Background studies for DarkSide Detectors

by
Sagar Sharma Poudel

A dissertation submitted to the Department of Physics ,

College of Natural Sciences and Mathematics

in partial fulfillment of the requirements for the degree of

Doctor of Philosophy
in Physics

Chair of Committee: Prof. Andrew Renshaw

Committee Member: Prof. Ed Hungerford

Committee Member: Prof. Lisa Whitehead Koerner

Committee Member: Prof. Carlos R. Ordonez

Committee Member: Prof. Omprakash Gnawali

University of Houston
December 2020

DEDICATION/EPIGRAPH

In loving memory of my mother Satyadevi Bastola

ACKNOWLEDGMENTS

I express my deep gratitude to Prof. Andrew Renshaw for his constant guidance and immense support through these past four years. I have learned a lot from him. He has also been a great source of inspiration and motivation for me. I am grateful to him for providing me opportunities to get involved in a variety of projects. I find it immensely satisfying when I think of the variety of knowledge, experience, and skills I acquired under his supervision.

I express my deep gratitude to Prof. Ed Hungerford for being such an influence during my research work. I have learned quite a lot of physics from the conversations we have had. I thank him for going over this dissertation and making a lot of corrections. His feedback has been invaluable.

I thank my Ph.D. committee members Prof. Lisa Whitehead Koerner, Prof. Carlos R. Ordonez, and Prof. Omprakash Gnawali for their valuable suggestions and feedback. I thank Dr. Paolo Agnes, who has given me constant physics inputs and guidance over the years. I got the chance to learn a lot from him about Monte Carlo simulations. I thank Dr. Anton Empl and Dr. Parth Singh for providing me guidance in my FLUKA simulations work. I also thank Dr. Aji Daniel, Mr. Jonathan Miller who gave me keen insights on statistical data analysis during the early months of my research work. I thank Dr. Rafay Anwar and Mr. Frank Malatino, who I have had numerous physics and “coding” discussions in the past.

I am thankful to all the DarkSide collaborators who provided me physics inputs, suggestions, and feedback during the course of my research work. Last but not the least, I am thankful to my wife Shila Marasini for her love, inspiration, and motivation. I am also thankful to my little boy Watsal Poudel for giving me joy and happiness during these years. I thank my aunt Laxmi Bhandari for her love and support and her lasting influence in my life.

ABSTRACT

Direct dark-matter detection experiments search for the signals from dark matter (DM) scattering off an atomic nuclei target. The DarkSide-50 experiment used a dual-phase Time Projection Chamber (TPC) with liquid argon (LAr) as the DM target. The next-generation DM detector, DarkSide-20k, will have multiple tons of liquid argon in its TPC for dark matter searches. It is expected to achieve sufficient sensitivity to detect WIMP dark matter or exclude a large parameter space for the WIMP-hypothesis.

The expected dark-matter event rate, is at most, few per year per ton of target. To detect such rare interactions, DM searches should be nearly "background-free". The experiments need to adopt means and techniques to suppress, mitigate, and possibly reject all background to be able to detect dark matter. All potential sources of background have to be studied, and their rates estimated or measured.

In this thesis, I present the results from my study of two potential backgrounds for dark matter searches: 1) Background from $^{42}Ar/^{42}K$ radioactive decays, and 2) Background from cosmic-ray muon and neutron interactions.

^{42}Ar and ^{42}K decays are a potential source of background in liquid argon detectors. In this thesis, I report the results from my studies of background from $^{42}Ar/^{42}K$ decay using DarkSide-50 data. The specific radioactivity for $^{42}Ar/^{42}K$ in DarkSide-50 was found to be on the order of few tens of μBq per kg of natural argon. In addition, I report my studies of possible search channels and potential signatures from the decay of $^{42}Ar/^{42}K$ isotopes in liquid detectors.

Neutrons produced by cosmic-ray muon interactions are a major source of background in underground dark-matter detectors. In this work, I present the results of my FLUKA-simulations study of cosmogenic background for DarkSide-20k. Based on these studies, the DarkSide-20k experiment can reject cosmogenic neutron backgrounds with high efficiency.

TABLE OF CONTENTS

LIST OF FIGURES

LIST OF TABLES

Chapter 1

Dark Matter

A multitude of astrophysical observations from the past several decades provides evidence for the existence of non-luminous matter (dark matter). The observations show dark matter contributes roughly 80% of matter-content (and 27% of total mass-energy content) of the universe. The evidence for dark matter is mostly based on the observations of gravitational effects of dark matter (DM) in astrophysical scales. The astrophysical observations put constraints on the particle properties of dark matter. DM particles interact with standard matter only through gravitation and possibly through other weak-scale processes.

1.1 Evidences for Dark Matter

In the early 1930s, Fritz Zwicky [17] measured the velocity dispersion of galaxies in Coma cluster using observed Doppler shifts in the galactic spectra. Using the Virial theorem, he calculated the average mass of the galaxy in the cluster based on the observed velocities. He found that the average mass of the galaxy within the cluster was several hundred times the mass estimated from the luminosity-based measurements [17]. Zwicky proposed the discrepancy could be resolved if some form of non-luminous matter contributes to the bulk of the mass of the cluster. He called the non-luminous (but gravitating) matter "dunkle Materie" (dark matter).

1.1.1 Rotation Curve of Spiral Galaxies

One of the most convincing evidence for dark matter comes from the study of the rotation curve of the galaxies. The rotational curve of galaxies is a plot of velocity (of a star or gas cloud) as a function of distance from the galactic center. Vera Rubin in the 1970s obtained the rotational curves for spiral galaxies based on the observations of the Doppler shift of the 21 cm neutral hydrogen line [18]. The rotational curves can provide information about the mass distribution within the galaxy. Beyond the bulk of the (visible) mass of a galaxy, the rotational velocity of a star or a gaseous cloud at distance r can be obtained from;

$$V(r) = \sqrt{\frac{GM(r)}{r}} \tag{1.1}$$

where M(r) is the mass internal to the radius r from galactic center. From Equation 1.1, the rotational velocity should fall as $v(r) \propto \frac{1}{\sqrt{r}}$. Rubin found that beyond a few kpc from the galactic centre, the rotational velocities are roughly constant well past the main distribution of visible mass [19]. Outside the bulge of the galaxy, galaxies seem to exhibit a universal dark matter halo with a density profile of roughly $\rho \propto 1/r^2$. As seen from the fit components in Figure 1.1, the visible disk and the gas components are not enough to explain the flat "rotational curve" observed at larger radii.

The observations, as well as large-scale simulations of halo density profiles from the scale of galaxies to galaxy clusters, support "cold" dark matter (CDM) halo models [20][21]. The CDM halo density profile is approximated well by the Navarro-Frenk-White (NFW) density function [22][23] given by

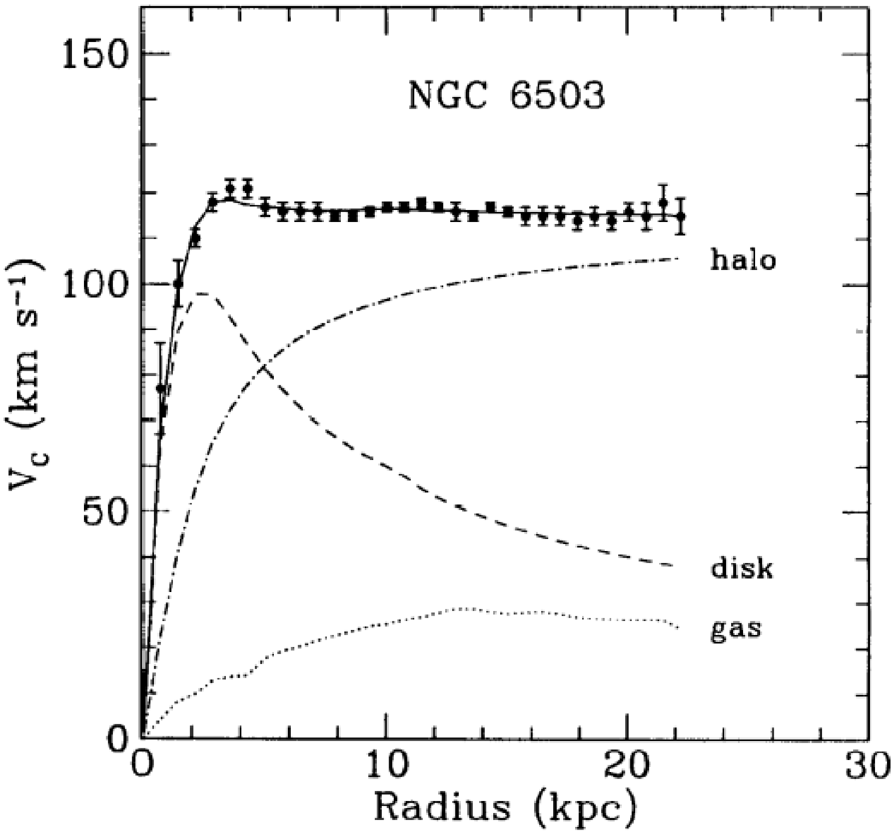

Figure 1.1: Rotational curve for galaxy NGC 6503 wich shows the mass contribution from dark matter halo, disk and gas are required to fit the data [1].

$$\rho(r) = \frac{\rho_0}{\frac{r}{r_h}\left(1+\frac{r}{r_h}\right)^2} \tag{1.2}$$

where r_h is a scale radius (that characterizes the size of dark matter halo) and ρ_0 is the dark matter density at radius r_h. The form of the density function in Equation 1.2 suggests a simplified isothermal density profile ($\rho \propto 1/r^2$)) approximately holds close to the scale radius, r_h. At large radii, $\rho(r)$ falls as $1/r^3$. The DM density profile within the bulge (especially within the galactic core) is still not fully understood [21][24][25]. But there is a sufficient evidence that DM dominates the matter content in galaxies (and galaxy clusters), and possibly dictates the formation and evolution of those structures.

1.1.2 Cosmic Microwave Background Measurements

The precision measurements of Cosmic Microwave Background (CMB) gives strong evidence for the existence of non-baryonic dark matter [2][26][27]. CMB is relic radiation that originated approximately 380,000 years after the Big Bang. Prior to the emission of CMB (or recombination), the universe was composed of dense plasma and photons (in thermal equilibrium). In this state, the universe behaved as a "baryon-photon" fluid. The universe was opaque to photons. As the universe continued to expand and cool, the temperature fell below atomic ionization energies (few eV). The ionized plasma could form neutral atoms (the process is called recombination). There was no free charge for photons to scatter off, so the photons decoupled and could stream freely. These photons are observed today as CMB [28]. The CMB had a temperature of $\sim 10^4$ K at the time of decoupling. However, as the universe has expanded and cooled, the mean CMB temperature is now about 2.7 K [26].

The full sky CMBR temperature map (as shown in the Figure 1.2) shows a high degree of isotropy suggesting the universe is largely isotropic and homogeneous. However, the measurements of CMB in smaller angular scale by COBE [26], WMAP [27], and PLANCK [2] reveals anisotropies. The analysis of CMB anisotropies enables the testing of cosmological models and puts stringent limits on cosmological parameters.

The anisotropy of CMB can be quantified by decomposing the temperature field $\mathrm{T}(\theta, \phi)$ into a series of spherical harmonic functions, $Y_{lm}(\theta, \phi)$;

$$T(\theta, \phi) = \sum_{l=0}^{\infty} \sum_{m=-l}^{l} a_{lm} Y_{lm}(\theta, \phi) \tag{1.3}$$

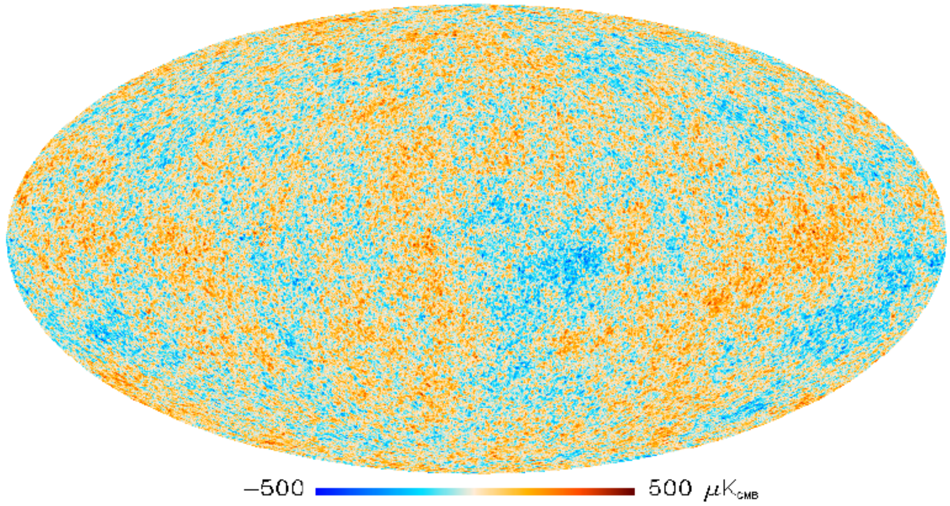

Figure 1.2: Full sky Cosmic Microwave Background temperature map from the Planck project [2].

The amplitude of each spherical harmonic is given by

$$a_{lm} = \int_{4\pi} T(\theta, \phi) Y^*_{lm}(\theta, \phi) \mathrm{d}\Omega \tag{1.4}$$

m takes 2l+1 values between $-l$ and l allowing $2l$ +1 modes to multi-pole l. The amplitude C_l is defined as an average over m for every l,

$$C_l = \frac{1}{2l+1} \sum_{m=-l}^{l} |a_{lm}|^2 \tag{1.5}$$

Once C_l is calculated the CMB angular power spectrum is usually plotted with $D_l = C_l l(l + 1)/2\pi$ (which characterises the anisotropy at the scale of $S_l = \frac{180^\circ}{l}$) against the l multi-poles.

After the inflationary period, the high-density regions formed a gravitational potential and began to grow. At the same time, there was also an outward force due to photon pressure. These opposing forces which are tightly coupled in the photon-baryon fluid, result in acoustic oscillations. The imprint of these oscillatory features of the baryon-photon fluid

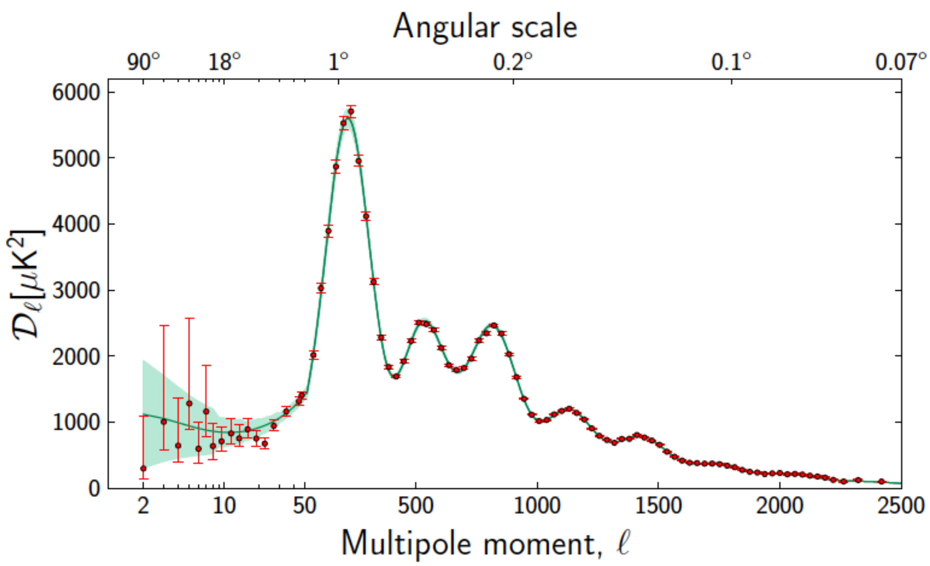

Figure 1.3: CMBR temperature anisotropy angular power spectrum decomposed into spherical harmonics. And the fit of six parameter ΛCDM Model.The shaded area represents the cosmic variance. The horizontal axis is logarithmic for $l <= 50$ and linear beyond it [2].

(from the time of the last scattering) is observed in the CMB anisotropy power spectrum.

The CMB spectrum for l <= 50 is the imprint of initial quantum fluctuations enlarged by inflation, and is related to the early universe and not with the recombination era. At larger l values, the imprints are from the acoustic oscillations. The first acoustic peak gives the size of the horizon at recombination. The distance from the last scattering surface can be determined from the expansion rate of the universe. As the angular size of the horizon gives the geometry of the universe, the location of the first peak at l $\sim$ 200 suggests the geometry of the universe is almost flat [29]. The odd-numbered-peaks represent compressions of the plasma while the even-numbered-peaks represent rarefaction. The greater the mass of baryonic matter in the early universe, the greater the compression in these acoustic oscillations, and the larger the first peak and subsequent odd-numbered peaks [30]. But the amplitude of the second peak and subsequent even-numbered peaks depends on how much the plasma will expand in acoustic oscillations and are insensitive to the total baryonic content of the universe. With increased baryonic mass, the amplitude of the first peak increases but not that of the second peak [30]. Enhanced third peak and almost comparable to the second peak suggests a high density of dark matter. Based on the Planck's measurements [2], the total matter density of the universe is $\Omega {h_0}^2 \sim 0.118$. And the baryonic matter density is $\Omega_b {h_0}^2 \sim 0.022$. This result is consistent with the value baryon matter predicted by Big Bang nucleosynthesis (BBN) [3][31]. The $\bigwedge$CDM cosmological model [32][33][34][35] is parameterization of the Big Bang model that incorporates cosmological constant as well as the cold dark matter. The 6-parameter $\bigwedge$CDM cosmological model fits the CMBR power spectrum very well. So, Planck's results suggest: The mass-energy content of the universe comprises of 68%, 27% and 5% of dark energy, dark matter, and baryonic-matter, respectively. This means a large fraction of the matter content of the universe is non-baryonic.

1.1.3 Constraints from Big Bang Nucleosynthesis (BBN)

The measurements of abundances of light nuclei can be used to provide an independent estimate of total baryon density in the universe.

After the Big Bang, when the universe cooled to a temperature of a few MeV, the universe was composed primarily of stable baryons (protons, neutrons), leptons and anti-leptons, and photons [36]. The charged-current weak interactions of the kind: $n + e^+ \Longleftrightarrow p + \bar{\nu_e}$, $n + \nu_e \Longleftrightarrow p + e^-$, $n \Longleftrightarrow p + e^- + \bar{\nu_e}$ were in equilibrium, and the neutron and proton had roughly the same abundance. But as the temperature fell, the (n/p) ratio is suppressed by the Boltzmann factor $exp(-\Delta m/T)$ ($\Delta m = 1.293$ MeV) [37] . As the universe expanded and temperature decreased to around a few MeV, the n/p ratio was no longer able to remain in equilibrium. Neutrons are not stable, as they would decay if not bound into stable nuclei. The binding is not significant until the temperature is well-below the binding energy of deuterium (^2H), 2.2 MeV. As the temperature decreased, stable ^2H could be formed. But at high enough nucleon density, most of ^2H would convert to ^4H. As the temperature decreased to around 0.1 MeV, most of ^2H, trace amounts of ^3He and ^4He, ^7Li were also formed. Around 100 sec after the Big Bang, Big Bang Nucleosyhthesis (BBN) ended. As the universe expanded, and the temperature fell below keV, nucleo-synthesis was no longer feasible. All the neutrons not bound to nuclei decayed. At the end of the BBN, the baryonic content of the universe consisted of free protons, ^4He, and less than 1% of other nuclei. The BBN-predictions of elemental abundances can be tested by measuring the elemental abundances in the regions of the sky that have a small fraction of heavy elements, which indicates low levels of chemical enrichment. In those regions, the observed abundances of lighter nuclei would be close to the values after the end of BBN. The relative abundances of the lighter elements predicted by BBN are in excellent agreement with measured abundances [3][38] (as shown in Figure 1.5).

During the BBN era, any increase in the baryon density would lead to more deuterium (^2H) ending up in ^4He. This would decrease the relic abundance of ^2H as measured today. The baryon abundance can be parameterized by $\eta = N_b/N_\gamma$. The baryon number density N_b and photon number density N_γ both decrease proportional to a^{-3} (a is the scale factor characterizing relative expansion of the universe) with the expansion of the universe. Therefore, the ratio η is unchanged at least in the scale of age of the universe. The Deuterium-to-Hydrogen measurements give η on the order of 5×10^{-5}. Based on the value of η, baryon fraction to a critical density $\Omega_b {h_0}^2 \sim 0.02$, where $h_0 = 0.7$ is the Hubble constant in unit of 100 km$\cdot$s^{-1}/Mpc [3][31].

The mass-energy density of the universe is close to critical density [2][29][39]. In units of critical density, $\Omega_b \sim 0.04$. i.e baryonic matter contributes only $\sim 4\%$ to mass-energy density of the universe. A significant fraction of the matter-energy content of the universe must be non-baryonic.

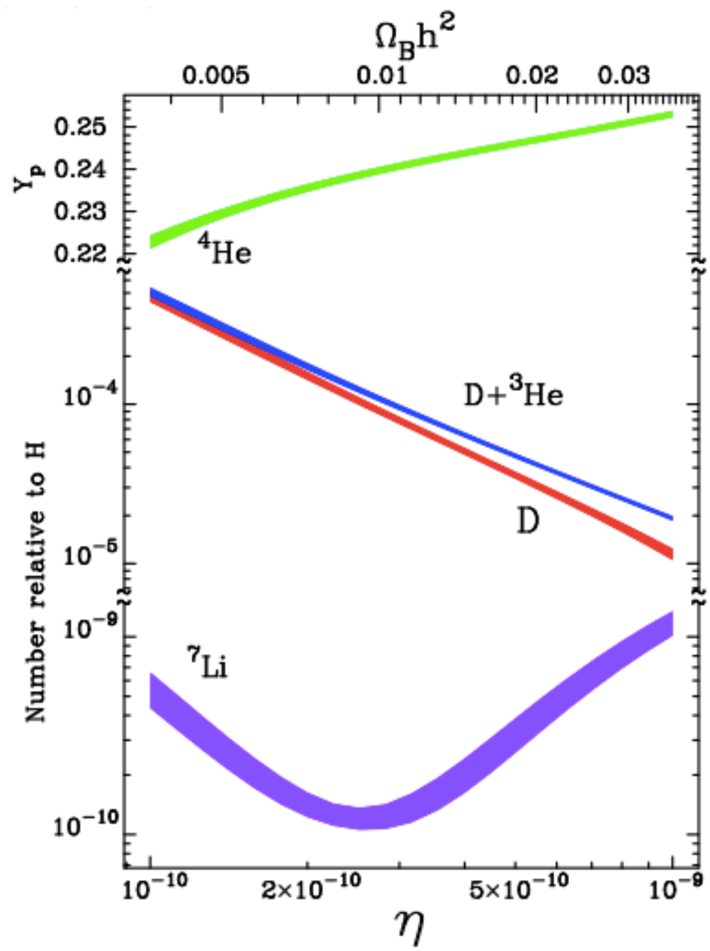

Figure 1.4: Prediction of abundances of the lighter elements from Big Bang Nucleosynthesis. Bands, shown at 95% confidence level. Y_p represents the abundance relative to hydrogen (^1H). Figure taken from [3].

1.1.4 Gravitational Lensing Measurements

From the General Theory of Relativity (GTR), a strong gravitational field can distort the space-time metric and bend the light passing through it [40]. So, the gravitational potential well of stars, galaxies, and galactic clusters can act as a “gravitational lens”. The Gravitational lensing effects provide a unique probe to search for dark matter. From the observational viewpoint, a simple theoretical treatment of gravitational lensing is given in [41]. The global magnification$|\mu|$ due to gravitational lensing can be characterized by parameters κ and γ ;

$$|\mu| = \frac{1}{(1-\kappa)^2 - |\gamma|^2} \tag{1.6}$$

Here, $1-\kappa$ characterizes isotropic magnification of the lensed source and γ characterizes the distortion of images caused by gravitational shear. A strong gravitational lensing regime has gravitational lenses with $\kappa \geq 0.5$ and $\gamma \geq 0.5$. Deep potential wells like galaxies and galaxy clusters can generate “strong lensing”. Strong lensing may result in the formation of multiple images, rings, and arcs of background gravitational structure [42] [43] [44]. The information about deflection, magnification, gravitational shear from these lens-sources can be used to reconstruct the mass of the lensing object. Strong gravitational lensing from galaxy or galaxy cluster can produce Einstein Ring and Giant arcs. Einstein Ring is formed if the distant source of light is directly behind the strong gravitational lens. Gravitational lensing information can be used to estimate mass-to-luminosity ratios of the galaxy clusters. The mass-to-luminosity ratio for the Abell 370 cluster was found to be ~ 370 [45]. This shows large fraction of the matter content in the galaxy is non-luminous. The gravitational lensing measurements [46][47] suggest the mass-to-luminosity ratio of galaxies increases with mass as well as with radius. This indicates the mass distribution of galaxies is different from

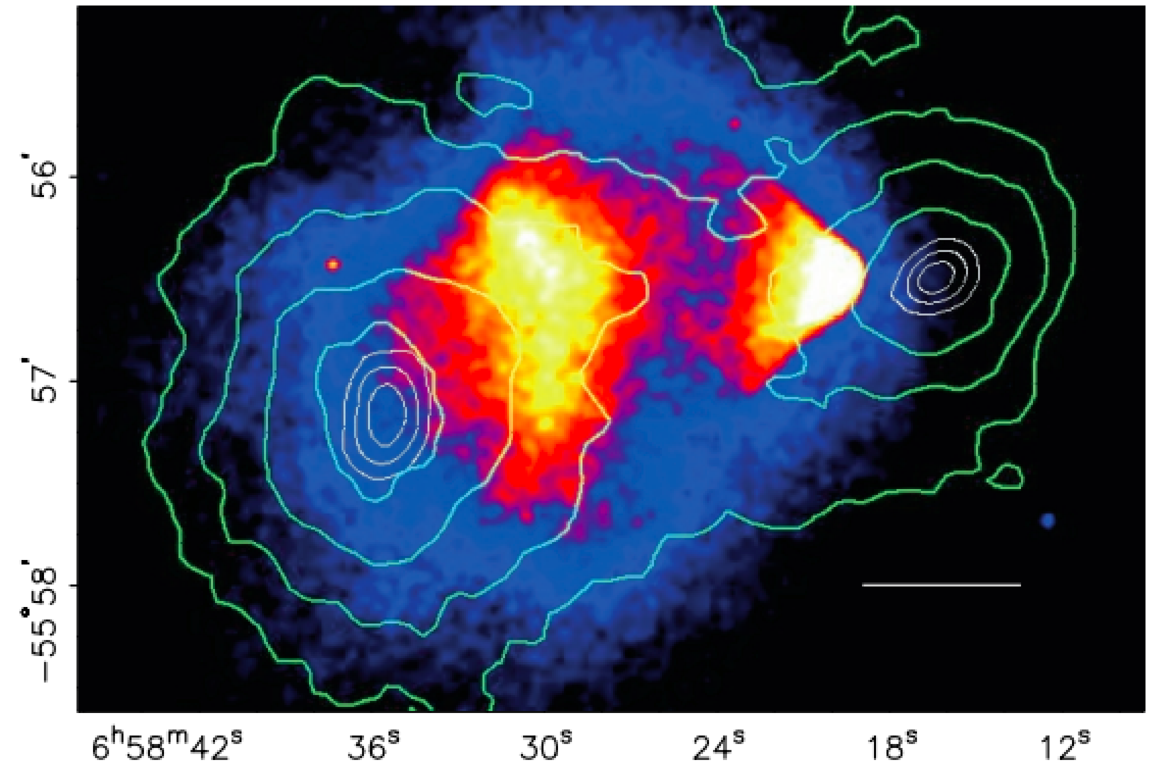

Figure 1.5: The lensing mass and Chandra X-ray emission map of 1E0657-56 (bullet cluster) showing two massive substructures that are offset with respect to the baryonic distribution. The color represents the temperature of the plasma (highest temperature regions (in white) and lowest temperature regions (in blue). The contours overlaid on the image show the gravitational potential, reconstructed using strong and weak lensing data. Figure taken from [4].

the mass distribution of luminous matter.

In a weak lensing regime, the distortions of shape of background objects by the foreground gravitational potential is small [48]. The presence of foreground sources can still be inferred from the statistical analysis of distortions on the shapes of background objects. Objects like neutron stars, black holes, planets, and brown dwarfs are commonly called massive astrophysical compact halo objects (MACHOs). The typical mass range for MACHOs is from $10^{-8}M_{\odot}$ to $10^{2}M_{\odot}$ [49]. These objects can act as a micro-gravitational lens, and increase the apparent brightness of the foreground star. The apparent brightness of a star can vary as a MACHO passes through the line of sight. This can be used to detect the presence of a MACHO. A Microlensing survey of millions of MACHOs in the Milkyway galactic halo and Large Magellanic Cloud (LMC) suggests the MACHOs account for a negligible fraction of non-luminous matter [49][50][51]. The combined result of EROS and MACHOS collaboration suggests MACHOs in mass range $10^{-7}M_{\odot}$ to $10^{-3}M_{\odot}$ contribute less than 25% to halo dark matter for most models. While MACHOs in the mass range $3.5 \times 10^{-7}M_{\odot}$ to $4.5 \times 10^{-5}M_{\odot}$ can at best contribute to 10% of a mass of spherical dark matter halo [49].

Gravitational lensing measurements of the mass distribution of merging galaxy clusters 1ES 0657–558 (Bullet cluster) [4][52] and MACS J0025.4-1222 [53] provides very strong evidence of dark matter. In both clusters, the combined weak and strong lensing mass reconstructions show the mass distribution of the clusters doesn't coincide with the baryon distribution (observed in X-rays by Chandra). The measure of off-set of total mass from the centre of baryonic mass may not be explained by the alteration of gravitational force law as suggested in MOND theories [54][55]. In the merging scenario, the decoupling of dark matter and hot baryonic plasma components also gives a strong argument for collisionless (weakly self-interacting) dark matter.

1.2 Brief overview of Some Dark Matter Candidates

The astrophysical observations put constraints on the expected properties of dark matter. So far, the observations suggest the following: Dark matter should be 1) stable (on a cosmological time scales), 2) charge neutral, and 3) weakly interacting. None of the Standard Model (SM) particles have all these properties. But some particle candidates have been proposed in the context of other theories. Some popular particle dark matter candidates are briefly discussed below.

1.2.1 Axion

The axion [56][57][58] is a pseudoscalar particle initially proposed by Peccei and Quinn to solve the "strong" CP problem. The Lagrangian of QCD can be expressed as;

$$L = L_{pert} + \frac{\theta g^2}{32\pi^2} G^a_{\mu\nu} G^{\tilde{a}\mu\nu} \tag{1.7}$$

where $G^a_{\mu\nu}$ represents QCD field strengths, g is the QCD coupling constant, and θ is a parameter. The second term arises due to non-perturbative effects. QCD depends on θ through $\bar{\theta} = \theta - arg(m_1, m_2, ...m_n)$ [59][60]. If quarks were massless, θ dependence vanishes, and CP violation would not occur [61]. However, $\bar{\theta}$ has been experimentally measured and the strong constraint comes from the measurement of neutron electric dipole moment ($\bar{\theta} < 10^{-9}$) [62]. This suggests that CP violations in strong interactions is non-vanishing, but immensely suppressed. This is called the strong CP problem.

Peccei and Quinn originally proposed to solve the strong CP problem by postulating the existence of a global quasi-symmetry $U_{PQ}(1)$ [56]. They suggested this symmetry is spontaneously broken by those non-perturbative effects that makes the physics of QCD depend on θ. The axion is a quasi-Nambu-Goldstone boson associated with the breakdown of the symmetry $U_{PQ}(1)$. In that case, one has

$$\bar{\theta} = \theta - arg(m_1, m_2, ...m_n) - \frac{a(x)}{f_a} \tag{1.8}$$

where, $a(x)$ is axion field and $f_a = \nu_a/N$ is an axion decay constant (with ν_a as vacuum expectation value, which spontaneously breaks $U_{PQ}(1)$, with N as $U_{PQ}(1)$ anomaly parameter) [63]. The additional term allows $\bar{\theta}$ to relax to zero dynamically, and solves the strong CP problem.

Axions potentially can solve the "strong CP problem" of SM , and they are also a viable dark matter candidate. They are non-relativistic, weakly interacting, and light [64]. The axion mass is given in terms of f_a by [61]:

$$m \simeq 0.6eV \frac{10^7 GeV}{f_a} \tag{1.9}$$

The axion couplings are inversely proportional to f_a. So, the mass of the axion is proportional to the strength of couplings. The astrophysical observations and laboratory searches put strong limits on the mass and couplings of axions [64][65]. For dark matter searches, of particular interest, is the axion-coupling to two photons ($\gamma^* + \gamma \rightarrow a$ or $a \rightarrow \gamma^* + \gamma$) [61][66]. The Axion Dark Matter eXperiment (ADMX) [67] searches for signals from axion-to-photon conversion (in the presence of a strong magnetic field). It has put limits on the strength of axion-photon couplings for μeV dark matter axions [68].

1.2.2 Sterile Neutrino

There are three known flavours of neutrinos ν_e, ν_μ and ν_τ. The neutrino flavour oscillations have been observed, which suggests neutrinos have some mass [69][70]. Also, Neutrinos weakly couple with leptons and quarks. Based on their properties, neutrinos may seem like a promising dark matter candidate. But Standard Model (SM) neutrinos have a very tiny mass. Based on Planck measurements [71], the sum mass of neutrinos should be smaller than eV. Such light neutrinos would decouple from the dense plasma in the early universe at temperatures of few MeV [72][73] (i.e when they are still relativistic). This makes SM Neutrino the "hot dark matter" (HDM) candidate. The dark matter that is "cold" at the time of decoupling explains better the structure formation and sub-degree feature of CMBR spectrum. A "Sterile" neutrino is a fourth flavored "massive" neutrino that has ultra-weak couplings with Standard Model (SM) neutrinos. In generic "Seesaw Models" [74][75], the existence of heavier "sterile" neutrinos are postulated to explain neutron-flavor mixing (and lightness of SM neutrinos). These weakly interacting massive neutrinos are good, cold dark-matter candidates. There are various mechanisms by which sterile neutrinos could have been created in the early universe. An overview of the current status of the research on sterile neutrino is reported in [76][77]. One mode of astrophysical search is: the radiative decay of a sterile neutrino into monoenergetic flux of X-rays with energy $E_\gamma \sim m_s/2$, where m_s represents the mass of sterile neutrino [78].

1.2.3 Weakly Interacting Massive Particles(WIMPs)

Weakly Interacting Massive Particles are a class of non-baryonic cold dark matter particles that interact weakly and have mass on the order of GeV to TeV [79]. WIMPs are promising dark matter candidates. In generic WIMP models, WIMPs are in thermal equilibrium with quarks and leptons in the early universe and have the right abundance to be a cold dark matter [80]. Moreover, weak-scale interactions of WIMPs give the right WIMP relic density and make the detection of WIMPs possible in today's or near future direct, indirect, and collider-based searches [76][81].

WIMP-like particles are also predicted by supersymmetric theories [80]. Supersymmetric theories incorporate symmetry between bosons and fermions. For each bosonic particle in SM, it has a fermionic counterpart and vice versa differing by spin $\frac{1}{2}$. The superpartner of fermions has prefix 's' (e.g. selectron, squark) while the superpartner of bosons has suffix 'ino' (e.g. gravitino, Higgsino). The electrically neutral part of the Standard Model Higgs field is a complex scalar H with a classical potential [82]

$$V = {m_H}^2 |\ H\ |^2 + \lambda |\ H\ |^4 \tag{1.10}$$

The Standard Model requires a non-vanishing vacuum expectation value (VEV) for H at the minimum of the potential. This occurs if $\lambda > 0$ and ${m_H}^2 < 0$. The SM Higgs is light, with mass $\sim$ 125 GeV [83]. In the framework of SM, enormous quantum corrections are required to the Higg's field to produce such a light Higgs. This is called the "hierarchy problem", and this problem could be solved if SM is supplemented by some scalar particles at electroweak scale [84]. Supersymmetric theories predict such particles [82]. In a minimal supersymmetric extension of the Standard Model (MSSM), baryon number (B) and lepton number (L) are violated. This is reconciled by imposing a discrete symmetry R-parity, $R = (-1)^{3B+L+2S}$, S for a particle of spin S [82]. SM particles have even parity ($R = 1$), and their supersymmetric partners have odd parity ($R = -1$). When R-parity conservation is imposed, the lightest supersymmetric particle (LSP) with $R = -1$ is stable, and potentially a dark matter candidate. In many theories, the lightest superpartner (LSP) is neutralino (a linear combination of the mass eigenstates of supersymmetric partners of a photon, Z^0 boson, and neutral-Higgs bosons, namely photino, zino, higgsino, respectively).

In a standard case, in the early universe, WIMPs are in thermal and chemical equilibrium with all other particles of the thermal plasma [76]. At temperatures much higher than the WIMP mass, the WIMP production and annihilation from and to SM particles were in equilibrium. And their common rate is given by;

$$\Gamma_{ann} =< \sigma_{ann} v > n_{eq} \tag{1.11}$$

where σ_{ann} is the WIMP annihilation cross-section, where v is relative velocity of annihilating WIMPs, and n_{eq} is the WIMP number density in chemical equillibrium and $< \sigma_{ann} v >$ is the average over the WIMP thermal production. As the universe expands, the number of produced WIMPs falls exponentially by a Boltzmann factor $e^{-m_\chi/T}$, where m_χ is mass of the WIMP particle. Then the number density, n, and WIMPs annihilation rate falls, and the WIMPs freeze out of equilibrium. With WIMP freeze-out temperatures ($m_\chi/T \sim 20$), $m \geq 100MeV$, WIMPs would freeze out before Big Bang Nucleosynthesis (BBN) and could act as seeds for the cosmological structures (galaxy and galaxy clusters) we observe today. Assuming entropy of matter and radiation has been conserved since WIMP freeze-out, one could obtain the present relic abundance for WIMP as a function of the self-annihilation cross-section [81] as;

$$\Omega h^2 \approx \frac{3 \times 10^{-27} cm^3 s^{-1}}{< \sigma_{ann} v >} \tag{1.12}$$

With $\Omega h^2 \sim 0.1$ for dark matter, and a value of $v \sim 0.1\ c$, σ_{ann} is typical for weak interactions in SM. A DM particle with a cross-section of electroweak scale, can produce the correct magnitude of the observed dark matter abundance. So, this makes WIMP the most favored DM candidate. And most of the experimental efforts, so far, have been focused on detecting WIMP-like particles [76].

1.3 Detection of Particle Dark Matter

Despite the compelling evidence of dark matter (DM) at various astrophysical scales, the "particle" nature of DM remains unknown. However, the astrophysical observations constrain the expected properties of dark matter, and the WIMP remains the leading candidate. In general, there are three approaches to detect DM: 1) indirect, 2) direct, and 3) collider searches.

The "indirect detection" approach involves searching for indirect signatures of DM interactions, possibly through the detection of secondary particles produced by decay or annihilation of DM particles [85][86][87]. If WIMPs could annihilate in the early universe, one could look for the signatures of WIMP annihilation reactions similar to $\chi\bar{\chi} \rightarrow e^+e^-$, $\mu^+\mu^-$,

$q\bar{q}$, W^+W^-. Detecting gamma-rays produced from the annihilation or decay of DM particles in regions like the galactic core appears most promising. Gamma-rays essentially travel in straight lines and may reach the detecting instruments unabsorbed in the local universe. These gamma rays may be detected as excess over known cosmic gamma backgrounds [87].

"Collider detection" involves colliding SM particles in accelerators to produce DM, and detecting the DM decay products or the "missing" energy carried away by the DM particles [88]. Collider experiments as LHC also look for signatures of new physics and may detect particles beyond SM. Collider-based searches provide an alternative channel to detect DM, complementing the direct and indirect searches.

The "direct detection" involves looking for signals from particle interactions of DM with SM particles. The direct detection experiments try to detect the signal from DM scattering off some target nuclei. The energy of the recoiling nuclei could be detected via scintillation, ionization, or phonons. Consider that a Dark Matter Halo in the Milky Way galaxy is composed of WIMPs. Then with local dark matter density $\rho_0 \sim 0.3\ GeV/cm^3$, mean WIMP velocity relative to target $< v > \sim 220\ km/s$ and WIMP mass m_χ as 100 GeV, the WIMP flux ϕ_0 received on the earth can be estimated.

$$\phi_0 = n_0 \times < v > = \frac{\rho_0}{m_\chi} \times < v > \sim 7 \times 10^4\ cm^2 s^{-1} \tag{1.13}$$

where, $\rho = \frac{\rho_0}{m_\chi}$ is number density of WIMPs. The WIMP flux is large. So, even though WIMPs are weakly interacting, they could be detectable in ultra-low background detectors [89]. WIMPs can also induce low energy nuclear recoils. The recoil energies could be keVs to hundreds of keVs. Typically, direct detection experiments aim to measure recoil energies E_R , and the event rate, R, within the limits set by the detector efficiency and backgrounds.

1.3.1 WIMP spectra and event rates

The differential event rate (usually expressed in counts per kg per day per keV) for nuclear recoils from WIMP interactions is given by;

$$\frac{dR}{dE_R} = \frac{\rho_0}{m_N m_\chi} \int_{v_{min}}^{\infty} v f(v) \frac{d\sigma}{dE_R}(v, E_R) dv \tag{1.14}$$

where m_χ is mass of WIMP, m_N is mass of the nucleus , ρ_0 is the local WIMP density, $\frac{d\sigma}{dE_R}(v, E_R)$ is the differential cross-section for WIMP-nucleus elastic scattering , $f(v)$ is the normalised WIMP velocity distribution in the detector frame, $\rho_0 \sim 0.3\ GeV/cm^3$ is the local dark matter density. The recoil energy, E_R can be expressed in terms of scattering angle (θ) in the centre of mass frame in the extreme non-relativistic limit as;

$$E_R = \frac{\mu^2 v^2 (1 - cos\theta)}{m_N} \tag{1.15}$$

where $\mu = m_\chi m_N/(m_\chi + m_N)$ is the WIMP-nucleus reduced mass. In the above v_{min} is the minimum WIMP speed that can induce nuclear recoils, and $v_{min} = \sqrt{(m_N E_R)/(2\mu^2 v^2}$. The upper limit for v is escape velocity v_{esc}, above this velocity WIMPs are not bound to Milky Way galaxy.

The total event rate (counts per kg per day) is obtained by integrating the differential event rate over all the possible recoil energies;

$$R = \int_{E_T}^{\infty} \frac{\rho_0}{m_N m_\chi} dE_R \int_{v_{min}}^{v_{esc}} v f(v) \frac{d\sigma}{dE_R}(v, E_R) dv \tag{1.16}$$

where E_T is threshold energy (smallest recoil energy measurable by the detector). In general,

$d\sigma/dE_R$ can be separated into spin-independent and spin dependent parts,

$$\frac{d\sigma}{dE_R} = (\frac{d\sigma}{dE_R})_{SI} + (\frac{d\sigma}{dE_R})_{SD} \tag{1.17}$$

The spin-independent differential cross-section $(\frac{d\sigma}{dE_R})_{SI} \propto A^2$, where A is mass number for the nucleus spin-independent differential cross-section. $(\frac{d\sigma}{dE_R})_{SI} \propto J(J+1)$, where J is the nuclear angular momentum [90]. In general, both the spin-independent and spin-dependent part contributes. The spin-independent (scalar) component dominates for heavy target nuclei ($A > 20$), which makes the case for using heavy nuclei such as silicon, germanium, argon, xenon as a target material in the direct detection experiments [9][12][13][91][92][93][94]. Some experiments [95][96][97] choose target nuclei with high nuclear angular momentum that are also sensitive to spin-dependent WIMP coupling.

For the standard halo model, the differential event rate in Equation (1.14) is described by a steeply falling exponential function [98];

$$\frac{dR}{dE_R} = \frac{R_0}{E_0 R} e^{-\frac{E_R}{E_0 r}} \tag{1.18}$$

where E_0 is the most probable WIMP kinetic energy, r is a kinematic factor $4m_\chi m_N/(m_\chi + m_N)^2$ and $R_0 = dR/dE_R)_0$ is event rate in the limit $E_0 \to 0$.

For fixed target nuclei, the expected WIMP-induced nuclear recoil spectrum is approximately an exponential spectrum with event rates falling off rapidly with increasing recoil energies. The more general form of Equation 1.18 also depends on the form factor $F(E_R)$ and accounts for further suppression of event rates at higher recoil energies. Since the interaction cross-section is small, the expected event rate is small. The direct dark matter detection experiments require ultra-low background to detect a WIMP. The ideal WIMP detector should have a large mass of target material, a low energy threshold, and the ability

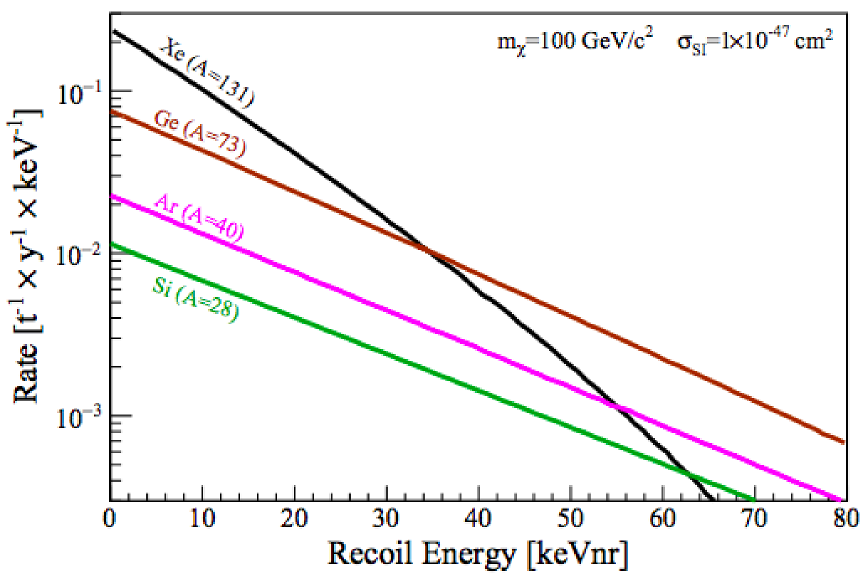

Figure 1.6: The expected nuclear recoil spectra induced by a $m_\chi = 100\ GeV/c^2$ WIMP in some common target nuclei with a spin-independent WIMP-nucleon cross-section $\sigma_{SI} = 10^{-47}\ cm^2$. As $d\sigma/dE_R \propto A^2$, greater event rates are expected for heavier target nuclei. For heavier nuclei, event rates fall off much more rapidly at high recoil energies due to form factor suppression. Figure taken from [5].

to efficiently discriminate the backgrounds.

1.3.2 Status of Direct Detection Searches

There are a large variety of experiments involved in direct dark matter detection efforts. PandaX [12], LUX [13], XENON1T [94], XMASS [99] are Xenon-based experiments. They can probe WIMP in both spin-independent and spin-dependent channels. DarkSide-50 [9], and DEAP-3600 [92] use liquid Argon as the target material to detect WIMP-nucleus spin-independent interactions. DarkSide employs a dual-phase (liquid-gas) argon Time Projection Chamber (TPC) to obtain signals from both the scintillation and ionization channel. There are other cryogenic experiments like EDELWEISS [100], (Super) CDMS [101] that use Ge-crystals to observe an ionisation and phonon signal. The CRESST [102] experiment uses $CaWO_4$-crystals and obtains scintillation and phonon readout. These crystal-based cryogenic experiments have energy thresholds on the order of keV and are sensitive to very light WIMPs.

No experiment yet has observed a statistically significant excess of dark matter over the expected backgrounds. NaI crystal-based experiment DAMA/LIBRA's claimed the discovery of a dark matter-induced annual modulation signature. But this has been largely ruled out based on the results from other sensitive experiments [94][103]. The Figure in 1.7 shows the exclusion curves obtained by various direct detection experiments and collider-experiment sensitive to spin-independent searches. The WIMP mass-cross section above the plotted curves is excluded by an experiment at 90% confidence level. In such exclusion curves, the WIMP-nucleon cross-sections are plotted in the vertical axis instead of WIMP-nucleus cross-sections, which facilitates comparison between experiments that use different target nuclei. Exclusion curves in general, rise steeply for low mass WIMPs. In low-mass WIMP regime, the experiments are typically limited by detector threshold, loss of signal acceptance, and

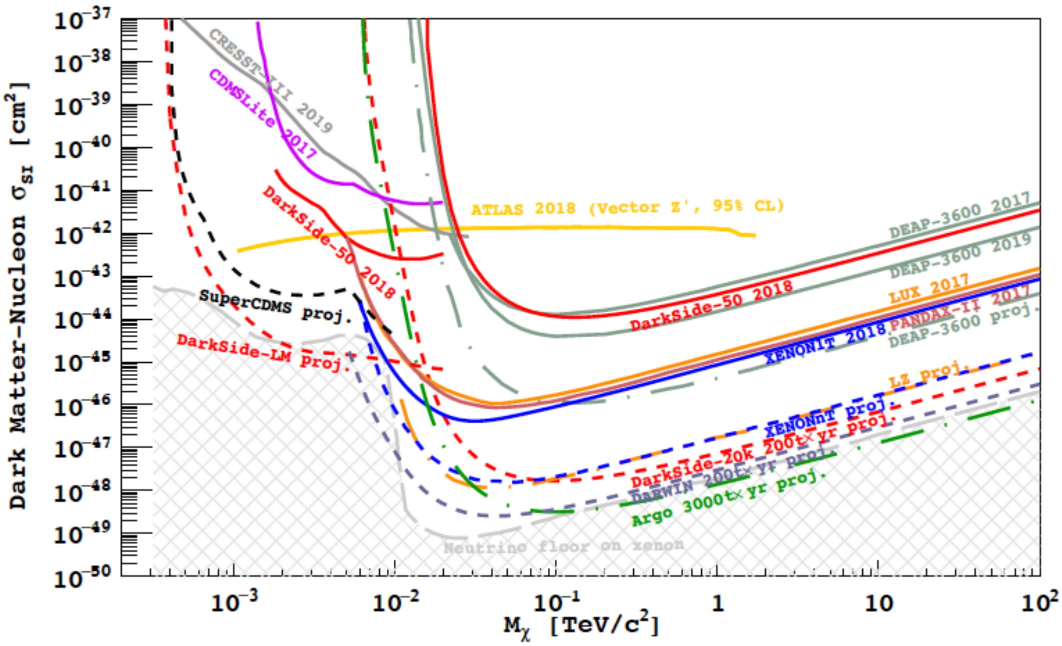

Figure 1.7: 90 % C.L. exclusion limits (represented by the continuous curves)showing leading results from direct and accelerator-based dark matter searches. For massive WIMPs, the current leading result is from XENON1T. Dotted lines represent the expected sensitivities for future germanium, xenon and argon-based searches. Figure taken from updated [6].

reduced light/charge yields. Exclusion curves also rise at higher WIMP masses since, for a fixed dark matter density, the expected WIMP flux is smaller, resulting in a lower event rate.

The present strongest limits for high mass WIMPs ($> 6\ GeV/c^2$) from WIMP-nucleus spin independent elastic scattering comes from XENON1T [11]. Using an ionisation-based signal alone, DarkSide-50 experiment placed the most strongest limits in the WIMP mass range ($1.8\ GeV/c^2 - 6\ GeV/c^2$) [104]. For very low mass WIMP, crystal based cryogenic experiments are expected to fare better due to their low energy threshold. CREST-III's limits are the strongest currently for $<\ 1.8\ GeV/c^2$ WIMPs. Xenon has naturally occuring non-zero spin isotopes ^{129}Xe and ^{131}Xe. So, the Xenon-based experiments XENON1T, PandaX, LUX also probe spin-dependent WIMP-nucleus elastic scattering and give strong limits

[95][96][105]. For typical direct detection searches, dominant backgrounds are electronic recoils, but the experiments have ways to reject such backgrounds with high efficiency. The backgrounds from nuclear recoil pose greater challenges. Next-generation detectors may also be sensitive enough to reach the "neutrino floor". The detectors may detect nuclear recoil signals from coherent neutrino-nucleus scatterings [106]. Since those signals will be identical to the signals from the WIMP, the neutrino-induced nuclear recoils are an irreducible backgrounds for the WIMP search. High energetic ^8B neutrinos from the sun would be an important background in search of low mass WIMPs ($m_\chi < \ 10\ GeV/c^2$). For high-mass WIMP ($m_\chi > \ 10\ GeV/c^2$) searches, the coherent scatterings from atmospheric neutrinos will be the dominant background. Next-generation larger detectors are expected to achieve the sensitivity required to probe the remaining parameter space above the neutrino floor.

Chapter 2

The DarkSide Program

2.1 Introduction

The DarkSide program consists of a series of DM/WIMP direct detection experiments using a dual-phase liquid argon Time Projection Chamber (LArTPC) [6][9]. The DarkSide-50 detector was the first physics-motivated detector in the DarkSide program. The DarkSide-50 detector has been operating underground at LNGS, in Italy since 2012 [7]. Important physics results of the DarkSide-50 experiment are reported in [6][7][9][104][107]. The experimental groups ArDM, DarkSide-50, DEAP-3600, and MiniClean that were using LAr detector technology to search for dark matter, joined to form the Global Argon Dark Matter Collaboration (GADMC) with a goal to design future experiments exploiting the advantages of LAr as a detector target. GADMC will build and commission DarkSide-20k detector. It will have ~ 50 tonnes of LAr in TPC as an active target for DM searches. Many fundamental design parameters for the DarkSide-20k experiment will be based on the experience gained by the DarkSide Collaboration. The information obtained in constructing, commissioning, and operating the DarkSide-50 detector in background free mode [6] is invaluable. The ultimate goal of the GADMC is to design ARGO (detector with multiple hundred of tons of

LAr as a target material) to search WIMP dark matter in all WIMP search parameter space above the “neutrino floor”.

2.2 DarkSide-50 detector

The DarkSide-50 detector is located in Hall C of LNGS under Gran Sasso mountain, in Italy [7].

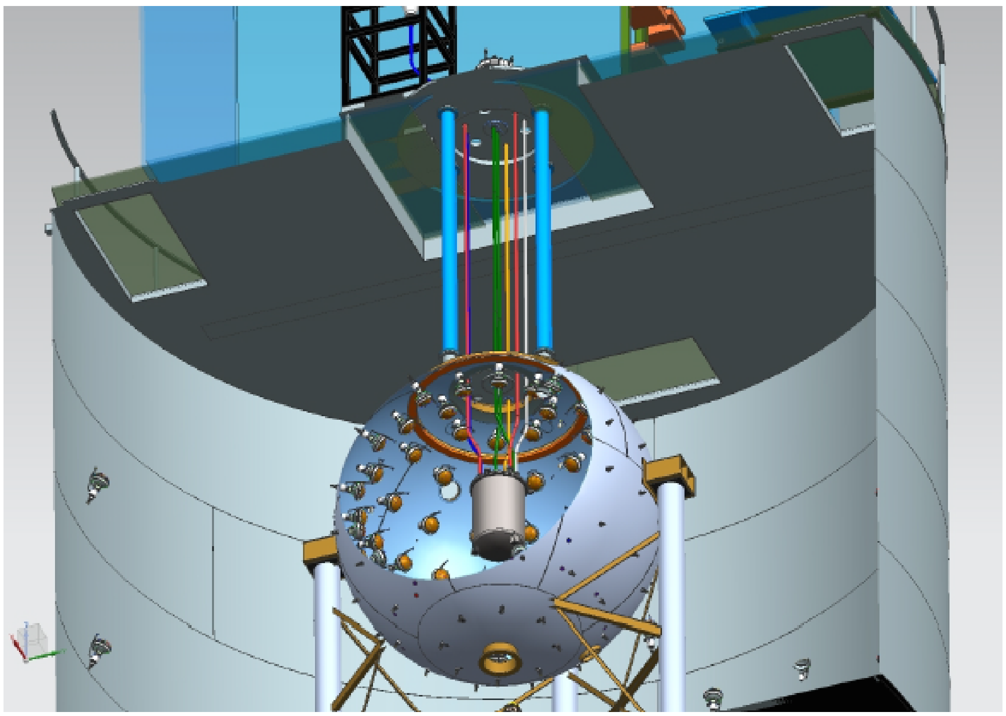

Figure 2.1: DarkSide-50 detector system. The outermost gray cylinder is the Water Cherenkov Detector (WCD). The sphere is Liquid Scintillator Veto (LSV) and contains boron-loaded liquid scintillator. The innermost gray cylinder is LAr Time Projection Chamber (TPC) cryostat [7].

It consists of three nested detectors as shown in Figure 2.1. From the center outward, the detectors are: Liquid argon Time Projection Chamber (LArTPC), Liquid Scintillator Veto (LSV), and Water Cherenkov Detector (WCD) [7]. The LAr TPC consists of active LAr volume which detects DM/WIMPs. The LSV acts as a shield and anti-coincidence veto for neutrons, gamma rays, and cosmogenic events (such as muons and its secondaries). The WCD serves as shielding and is used as anti-coincidence for cosmogenic events.

2.2.1 DarkSide-50 LAr TPC

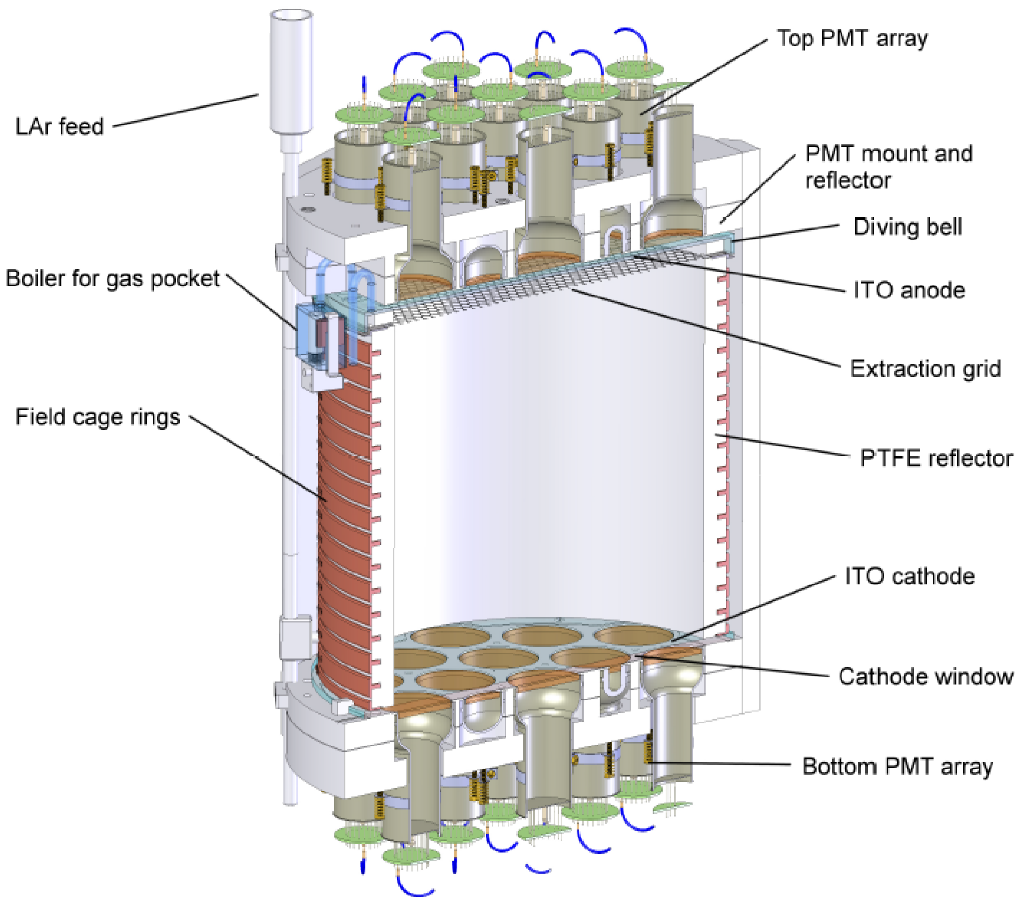

Figure 2.2: Cut-view of DarkSide-50 LAr TPC. Figure from [7].

The cut-view of DarkSide-50 TPC is shown in Figure 2.2. The active LAr volume is a cylindrical region of height 36 cm and diameter 36 cm holding (46.4 ± 0.7) kg of liquid argon [7]. A 1 cm argon gas layer is maintained at the top of the LAr volume. The cylindrical wall of the TPC is a 2.54 cm-thick PTFE (Teflon) reflector. The active volume is bounded at the top and the bottom by fused-silica windows.

Arrays of 38 Hamamatsu $R11065$ 3" PMTs (19 each on the top and bottom) which are submersed in LAr, view the active volume through the fused-silica windows. The inner surfaces of the fused-silica windows as well as the Teflon are coated with tetraphenyl butadiene (TPB). TPB is a wavelength-shifter. It absorbs the 128 nm UV scintillations from LAr and converts to visible photons for the PMTs to detect. The fused-silica windows are coated on both faces with thin transparent conductive indium tin oxide (ITO). This allows the inner window faces to act as a grounded anode at the top, while high voltage is applied to the bottom while outer surfaces are kept at the average PMT photocathode potential gradient.

The entire TPC structure is contained in a double-walled stainless steel cryostat which is held by the rods that hang from the top through WCD and LSV. The volume between the cryostat walls contains multi-layers of mylar insulation. The cryostat is cooled using an external circulation loop of purified liquid argon at 89 K. The vacuum plus the mylar insulation maintains the temperature at 89 K inside the cryostat while the outside of the cryostat is maintained at room temperature.

The electron drift system in DarkSide-50 TPC consists of the ITO cathode, anode planes, a field cage, and a grid. The grid is a hexagonal mesh etched from a 50 μm-thick stainless steel foil with high optical transparency ($\sim$ 95% at normal incidence). It remains 5 mm below the liquid-gas interface. The voltage between the cathode and the grid produces a vertical electric field that causes ionization electrons in the LAr to drift upward. The field cage consists of copper rings that surround the PTFE cylindrical wall and are held at graded potentials to keep the drift field uniform across the active volume.

Any particle interaction in the active volume results in electronic recoils or nuclear recoil events which produce the primary signal, S1, and ionization electrons. The ionization electrons that survive recombination drift in the electric field, and are extracted into the gas layer above the LAr where they produce a secondary signal S2 by electroluminescence.

Thus, the Dual-phase LArTPC technology enables the collection of both S1 and S2 signals for each event.

2.2.2 DarkSide-50 Liquid Scintillator Veto (LSV)

The DarkSide-50 LSV is a 4.0 m diameter stainless steel sphere filled with 30 tonnes of boron-loaded liquid scintillator. The boron-loaded liquid scintillator has three primary components: 1) pseudocumene (PC), 2) trimethyl borate (TMB), and 3) 2,5-diphenyloxazole (PPO) [108]. PC is a primary scintillator used in the LSV and makes up the bulk of the scintillator cocktail. TMB contains natural boron with 20% of ^{10}B which has a large thermal neutron capture cross-section. This makes the LSV an effective neutron veto. PPO is a wavelength-shifter. An array of 110 Hamamatsu R5912 LRI 8 " PMTs is mounted on the inner surface of the sphere to detect scintillation photons [7].

Neutrons entering the TPC leave a prompt thermalization signal and/or a delayed signal following neutron capture within LSV. The neutron capture reaction $^{10}B(n,\alpha)^{7}Li$ makes the boron-loaded scintillator an effective veto for neutron background[109]. ^{10}B neutron capture can proceed in one of following two ways:

1) $^{10}B + n \rightarrow \alpha\ (1775\ keV) + {}^{7}Li\ (1015\ keV)$ (BR: 6.4%)

2) $^{10}B + n \rightarrow \alpha\ (1471\ keV) + {}^{7}Li^{*}$ (BR: 93.6%), $^{7}Li^{*} \rightarrow {}^{7}Li\ (839\ keV) + \gamma\ (478\ keV)$

The γ from the decay of $^{7}Li^{*}$ to ^{7}Li is most likely to leave a detectable signal in the LSV. The α and ^{7}Li have short track lengths and deposit all the energy within the LSV. But the scintillation output of the α and ^{7}Li is highly suppressed due to ionization quenching, and is equivalent to a $50-60$ keV electron. The measured LSV photoelectron (PE) yield 0.54 ± 0.04, makes the quenched energy detectable [7].

2.2.3 DarkSide-50 Water Cherenkhov Detector (WCD)

DarkSide-50 WCD is a cylindrical tank of diameter 11 m and 10 m height containing high purity water. The WCD uses the water tank which originally was part of the Borexino Counting Test Facility (CTF) [110]. The inside surface of WCD is covered with Tyvek-polythene-Tyvek reflector [111]. WCD is equipped with 80 ETL 9351 8" PMTs on the side and the bottom to detect Cherenkov photons produced by muons and other relativistic particles while traversing the water.

The Water Cherenkov Detector (WCD) provides a powerful shield against the external background (gamma rays, neutrons from the surrounding cavern walls). It also acts as a veto for muon and muon-induced secondaries. The muons or their secondaries produce Cherenkov signals in WCD . Based on Borexino's measurements [112], the muon flux is $(3.41 \pm 0.01) \times 10^{-4} m^{-2} s^{-1}$ in the LNGS. Approximately 2000 muons still cross the WCD every day. The cosmogenic muons can produce high energy neutrons which can penetrate the shielding and leave energy in the TPC. The WCD acts as a veto to detect muons that produced the neutrons.

2.3 DarkSide-20k detector

DarkSide-20k is a liquid-argon based multiton detector which will be constructed by the Global Argon Matter Collaboration (GADMC) at LNGS [6]. The DarkSide-20k will operate for a minimum of 10 years while maintaining a background level in the WIMP search region of less than < 0.1 events for the total exposure. Many of the fundamental design parameters for the DarkSide-20k are based on the experience from the successful commissioning of the DarkSide-50 detector. Extensive work on the prototype and the actual DarkSide-20k detector is already underway. The DarkSide-20k detector is expected to be fully installed and begin data acquisition by 2023.

The detector system for DarkSide-20k consists of an octagonal-shaped (dual-phase) TPC of height 350 cm consisting of 49.7 tons of underground liquid argon as the sensitive volume. The TPC is contained within a vessel made from ultra-pure polymethylmethacrylate acrylic (PMMA), similar to the DEAP-3600 experiment [113] and eliminates the need for a dedicated cryostat, or UAr containment vessel. The body of the PMMA vessel will be made from fused 5 cm thick acrylic plates. The top and the bottom lid serves as the anode plate and cathode plate of the TPC, respectively.

The veto detector system consists of an Outer Argon Buffer (OAB) (40 cm thick), Gd-doped PMMA shell (10 cm thick) and a Inner Argon Buffer (IAB) (40 cm thick). The Gd-doped PMMA shell is sandwiched between OAB and IAB atmospheric layers. The entire detector system (veto system and TPC) is contained in a ProtoDune-like AAr cryostat [114] filled with liquified atmospheric argon. Rejecting the stainless steel cryostat system for ProtoDune-like cryostat has some advantages. The active LAr volume will be contained in radio-pure PMMA, and the residual background from the cryostat system is greatly reduced. The ProtoDUNE-like cryostat system has the added advantage of being scalable, making it the technology suitable for the next-generation GADMC detectors. The Gd-doped PMMA shell is an efficient moderator of neutrons. The resulting γ rays from the neutron capture on Gd (as well as on H in acrylic) provide the means to veto the neutrons. A copper cage (acting as a Faraday cage) provides the optical insulation from the rest of the AAr external to the OAB and, also provides an electric shield for reducing external noise from background detector signals. The inner surfaces of the TPC (facing the active volume) will be coated with tetraphenyl butadiene (TPB) and converts the 128 nm argon scintillation light to a wavelength detectable by SiPMs. SiPMs have higher effective quantum efficiency, higher reliability at LAr temperature, and a higher radiopurity than PMTs. The photo-sensing

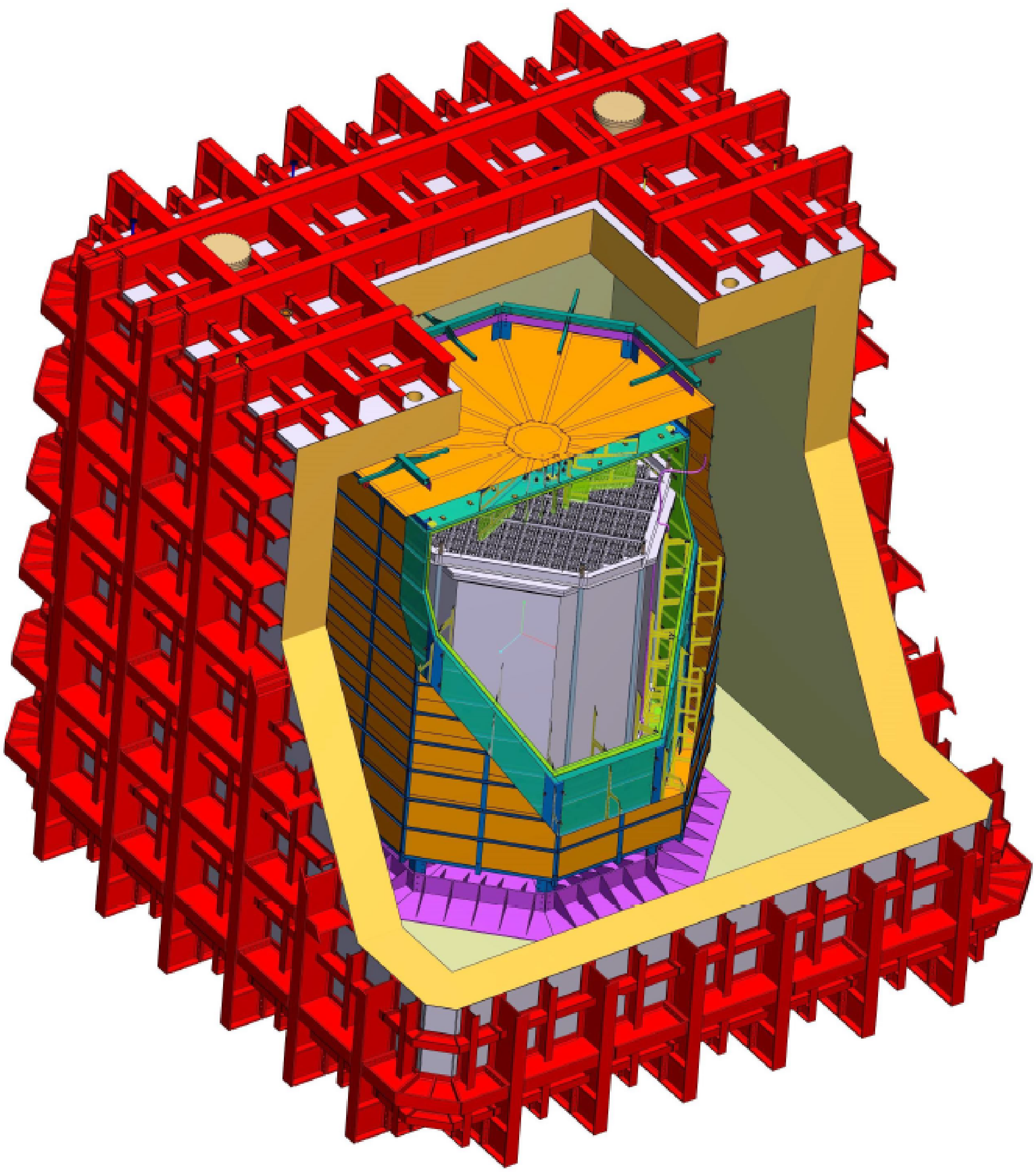

Figure 2.3: DarkSide-20k detector. Octagonal TPC filled with UAr liquid argon (grey) and contained in sealed acrylic (PMMA) vessel. Top and bottom plane of the PMMA vessel has Photodetector modules to obtain scintillation read-out. PMMA sealed TPC is surrounded by veto detector system (Gd-doped acrylic shell (green) sandwiched between two active atmospheric liquid argon volumes: Outer Argon Buffer (OAB) and Inner Argon Buffer (IAB)) , all contained in protoDune-style cryostat (red).

unit in DarkSide-20k will be a photodetector module (PDM), consisting of a large tile of SiPMs. Each PDM unit consists of 24 SiPMs and covers an area of 50 $mm \times 50$ mm. The top and bottom scintillation-read assemblies will have 4140 PDMs each. The PDMs will be located above the anode and below the cathode which covers the top and bottom faces of the LAr TPC active volume. The PDMs collect both S1 and S2 signals with high efficiency.

Table 2.1: Some design parameters for DarkSide-20k TPC

Parameter	Value
TPC drift length	350 cm
Octagonal inscribed circle diameter (87 K)	350 cm
Active LAr mass	49.7 t
Fiducial LAr mass	20.2 t
Drift field	220 V/cm
Extraction field	2.8 kV/cm
Luminescence field	4.2 kV/cm
Gas pocket thickness	(7 ± 0.5) mm
Grid wire spacing	3 mm

DarkSide-20k is expected to achieve the sensitivity to WIMP-nucleon cross sections of $7.4 \times 10^{-48} cm^2$ ($6.9 \times 10^{-47} cm^2$) for 1 TeV/c^2 (10 TeV/c^2) WIMPS with 200 tyr exposure. At this sensitivity, DarkSide-20k also expects to detect a few events from coherent elastic scattering of atmospheric neutrinos off argon nuclei. The DarkSide-20k detector will either detect a WIMP or will exclude a large fraction of the favored WIMP parameter space. The ultimate goal of the GADMC is the construction of the ARGO detector, which will have multi-hundred tons of fiducial LAr mass. ARGO is expected to reach the experimental sensitivity of detecting WIMPs or exclude much of the WIMP parameter space down to the neutrino floor for WIMP masses from 1 GeV/c^2 to several hundreds of TeV/c^2 [6].

2.4 Scintillations in Liquid Argon

The process of liquid argon (LAr) scintillations is described in great detail in [115] [116] [117]. When a particle scatters in LAr, it will either scatter from an electron orbiting an argon atom or from the argon nucleus. The charged particle moving through LAr loses energy continuously via ionization or excitation of Ar atoms. The charged particle may also cause the nucleus to recoil. Some of the energy of a recoiling nucleus get transferred to electrons directly by the recoiling nuclei or by a recoiling nucleus, while some energy is dissipated as heat. Scintillations from LAr arises from the formation of Ar exciton (Ar^*) or ion (Ar^+), produced by the interacting/ionizing particle.

The Ar exciton Ar^* can bond with ground state Ar to form weakly bound Ar_2^* dimer. Ar_2^* then decays into a ground state emitting a photon. This process, known as exciton self-trapping is described by:

$$Ar^* + Ar \rightarrow Ar_2^* \tag{2.1}$$

$$Ar_2^* \rightarrow 2Ar + h\nu \tag{2.2}$$

Alternatively, an argon ion (Ar^+) may bond with an atom in the ground state to form a charged dimer Ar_2^+. These can capture a free electron to form a doubly excited Ar^{**}. The Ar^{**} then makes a non-radiative transition to a singly-excited dimer, Ar^*. The scintillation can proceed through exciton self-trapping. This scintillation mechanism is called recombination luminescence and is described by the sequence;

$$Ar^{+} + Ar \rightarrow Ar_2^{+}$$

$$Ar_2^{+} + e^{-} \rightarrow Ar^{**}$$

$$Ar^{**} \rightarrow Ar^{*} + heat$$

$$Ar^{*} + Ar \rightarrow Ar_2^{*}$$

$$Ar_2^{*} \rightarrow 2Ar + h\nu$$

A dimer Ar^{**} is in a Rydberg state, where Ar_2^{+} core is orbited by a bound electron. Depending on the orientation of spins of the Ar_2^{+} core and the bound electron, $Ar^{*}*$ can be in singlet state (when spins are anti-parallel) or triplet state (when spins are parallel). The singlet state decay is allowed by all selection rules and occurs on a short time scale of 6 ns [118]. The triplet state decay, however, occurs on much longer time scale of 1600 ns. In either case, the energy is released as a UV photon with wavelength 128 nm.

The maximum number of photons produced per deposited energy E_{dep} can be given by [116]:

$$N_{ph} = N_i + N_{ex} = N_i(1 + N_{ex}/N_i) = \frac{E_{dep}}{W}(1 + N_{ex}/N_i) \tag{2.3}$$

where N_i and N_ex are the number of ions and excited atoms (excitons) produced by the incoming particles, respectively. Here, W is the average energy of the ion-electron pair and is ~ 24 eV for liquid argon [119].

The mechanisms by which electronic recoils and nuclear recoils lose energy to excitation and ionization is different, so, the exciton-to-ion ratios differ. The exciton-ion ratio (N_{ex}/N_i) in LAr is 0.21 for electronic recoils, and ~ 1 for nuclear recoils[115]. For electronic recoils in liquid argon , the effective W for scintillation $W_ph = W/(1+N_{ex}/N_i)$ is 19.5 eV. So, N_{ph}, the number of photons produced for keV energy deposited is approximately ~ 50. This shows argon is an efficient scintillator.

The scintillation signal in LAr has a fast component (resulting from the singlet state decay) and a slow component (resulting from the triplet state decay). Although the decay times do not depend on the ionization density of the particle's track, but the singlet-to-triplet ratio (N_s/N_t) does [118], and this ratio N_s/N_t is larger for nuclear recoils than for electronic recoils.

Ar^* (excitons) can lose energy by non-radiative transitions [120][121]. N_{ex}/N_i is larger for nuclear recoils than that for electronic recoils. Also, dE/dx is greater for nuclear recoils, so, nuclear recoils leave a denser track of excitons/ions. This is also why the ion-electron recombination probability for nuclear recoils is greater. Due to these effects, the scintillation yield for nuclear recoils is smaller than for electronic recoils (by a factor of 0.25) [121].

In general, total scintillation yield also decreases in the presence of a drift field. This is because the recombination luminescence is suppressed as the electrons drift away from the event sites. In DarkSide-50, the null-field and field-on scintillation yields for electronic recoil events are approximately 8 PE/keV and 7 PE/keV, respectively [9].

2.5 Pulse Shape Discrimination

As discussed in Section 2.4, the scintillation signal in liquid argon has a fast component($\sim$ 6 ns) and slow component ($\sim$ 1600 ns) resulting from the singlet state and triplet state excimer decays, respectively. The relative population of the fast (singlet) and slow (triplet) components is strongly correlated with the ionization density (hence the nature of the primary ionizing particle and the deposited energy). Typically, nuclear recoil events create $\sim 70\%$ of singlet dimers. This provides the way to distinguish between nuclear recoils and electronic recoils events. DarkSide uses a $f90$ parameter. Here, $f90$ is the fraction of the scintillation signal (in units of photoelectrons (PE)) in the first 90 ns of S1 pulse. In the first 90 ns, almost all the singlet dimers will have decayed, while only a few triplet dimers will have decayed. The $f90$ is ~ 0.7 for nuclear recoils, and ~ 0.3 for electronic recoils.

Two distinct bands of electronic recoil events and nuclear recoil events are seen in the f90 vs S1 plot (shown in Figure 2.4). Though the number of electronic recoils dominates, the discrimination based on the f90 parameter allows efficient rejection of the electronic recoil backgrounds. The Discriminating power is the number of events that can be rejected as electronic recoil events for every event incorrectly classified as nuclear recoil, for some nuclear recoil acceptance level. DarkSide-50 demonstrated the discriminating power of 10^7 [7] using pulse shape discrimination based on the f90 parameter alone.

2.6 Dual-phase Liquid Argon Technology

The DarkSide program uses dual-phase argon TPC to detect both S1 and S2 signals for each event. The active volume consists of liquid argon. Above the LAr volume is a thin gas layer. When a particle interacts in liquid argon, it can produce a prompt scintillation signal, S1, and ionization electrons. The ionization electrons that escape recombination drift

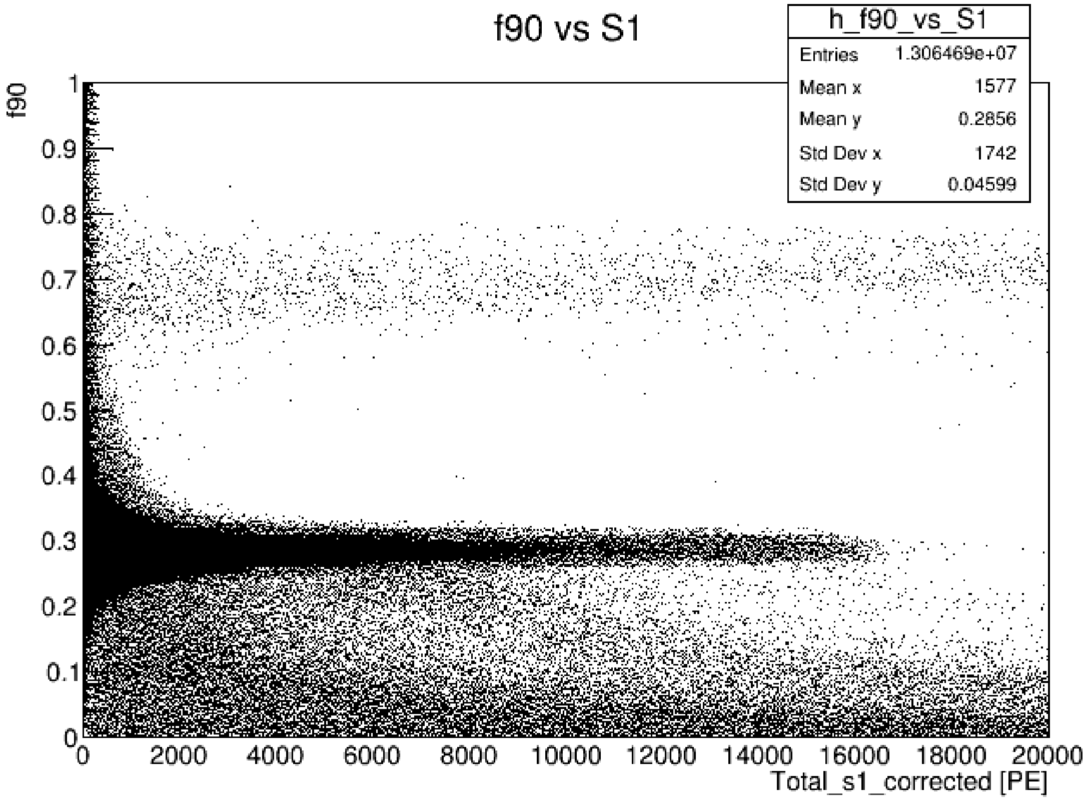

Figure 2.4: The $f90$ vs $S1_{corr}$ plot for events in 532-day DarkSide-50 data-set after applying some nominal data quality cuts. Electronic recoil events form a f90 band around $\sim$ 0.3 while nuclear recoil events have f90 $\sim$ 0.7. $S1_{corr}$ is S1 corrected for drift time and radial dependence.

in the uniform electric field and are extracted into the gas layer. The less dense gas in this layer allows the electrons to excite argon atoms in the gas. These argon atoms de-excite and release secondary scintillation S2. For the same size S1, nuclear recoils have a smaller S2 signal compared to electronic recoils. Thus, the pulse shape discrimination on S1 (based on f90 parameter) and $S2/S1$ ratio allows a powerful rejection of electronic recoil backgrounds.

Dual-phase technology allows an efficient position reconstruction of any event occurring in TPC. The timing between S1 and S2 (effectively, the drift time of the ionization electrons) gives z position information of the event. Since the drift field is uniform across the TPC, the electron drift velocity is constant across the active volume. In DarkSide-50 TPC, the drift field is maintained at 200 V/cm, and the electron drift velocity is $\sim$ 1 mm/μs [122]. The z-coordinate for the event can be determined with sub-mm precision. The S2 distribution in the PMTs gives the x-y position of the event. The x-y position resolution is on the order of 1 cm in DarkSide-50. A better x-y resolution will be achieved when small units of Silicon photomultipliers (SiPMs) are used in DarkSide-20k. The 3D position reconstruction also allows fiducialisation of the active volume. This removes most of the surface backgrounds originating in the materials surrounding the TPC.

The nuclear recoils induced by low-mass WIMPs (few GeVs) are on the order of a few keVs. In this regime, the efficiency for detecting the S1 signal is low, and f90-based PSD is not available. However, an S2-based search allows the experiment to achieve a much lower threshold and be sensitive to low-mass WIMPs.

2.7 Use of Low Radioactivity Argon

^{40}Ar is abundant in atmosphere (0.934%) and the commercial production is relatively inexpensive. Natural argon is mostly ^{40}Ar which is not radioactive. But there is also a small concentration of cosmogenically activated radioactive isotopes of argon, mainly ^{39}Ar, ^{37}Ar, ^{42}Ar. The ^{39}Ar concentration is relatively high in atmospheric argon (AAr), with the specific activity $\sim$ 1 Bq per kg [9][10]. The high activity of ^{39}Ar poses some significant challenges. When DarkSide-50 TPC was filled with AAr, the DarkSide-50 event statistics were dominated by ^{39}Ar β-decays. The ^{39}Ar decays dominated the trigger rate, and there were a significant pile-up of events due to a drift time of several hundred μs. This will pose an even greater challenge in larger detectors (with larger TPCs). Further, the large number of ^{39}Ar events decreases the sensitivity for a WIMP search, especially with leakage of electronic recoil background in the nuclear recoil region.

^{39}Ar in atmosphere is produced by cosmogenic activation on ^{40}Ar through $^{40}Ar(n,2n)^{39}Ar$

and similar reactions [123]. The underground argon is cosmogenically shielded and can have a reduced concentration of ^{39}Ar. Such underground sources of argon were discovered [124][125]. Kinder Morgan facility[125] extracted underground argon (UAr) from wells in Western Colorado for DarkSide. The purification and distillation of the argon was carried out at Fermilab [126]. In April 2015, DarkSide-50 TPC was filled with the low-radioactivity argon [14], and the data acquisition began. The ^{39}Ar activity was found to be a factor of 1400 times smaller than in atmospheric argon.

The large scale procurement and purification of UAr is crucial for next-generation GADMC detectors, DarkSide-20k and ARGO. The Urania project will extract and purify the UAr from the CO_2 wells at the Kinder Morgan Doe Canyon Facility located in Cortez, CO, with a production rate of several hundred kgs per day [6]. The Aria project will carry out chemical purification of extracted argon before it is filled in the LArTPC. Aria consists of two 350 m tall distillation columns of different processing diameters, Seruci-I and Seruci-II, capable of separating isotopes by means of cryogenic distillation. Apart from reducing the concentration of the ^{39}Ar isotopes from already ^{39}Ar-depleted Argon, the process will also decrease the traces of N_2, O_2, Kr to the acceptable levels.

2.8 G4DS:DarkSide Monte Carlo Tool

G4DS is a DarkSide's GEANT4-based Monte Carlo simulation code [8][127][128] designed to simulate the response of DarkSide detectors, DarkSide-10, DarkSide-50, and DarkSide-20k. For each of the detectors, G4DS provides a rich set of particle generators, detailed geometries, real data tuned physical processes, and the full optical propagation of the photons produced by scintillation in liquid argon and electroluminescence in gaseous argon [8]. The goals of G4DS are to 1) accurately describe the light and energy response of DarkSide detectors, 2) tuning of the analysis cuts and efficiency estimation, 3) prediction of nuclear and electronic

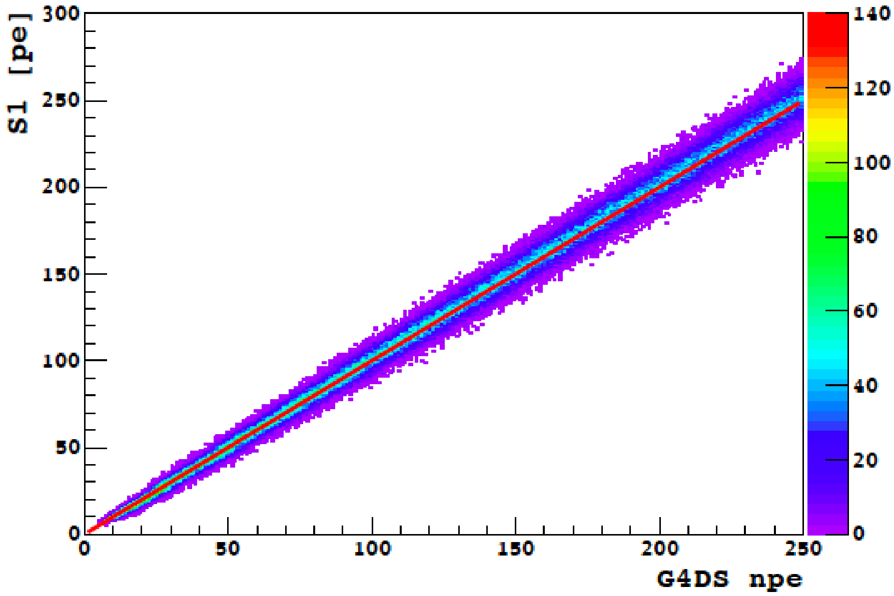

Figure 2.5: Reconstructed S1 as a function of number of PE generated by G4DS (DS-50). The deviation from linearity (red line) is percent level. Figure taken from [8].

backgrounds, and 4) definition of the signal acceptance band. G4DS tracks all the generated photons until they reach the photosensors, where these are converted to photoelectrons (PE) stochastically based on the quantum efficiency. The conversion of photoelectrons into charge uses electronics simulation.

The processes leading to scintillation and ionization are parameterised in G4DS based on a Precision Argon Response Ionization and Scintillation (PARIS) model [8]. PARIS is a simplified and effective model that was tuned to reproduce DarkSide-50 data. With an excellent agreement found between Monte Carlo and the data, the PARIS approach could be used for future DarkSide/GADMC detectors. The fundamental principles governing the ionization and scintillation processes in LAr is built into the PARIS Model. In G4DS, the fraction of recoil energy that produces scintillation (including quenching factor for nuclear recoils), is translated into the number of photo-electrons by applying poisson smearing and using light yield determined from the calibrations.

The electronics simulation is carried out using DarkArt software. This is the same framework that was used for data reconstruction for DarkSide-50. For DarkSide-50, the DarkArt simulation module generates the waveforms PMT-channel-wise. Channel level raw waveforms added with noise (obtained from various data campaigns) constitutes a simulated waveform. The simulated waveforms are further processed through the reconstruction code that carries out baseline subtraction, and identification of pulses, and reconstruction of the variables like S1, S2, f90 for each event. The difference between the reconstructed S1 variable and the true number of photo-electrons generated by G4DS in DarkSide-50 is $\sim 1.1\%$ [8]. The smearing introduced by the electronics and the reconstruction algorithms is estimated to be $\sim 5\%$.

G4DS is also built to track and process the events generated by FLUKA and TALYS simulation codes. FLUKA was mostly used to study cosmogenic neutron background and cosmogenic isotope production, while the TALYS code has been used to study (α,n) reactions.

2.9 Summary of DarkSide's Successes

DarkSide-50 experiment didn't detect a WIMP signal. But it demonstrated that the sensitivity required to detect WIMP dark matter is achievable with the use of dual-phase LAr technology, using efficient background suppression and discrimination techniques. Despite the null results for WIMP, DarkSide-50 was able to exclude large fraction of WIMP-hypothesis parameter space. Following the successful and stable operation of the DarkSide-50 detector (along with the physics success of the experiment), efforts are already underway to build a larger detector DarkSide-20k. The Next-generation detectors DarkSide-20k and ARGO will be built and commissioned by GADMC (The Global Dark Matter Collaboration). The goal is to search for WIMPs down to the neutrino floor.

DarkSide-50 carried out the first dark matter search with atmospheric argon (AAr) data acquired in 2013-2014, and the results were published for an exposure of 1422 ± 67 kgd in 2015 [7]. The DS-50 TPC was filled with underground argon (UAr) in 2015 [14]. The measurements found the ^{39}Ar activity was suppressed by a factor of ~ 1400. And DarkSide reported the results from the analysis of 70.9 days of UAr data [14]. For a combined exposure of AAr and UAr runs, DarkSide set an upper limit on WIMP-nucleon cross-section at 2 $\times 10^{-44}$ cm^2 (8.6×10^{-44} cm^2, 8.3×10^{-43} cm^2) for a WIMP mass of 100 GeV/c^2 (1 TeV/c^2, 10 TeV/c^2).

The DarkSide published the results of WIMP search in 532.4 live-day exposure of the DarkSide-50 detector [9]. The total exposure for the analysis was (16660 ± 270) kgd. A "blind analysis" was performed on the 532-live day data set. The candidate selection/background rejection criteria was designed, and the background surviving cuts were estimated, without the knowledge of the number of properties of events in the final WIMP search region. Expected background of 0.1 event was considered acceptable resulting Poisson probability of $< 10\%$ of observing one or more background events in the search region. The details of blind analysis techniques and background predictions can be found in [9]. On applying the analysis cuts, and then unblinding the data, no event was observed in the pre-defined search region. Figure 2.6 a) shows the f90 vs S1 plot after all the analysis cuts.

Figure 2.6 b) shows the increased separation between the DM box and the background events, when tighter radial and S2/S1 cuts are imposed. In multi-ton detector DarkSide-20k, these additional cuts would provide additional background rejection at little loss in signal efficiency.

In the blind analysis of 532.4-day data, no event was found in the pre-defined DM-search box. A limit on spin-independent DM-nucleon cross-section was derived assuming the standard isothermal WIMP halo model ($v_0 = 220\ km/s,\ v_{esc} = 544\ km/s, v_{earth} = 232\ km/s,\ \rho_{dm} = 0.3\ GeV/(c^2 cm^3)$. A 90% C.L exclusion curve (shown in Figure 2.7)

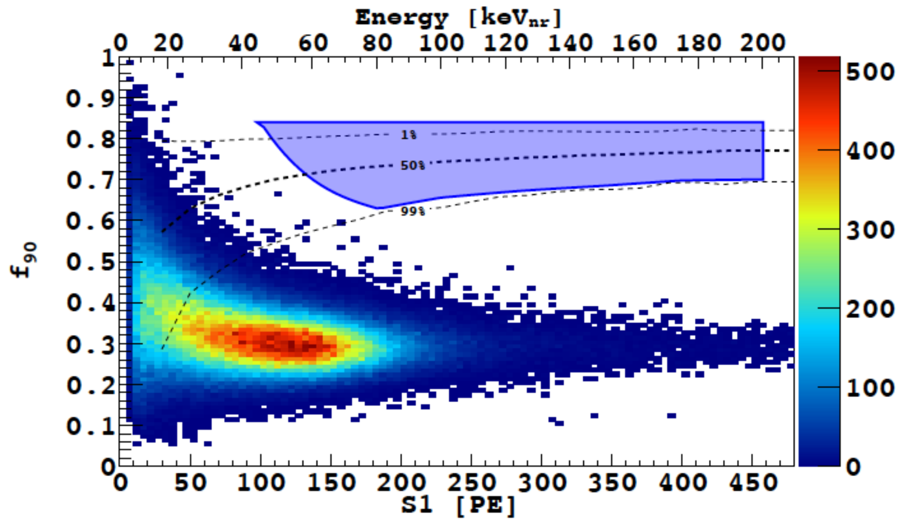

(a)

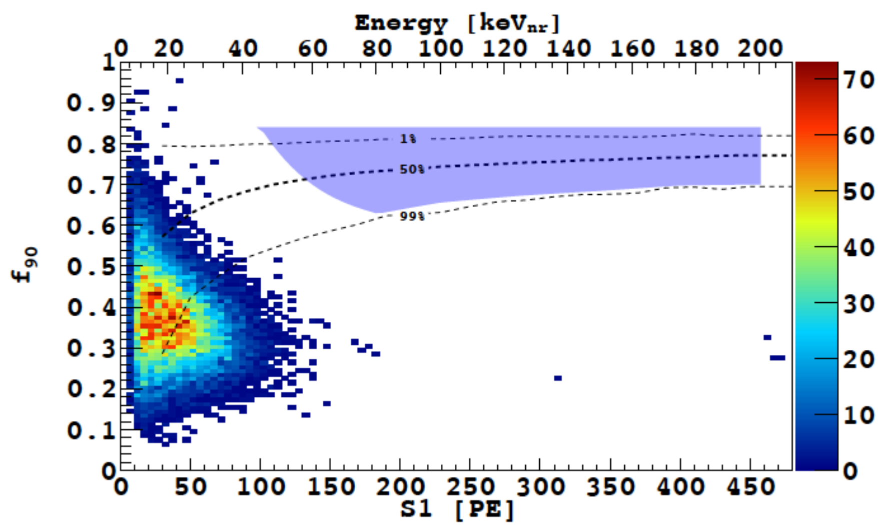

(b)

Figure 2.6: Distribution of events in f90 vs S1 that survived analysis cuts. No candidate event in the DM box (region within the outlined blue solid line) was observed. The 1%, 50%, and 99% f90 acceptance contours for nuclear recoils, as derived from fits to $^{241}AmBe$ calibration data are shown as the dashed lines. The plot 2.6 b) is the f90 vs S1 distribution when the tightened radial and S2/S1 cuts are implemented. Figure taken from [9].

was derived corresponding to the observation of 2.3 events DM-induced spin-independent scatterings. The minimum upper limit is 1.09 $\times 10^{-44}$ cm^2 at 126 GeV/c^2.

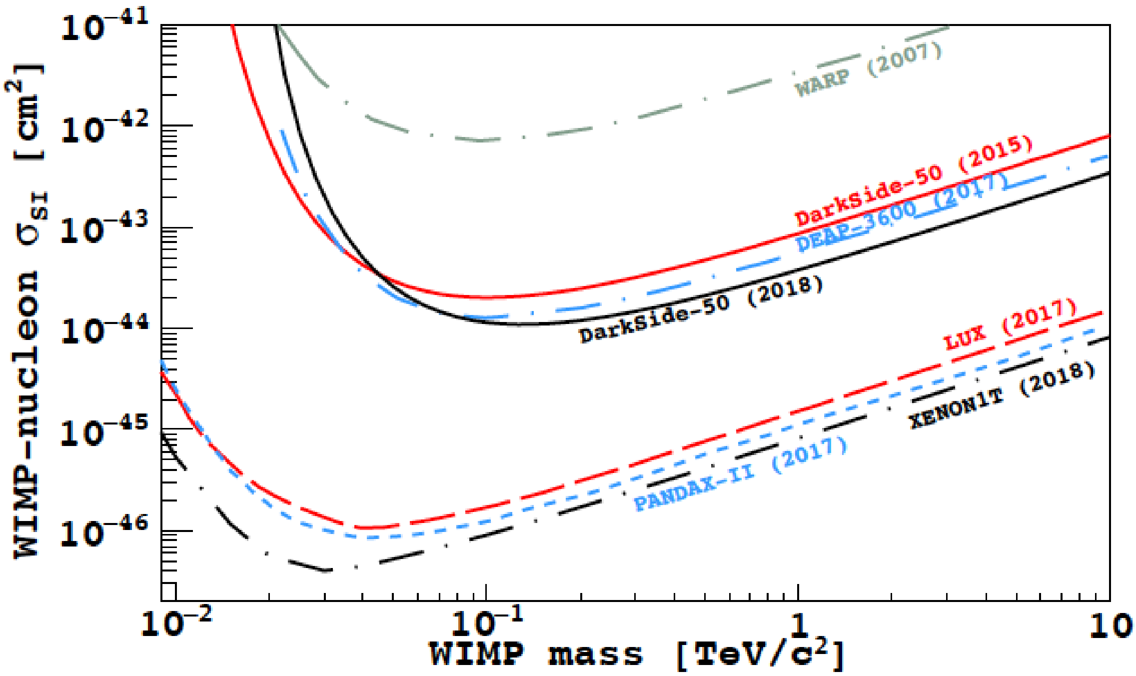

Figure 2.7: The spin-independent DM-nucleon cross section 90% C.L. exclusion limits. The exclusion curve derived from DS-50's 532-day analysis is represented by the solid black. The exclusion curve from earlier 70-day analysis is in the red solid line. The exclusion curves from few other experimental projects WARP [10], Xenon1T [11], Pandax-II [12], LUX [13] are shown for comparison. Figure taken from [9].

The DarkSide published its results for an S2-analysis based low-mass dark matter search. This is discussed in greater detail in [104]. The search was with a much lower recoil analysis threshold (0.6 keV_{nr}) and was sensitive to DM masses to 1.8 GeV/c^2. The low-mass WIMPs produce low nuclear recoils (on the order of a few keV_{nr}). In that regime, the S1 signal is small or undetectable. The required low recoil energy analysis threshold is achieved by exploiting the ionization signal S2. Above 30 PE, the pulse finding algorithm can detect S2 with 100% efficiency owing to the high S2 yield of 23 ± 1 PE per electron extracted. The analysis led to the most sensitive limit on WIMP-nucleon scattering cross section for low-mass WIMPs ($5\ GeV/c^2 < mass > 1.8\ GeV/c^2$).

The DarkSide-50 data has also been used in a search of sub-GeV dark matter candidates [107] interacting through a vector mediator with couplings smaller than the weak scale. [129] [130] [131]. Light DM may couple to electrons. Since electrons are lighter than the target nucleus, the electrons absorb more efficiently the kinetic energy in the light DM than the nuclear target. The 540-day data set was used for the analysis, and upper limits for DM-nucleon scattering was set for two DM form factor assumptions: $F_{DM}(q) \propto 1/q^2$ and $F_{DM}(q) = 1$ at 90% C.L [107].

Chapter 3

Backgrounds to Dark Matter Searches in DarkSide-50

The WIMP signal is a low energy (keV to hundreds of keV) nuclear recoil. And the expected WIMP rate is on the order of few events per ton of target material per year. Since WIMP events are so rare, almost all the data acquired are background events of some type. In general, the backgrounds can be radiogenic backgrounds (intrinsic backgrounds due to radioactivity from the target material itself or from surrounding detector materials) or cosmogenic backgrounds (backgrounds from cosmic-ray muons or muon-induced secondaries). Two major types of backgrounds are electronic recoil (ER) backgrounds and nuclear recoil (NR) backgrounds. The ER events mostly result from Beta (β) or gamma (γ) scattering in liquid argon. While NR events mostly result from alpha (α) or neutron (n) scattering in the argon. The backgrounds for dark matter searches in DarkSide detectors are briefly discussed in this section.

3.0.1 Beta-gamma Backgrounds

β and γ can induce electronic recoils in liquid argon. Most of the γ's originate from the radioactivity of the detector materials or the surrounding cavern walls. In DarkSide-50 and DarkSide-20k, one of the major β emitters is ^{39}Ar. ^{39}Ar is present in liquid argon volume. The ER backgrounds from βs and γ's do not pose a significant challenge for a WIMP search. The LArTPC technology allows efficient discrimination of β-γ backgrounds based on the powerful PSD parameter f90. Some major sources of β and γ backgrounds in DarkSide-50 are the following:

^{39}Ar

^{39}Ar is a long-lived radioactive isotope of Ar (half-life of 269 years). Its origin is mostly cosmogenic with major production channel being ^{40}Ar(n,2n)^{39}Ar reactions. ^{39}Ar beta-decays with an end point energy of 565 keV. The concentration of ^{39}Ar is small in natural argon. But β's from its decay deposit almost all the energy in the sensitive volume. DarkSide reported the ^{39}Ar β specific activity of $\sim$ 1 Bq/kg [7] in AAr. In DarkSide-50, ^{39}Ar dominated the trigger rate. With the use of cosmogenically shielded underground argon (UAr), DarkSide reported the specific activity of ^{39}Ar to be $\sim$ 0.73 mBq/kg.

^{85}Kr

^{85}Kr is found in small concentration in both AAr and UAr. In the atmosphere, ^{85}Kr can be produced by cosmogenic activation through the ^{84}Kr(n,γ)^{85}Kr reactions, and also by fission of uranium and plutonium in nuclear reactors [132][133]. Similar fission reactions in the earth's crust are also expected to produce ^{85}Kr as found in the UAr extracted by the DarkSide [14]. Primarily, ^{85}Kr β-decays to ^{85}Rb with a half-life of 10.7 years and end-point energy of 687 keV. In UAr, DarkSide-50 measured the specific activity of ^{85}Kr to be

$\sim$ 2mBq/kg [14]. No attempt was made to remove Kr from the UAr for the DS-50, as the presence of ^{85}Kr was not expected at the time of purification. For DarkSide-20k, the activity of ^{85}Kr will be much lower as the bulk of the Kr will be removed during the purification of UAr [6].

^{60}Co

^{60}Co is a synthetic isotope primarily produced in nuclear reactors by neutron activation of the stable isotope ^{59}Co. A small concentration of ^{60}Co is present in stainless steel in the cryostat and PMTs of DarkSide-50 detector. It has a short half-life of 5.27 years, and β-decays to excited $^{60}Ni^{*}$ which decays and gives off two γ's (1.17 MeV and 1.33 MeV). These high energy γ's can penetrate the stainless steel and leave a signal in the TPC and the LSV. Some Co-60 γ's are detected in prompt coincidence between TPC and LSV.

^{40}K

^{40}K is a long-lived radioactive isotope ($\tau_{1/2} \sim 10^9$ years) of potassium. It has a natural abundance of 0.012% [134] in earth's crust. ^{40}K is present in stainless steel in the cryostat and the PMTs in the DarkSide-50 detector. The ^{40}K isotope predominantly β-decays to ^{40}Ca. These β's are usually not detected as they do not enter the sensitive volume and LSV. ^{40}K can also emit β^{+} leading to ^{40}Ar. The β^{+} annihilates with the β^{-} giving off two gammas of energies 511 keV each. ^{40}K can also undergo electron capture through the reaction: $^{40}K \rightarrow {}^{40}Ar + \nu_e + \gamma$. The resulting 1461 keV γ is easily detectable by the detector. Since the electron-capture reaction strips the electron from atomic shell, these reactions may be followed by a X-ray or an auger electron.

^{232}Th, ^{238}U, ^{235}U and their daughter isotopes

These isotopes have relatively long half-lives and are mostly primordial in origin. They are found in rocks and metals and are the contaminants in detector materials in a concentration affected by the radio-purity processes. Their full decay chains produce a series of daughter isotopes [135][136][137] which lead to stable Pb isotopes. There are β, γ, α, fissile neutrons backgrounds coming from these decay chains. ^{208}Tl, near the bottom of ^{232}Th decay chain, produces 2.6 MeV γ. This is the highest energy γ produced in any of the naturally present isotopes. The ^{214}Bi also decays by β or β+γ with a Q-value of 3.23 MeV. The fission of the isotopes especially, that of ^{238}U, typically leaves the nuclei in excited states leading to the emission of γ. These γ's are mostly coincident with the signal produced by fission-produced β, α, or n.

3.0.2 Neutron Backgrounds

Neutrons induce nuclear recoils in argon and are important backgrounds in WIMP dark matter searches. Since neutrons have higher scattering cross-section than WIMPS, they are more likely to undergo multiple scatterings in liquid argon. However, the nuclear recoil signal from a single-scattering neutron is identical to that of WIMPs. In DarkSide-50, the WCD shields inner volume from the neutrons originating in the detector surroundings. The LSV is a boron-loaded liquid scintillator. It acts as a neutron veto, actively tagging neutrons based on their captures on ^{8}B, ^{14}C , and ^{1}H. The neutron captures results in γ photons that are detectable with high efficiency. Neutrons may be radiogenic (originating within the detector materials or surroundings) or cosmogenic (induced by muons or its secondaries interacting in the detector).

Radiogenic neutrons

The neutrons that originate in detector materials or the surroundings are "radiogenic" neutrons. Most of these neutrons originate from the isotopes ^{232}Th, ^{238}U, ^{235}U that are present in the cryostat, the PMTs, and other surrounding materials. Therefore, the radiogenic neutron event rate depends on the concentration of these isotopes in the detector materials. These isotopes or their daughters can produce neutron by spontaneous fission and (α, n) reactions. The spontaneous fission reactions, as in ^{238}U, often generate multiple neutrons and coincident high energy γ's. While the neutrons that originate from (α, n) reactions are particularly dangerous backgrounds. The α's from the isotopes in the decay chain of ^{232}Th, ^{238}U, ^{235}U may interact with the detector material and release neutron(s). The (α, n) neutrons are often produced with no accompanying γ's. Although, the delayed coincidence of α with n helps identify some of these events. Most dangerous events are those in which α deposits energy deeper into the detector-materials and have only a neutron scatter in the sensitive volume.

Cosmogenic neutrons

The cosmic-ray muon interactions with the detector materials and the surroundings can produce neutrons. These "cosmogenic" neutrons mostly originate from muon induced spallation. These neutrons are typically have much higher energies than the radiogenic neutrons, and hence, are much harder to shield but also easier to veto. Most of the cosmogenic neutrons have several MeV of energies and scatter multiple times in the detector. The cosmogenic neutrons are often produced as part of a particle shower and are accompanied by other neutrons and charged particles, some of which may be detected by the LSV and TPC. Any cosmogenic neutron interactions in TPC can also be vetoed based on Cherenkov radiation that may be produced by the parent muon or its secondaries passing through WCD.

3.0.3 Alpha Backgrounds

The decay chain of ^{232}Th, ^{238}U, ^{235}U have alpha (α)-emitting isotopes. In DarkSide-50, the dominant α-emitters of interest are ^{222}Rn and its daughter ^{210}Po. These isotopes may also be deposited on detector surfaces during fabrication and assembly or introduced into the circulating liquid argon during the experiment. An α decay produces an α-particle and a recoiling nucleus, both of which can induce nuclear recoils in liquid argon. The emitted α-particles typically have energies of several MeV. So, α-particles that deposit full energy in LAr volume do not pose a significant problem as the energy range is outside the WIMP region of interest. More dangerous backgrounds come from energy-degraded α's that deposit much lower energy in liquid argon having spent part of their energy in non-scintillating detector materials. For instance, ^{210}Po α decay results in an α (of energy 5.3 MeV) and a recoiling ^{206}Pb nucleus. If α deposits its entire energy in liquid argon, the resulting scintillation signal is large (on the order of thousands of PE). But if the α deposits smaller energy , S1 of the α and/or recoiling ^{206}Pb event may lie in the WIMP energy range. An α particle has a short range. So, most of the α events in TPC occur close to the inner surfaces of the TPC. These α backgrounds can be rejected by fiducialialization (i.e excluding the events from near the surface). Some α events depositing energy in TPB have been identified to have a characteristic S1-tail which provides an additional basis for discrimination [9][138].

3.0.4 Muon Backgrounds

The muon flux at 3800 m.w.e depth of LNGS is several orders of magnitude smaller than on the surface, while the mean energy of a muon is $\sim$ 280 GeV [139]. Muons interacting in the material can lose all or part of their energy through various mechanisms: 1) continuous ionization 2) bremsstrahlung 3) pair production 4) nuclear interactions. Typically, muon interactions can produce secondaries such as e^-, e^+, photons, neutrons, protons that may also leave a detectable signal in the detector. The muons entering the WCD and LSV produce high Cherenkov and scintillation signals, and are easy to veto. More concerning backgrounds are from cosmogenic neutrons produced by muon-induced spallation in the detector materials and the surrounding cavern. The muon-induced spallation on nuclei can also produce short-lived radioactive isotopes. These cosmogenically activated isotopes can also emit neutrons. The delayed neutrons produced by cosmogenically activated isotopes in the detectors can be dangerous backgrounds for WIMP dark matter searches.

3.0.5 Cherenkov Backgrounds

The high-energy electrons interacting in high refractive index detector-materials (Teflon, Fused silica, etc.) can produce Cherenkov signals. These electrons could be recoil electrons from Compton-scattering or energetic β's from radioactive decay. The Cherenkov signals have a fast time profile (f90 $\sim$ 1), and the signals usually concentrates on just one or a few PMTs. This information helps to reject most of the Cherenkov backgrounds. Particularly problematic events are those having both Cherenkov and electronic recoil signals. The signal from the recoiling electron and the Cherenkov signal produced by β or γ can make the event appear as a nuclear recoil.

3.1 Activity Measurement and Estimates in Detector Components

DarkSide launched an extensive program of assays to select radio-pure material, and to measure the residual activities. Most of the detector components were screened, and their activities measured before assembly. For example, The cryostat materials (stainless steel, flanges, nuts, bolts, pipes, Viton o-ring, insulation materials) were all assayed and screened before assembly [9]. The screened sample PMTs screened were not used in the detector. Typically, majority of radioactivity in PMTs comes from the borosilicate glass stem at the back of the PMT, the ceramic insulators supporting the dynodes, and the Kovar casing.

Background activity was estimated for various detector components using a spectral fitting technique which is discussed in [9][140]. A global energy variable, reconstructed from a linear combination of S1 and S2, was used to make the radioactivity estimates. The procedures and the fitting techniques are discussed in [9][141]. The sharing of energy deposited by an event is shared between scintillation and ionization in TPC. So, the combination of S1 and S2 is a more linear and high-resolution energy variable [9]. The combined S1-S2 electronic recoil energy scale is established by reconstructing γ-ray lines from the radioactivity in the detector [9]. Rate estimates are derived from fitting Monte Carlo (MC) energy spectra on energy spectrum from the data. The procedures are: 1) Obtain energy spectra from G4DS for various decay chains ^{232}Th, ^{238}U, ^{235}U , and for other isotopes ^{40}K, ^{60}Co for all their respective detector locations, and generate the energy spectra for ^{39}Ar, ^{85}Kr from G4DS. 2) Apply empirical smearing to the energies by drawing E_{smear} from a normal distribution with mean energy E and variance σ^2, where σ^2 is a function of E and some empirically obtained parameters. 3) Fit combined MC spectra on the data by constraining some components based on activities obtained from screening or measurements.

The fit is done iteratively, taking advantage of certain high energy γ-rays unique to the individual decay chains. The estimate of the PMT activity was based on MC based fit on the data utilizing the information from measured cryostat activities and that of ^{39}Ar, ^{85}Kr. The activities estimated from the procedure are presented in Figure 3.1.

Source	PMTs [Bq]		Cryostat [Bq]
	fitted	assayed	assayed
^{232}Th	0.277±0.005	0.23±0.04	0.19±0.04
^{40}K	2.74±0.06	3.0±0.4	$0.16^{+0.02}_{-0.05}$
^{60}Co	0.15±0.02	0.17±0.02	1.4±0.1
^{238}U^{low}	0.84±0.03	0.69±0.05	$0.378^{+0.04}_{-0.1}$
^{238}U^{up}	4.2±0.6	5.3±1.1	$1.3^{+0.2}_{-0.6}$
^{235}U	0.19±0.02	0.27±0.4	$0.045^{+0.007}_{-0.02}$
Liquid Argon Activity [mBq/kg]			
^{85}Kr	1.9 ± 0.1	^{39}Ar	0.7±0.1

Figure 3.1: The activities from various background components as reported in 532-day data analysis paper. The LAr components ^{39}Ar and ^{85}Kr activities are taken from [14]. Cryostat activities were fixed at assayed values and summed across all locations. The PMTs activity estimate was obtained by iterative fitting utilizing some γ peaks unique to the decay chain and the sum activity was obtained by summing for all 38 PMTs [9].

Chapter 4

$^{42}Ar/^{42}K$ background studies

Natural argon mostly consists of ^{40}Ar. There are also some cosmogenically activated long-lived radioactive isotopes like ^{39}Ar, ^{37}Ar, ^{42}Ar present in natural argon. The radioactivity from ^{42}Ar and its daughter isotope ^{42}K are expected to be small due to their trace natural concentration [142][123] . However, it is a potential source of background for next-generation liquid-argon-based experiments searching for dark matter and/or neutrino-less double beta decay ($0\nu\beta\beta$).

4.1 $^{42}Ar/^{42}K$

^{42}Ar isotope has a long half-life of 32.9 years. It β-decays into ^{42}K. The endpoint energy of the β-spectrum is 599 keV. ^{42}K is also radioactive and has a short half-life of 12 hrs. ^{42}K has two major decay modes. The primary decay mode goes directly to ground state ^{42}Ca, and produces β-spectrum with an endpoint of 3525 keV. This decay mode has a branching ratio (BR) of 81.9 %. ^{42}K can also β-decay with endpoint energy 2001 keV. This decay mode has a BR of 17.7 %. The resulting daughter isotope, ^{42}Ca, emits a 1524 keV γ to the ground state ^{42}Ca. The simplified decay scheme of ^{42}Ar is shown in Figure 4.1.

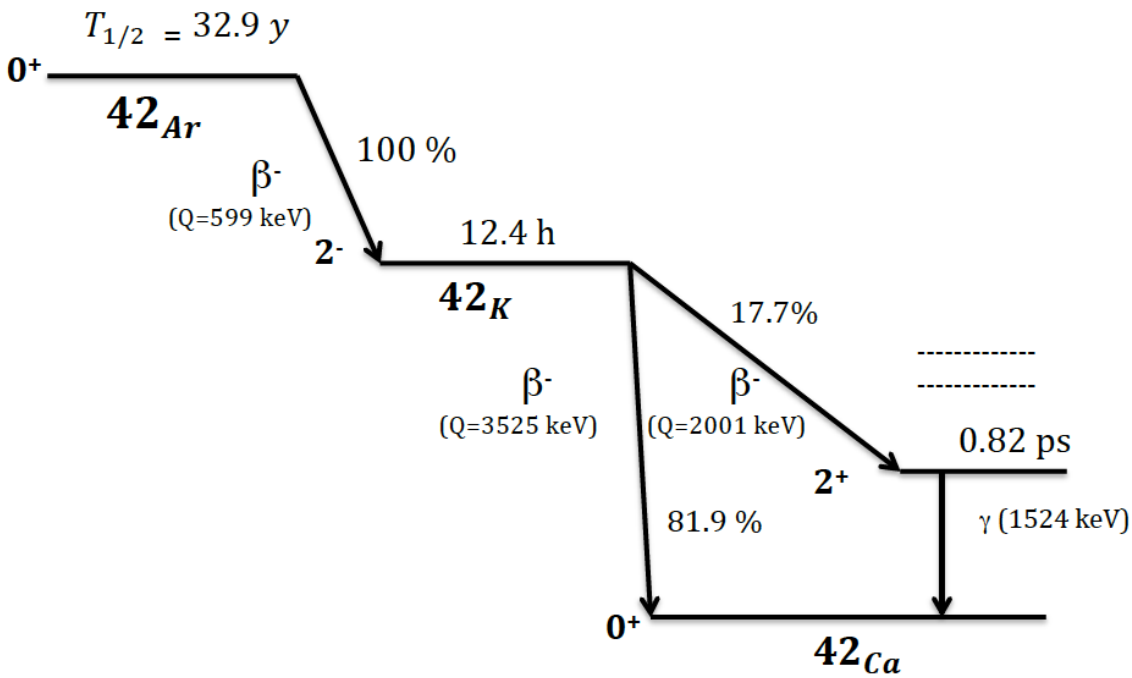

Figure 4.1: A simplified ^{42}Ar decay chain. ^{42}Ar β-decays to ^{42}K with the branching ratio 100%. Only major decay channels are included [15].

^{42}Ar is produced by activation in ^{40}Ar. ^{42}Ar may be produced by two step neutron capture reaction [123][143]:

$$1)\ ^{40}Ar + n \rightarrow {}^{41}Ar + \gamma$$

$$2)\ ^{41}Ar + n \rightarrow {}^{42}Ar + \gamma$$

^{41}Ar has a short half-life of $\sim$ 2 h. So, significant production of ^{42}Ar through this process requires a high neutron flux. An alternative channel of ^{42}Ar production is via the reaction $^{40}Ar(\alpha$,2p$)^{42}Ar$. This mode of production of ^{42}Ar is expected to be more significant in the upper atmosphere [142][143], where α's are abundantly produced by the cosmic ray interactions. The shape of beta spectra of Beta-emitting isotopes in the decay chain of ^{42}Ar (shown in Figure 4.1) can be computed from [144] ;

$$N(T)dT = C.P^2(Q-E)^2F(Z,P)S(P,Q)dT \tag{4.1}$$

where, P is the momentum of the β particle, Q is the end-point energy of the spectrum, T is kinetic energy of β-particle, F(Z,P) accounts for the Coulumb effects, S(P,Q) is the shape factor, C is the normalisation factor. With S(P,Q)=1 , the Equation 4.1 can be derived from Fermi theory of beta decay in the case of allowed beta transitions assuming all energy dependencies of nuclear matrix elements associated with the transition can be factored out [144]. To extend the equation to the allowed as well as forbidden-unique beta decays, all transitions leading to beta decays can be assumed to be allowed and “forbidden-ness” (or energy dependencies of the matrix elements defining the transitions) as well as other finer corrections can be incorporated in the shape factor S(P,Q). Some major β spectra observed in ^{42}Ar chain are shown in Figure 4.2.

The shape factor for first forbidden unique transitions leading to the ^{42}Ar β decay and ^{42}K (Q=3525 keV) β decay can be given by $S(P,Q) = Q^2 + \lambda P^2$ where λ carries an additional small-order correction. Here, for the ^{42}Ar β shape, the λ is assumed unity. The λ correction for the ^{42}K (Q=3525 keV) β shape factor is taken from [145]. For forbidden non-unique ^{42}K (Q=2001 keV) β spectra, the shape factor is also taken from [145]. The Fermi function, that accounts for Coulomb effects in the spectral shape, is taken from [146]. Any small error associated with the uncertainty in the shape factor and Fermi function translates to the normalisation factor, and affects the over all shape of the β spectra.

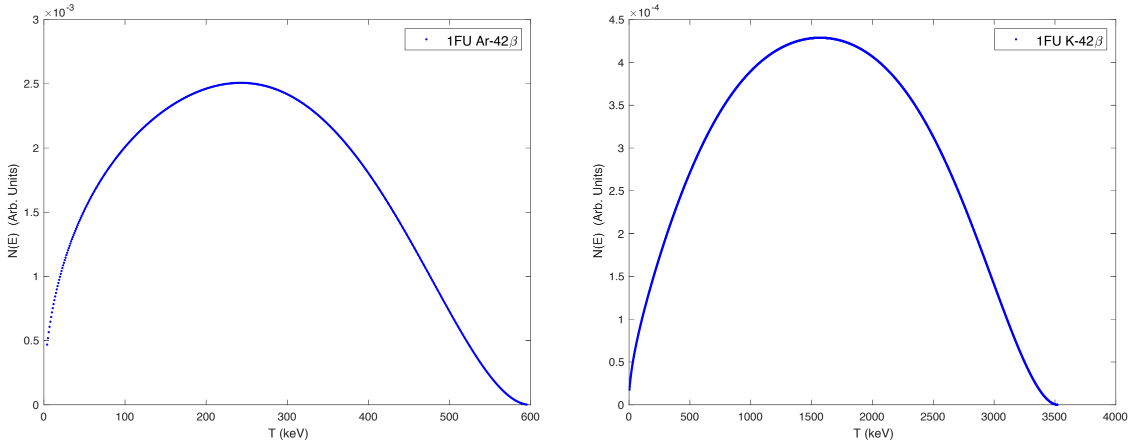

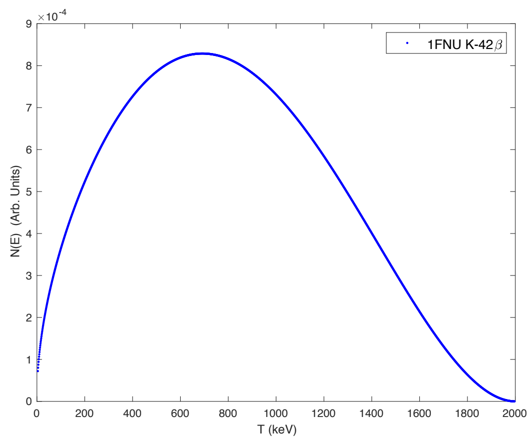

β-channels	BR	Transition	$\Delta J,\Delta\pi$	Nature of transition	Q (keV)
42Ar decay	100%	$0^+ \rightarrow 2^-$	2, -1	1st forbidden unique	599
42K decay	81.9%	$2^- \rightarrow 0$	2, -1	1st forbidden unique	3525
42K decay	17.6%	$2^- \rightarrow 2^+$	0, -1	1st forbidden non-unique	2001

Figure 4.2: The theoretical β-spectra for some major β-decay channels in ^{42}Ar chain and the details of transitions leading to the decays.

4.2 $^{42}Ar/^{42}K$ Background for Liquid Argon Based Low-background Detectors

^{42}Ar is a long-lived radioactive isotope ($\tau_{1/2} = 32.9$ y) of argon. $^{42}Ar/^{42}K$ decays can be important sources of background in large liquid argon based detectors. It is difficult to measure the background radioactivity from ^{42}Ar. The activity from ^{39}Ar is several order of magnitude larger than that of ^{42}Ar. The decays from both isotopes also have similar end-point energies. The β-spectrum of ^{42}Ar has an endpoint energy (Q-value) of 599 keV, while that of ^{39}Ar 565 keV. Also, both decays are first forbidden-unique decays, and their spectra have similar shapes. However, the potential β-γ signatures from ^{42}K decay chain could be detectable in large volume argon detectors. The GERDA experiment has observed the 1524 keV γ peak in its background energy spectrum [147]. The isotopes ^{42}Ar and ^{42}K are intrinsic to liquid argon. And their background could be important for next-generation DarkSide-20k that will have multi-tons of liquid argon in TPC and in veto. The energy deposition from the decays of ^{42}Ar and ^{42}K spans a large energy range keV to MeV. So, $^{42}Ar/^{42}K$ are potentially important for sensitivity studies in both low-mass to high-mass WIMPs searches. The $^{42}Ar/^{42}K$ concentration in AAr is not precisely known, and no study has been carried out in UAr.

Various experiments have measured the ^{42}Ar specific activity [142][147][148][149][150] in atmospheric argon. The estimated activity is on the order of few μBq/kg. The estimates for ^{42}Ar activity are often based on the ^{42}K activity measurements. The half-life of the ^{42}K is $\sim$ 12 h, and hence shorter than that of parent isotope ^{42}Ar. So, secular equillibrium is assumed to be established between ^{42}K and ^{42}K decays. With this assumption, the activity of ^{42}K is equal to that of ^{42}Ar in the detector.

The GERDA experiment [147] found ^{42}K may not be uniformly distributed within the liquid argon volume. In the presence of a uniform electric field, ^{42}K can gain charge, and then move towards electrodes. The GERDA experiment has run campaigns to estimate and mitigate the ^{42}K background. Especially ^{42}K β (Q=3525 keV) seem to be an important background for the $0\nu\beta\beta$ signal (2039 keV) searches in GERDA [151]. The GERDA's estimate for $^{42}Ar/^{42}K$ activity was based on the counts of 1524 keV γ signals. The DEAP-3600 experiment estimated the $^{42}Ar/^{42}K$'s activity to be 40.5 ± 5.9 μBq/kg [150]. This measurement was based on spectral fitting. In a single-phase detector (with no electric field across liquid argon volume) such as DEAP, the ^{42}K can be assumed to be uniformly distributed in the liquid argon. In the case of a dual-phase detector, however, it would be difficult to reliably estimate the activity (and concentration) of ^{42}Ar based on ^{42}K measurements.

4.3 Multidimensional Fitting

A Monte Carlo-based multidimensional fitting package was built for DarkSide-50 background studies [128]. The fit is based on a Chi-square (χ^2) minimisation, with χ^2 computed simultaneously in two-dimensional S1 vs drift time histogram and S1$_{late}$ spectra. The multidimensional spectral fitting technique has been used in estimating activity for background components, computing ^{39}Ar depletion factor in UAr, and in carrying out other background studies in the past. The Figures 4.3 and 4.4 show one example fit. The DarkSide's Monte Carlo package G4DS is used to generate the Monte Carlo spectra of radioactive isotopes in various detector components (cryostat, PMTs, sensitive volume).

S1, S1$_{late}$, tdrift

Three observable quantities were identified and obtained to break the degeneracy between the various spectra to make the fitting procedure more restrictive. The quantities are S1, tdrift and S1$_{late}$. The S1 vs tdrift spectra is generated for single-scatter events (i.e two pulse events). The S1 vs tdrift fit is carried out in the range S1 $<$ 6000 PE. At higher energies, the ADCs saturate, and reconstructed variable like S1 become unreliable. While S1$_{late}$ is defined as (1-f90)S1, the variable is little affected by the saturation as vertical saturation of ADCs is expected to be present only during first few tens of nano-seconds of a S1 pulse. However, there is a loss of resolution as (1 -f90) is typically 0.7 for electronic recoils. So, S1$_{late}$ fitting is done on data taken with a null-field configuration (at null field, the light yield is $\sim$ 8 PE/keV compared to 7 PE/keV with field-on). Unlike S1 spectra which is a featureless continuum, S1$_{late}$ includes all-pulses and shows prominent gamma absorption peaks as seen in Figure 4.4. The same radioactive isotope in the PMTs and cryostats can have similar S1 and $S1_{late}$ spectra, but their tdrift distribution are different. This makes the tdrift variable useful as it can break the degeneracy in the energy spectra. The decays of the same radioactive isotope can be simulated at different detector locations, and the spectra can be separately incorporated in the fitting.

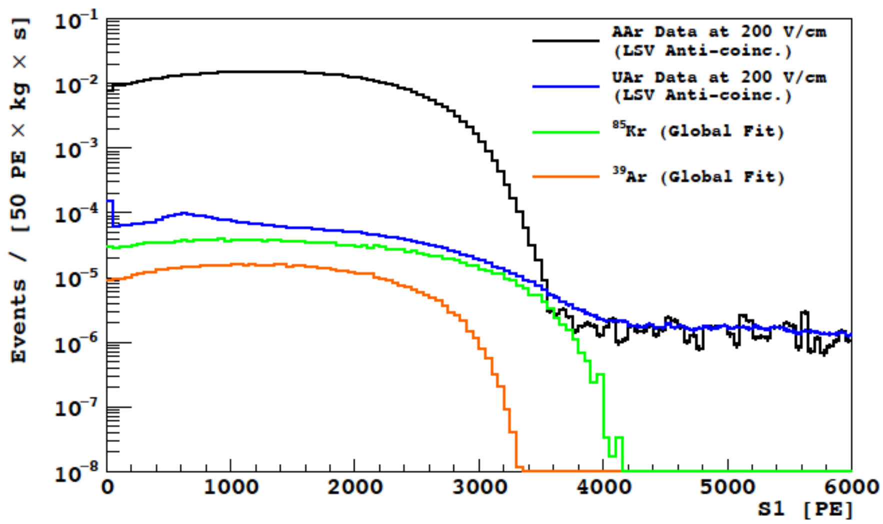

Figure 4.3: The Live-time normalised S1 pulse spectra for single-scatter events in AAr (black) and UAr (blue) taken at 200 V/cm drift field and MC fit (red) of data is shown. The Extracted MC fit for ^{85}Kr and ^{39}Ar are also shown. Peak at $\sim$ 600 PE are due to γ ray Compton scatterers. Figure taken from [14].

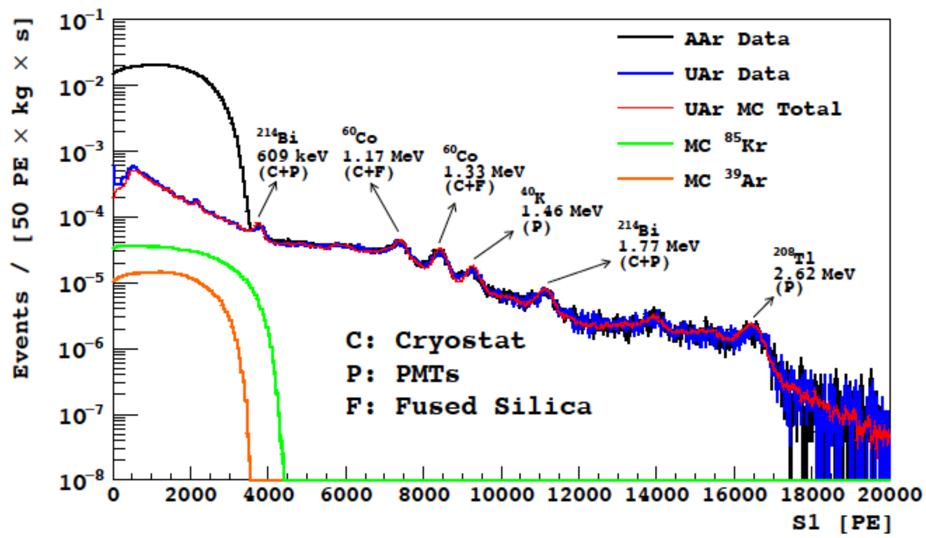

Figure 4.4: The Live-time-normalised S1-late integral pulse shape spectra in a null field (zero drift field) with AAr(black) and UAr(blue). A Geant4 MC fit (red) on the UAr data is shown. ^{85}Kr and ^{39}Ar activity spectrum is also shown as extracted from the MC fit. S1-late represents (1-f90)S1 component that is unaffected by the saturation in ADCs. Figure taken from [14].

Spectra corrections and normalisation

For the multidimensional spectral fitting studies, both field-on and field-off data are available. The S1 spectra are corrected for the z-dependence of the light yield. $S1_{late}$ spectra are obtained from field-off data taken during both AAr and UAr campaigns. In the field-off configuration, no tdrift information is available so a z-dependent top-bottom-asymmetry of S1 was exploited to correct for the $S1_{late}$. The event selection for both field-off and field-on data sets were required to pass a few basic data quality cuts: 1) All 38 PMT channels are found for the events 2) The baseline is found 3) The correct pulse start time is identified. In addition, the S1 vs tdrift spectra are built considering only single-scatter events (basically two pulse events). The accumulated lifetime for the data sets was computed after implementing these cuts.

The fitting code incorporates normalisation between S1 vs tdrift and $S1_{late}$ spectra on the basis of the different lifetimes of the data sets. The estimates of the normalisation factor between these single-scatter (for S1 vs tdrift) and multi-scatter data-sets (for $S1_{late}$) are effected by the systematics. One effect comes from the clustering algorithm that was used to reconstruct the pulse in the data . The algorithm is tuned for S1 $<$ 1000 PE. Another effect is the different pile-up probability of the pulses for the events in the data sets, which should have been accounted in the calculation of the lifetime. The aggregate effect of the systematics is expected at percent level in the estimate of normalisation factor between single scatter field-on and multiple scatter field-off spectra data-sets. To account for these systematics, a nuisance parameter was introduced in the fit minimisation procedure to weight the ratio between single and multiple scattering for each background components. The gaussian constraint included in the χ^2 computing forces the nuisance parameter to be close to one, but the parameter can also be weighted by the user to allow user-desired deviation of few % in the activity estimates from the fitting. The fitter considers the difference in statistics between MC spectra for the background components. The statistical errors are included in the χ^2 calculation.

4.4 $^{42}Ar/^{42}K$ fitting Studies in Underground Argon (UAr) Data

Full decay chains of ^{42}Ar and ^{42}K were separately simulated in G4DS with the assumption that the isotopes are uniformly distributed in LArTPC. S1 and S1$_{late}$ spectra were obtained from tpcene (energy distribution of events in TPC) spectra. The tpcene distribution for full ^{42}Ar and ^{42}K decay chains are given in Figure 4.6. In the ^{42}Ar tpcene spectra, the enhancement below < 600 keV comes dominantly from ^{42}Ar decays while the contribution above comes from from ^{42}K decays. It is possible to build S1 and S1$_{late}$ spectra from the tpcene variable itself using an appropriate energy-dependent light yield (obtained from the calibration campaigns [9][128]).

The S1$_{late}$ yield was obtained from the light yield calibrations with field-off data. Each of the prominent gamma peaks (observed in Figure 4.4) were fit with a gaussian after local background subtraction. The mean of their S1$_{late}$ values was divided by the true energy to obtain light yield. At very low energy, calibration was based on 41.5 keV peak from ^{83m}Kr. The light yield dependency on the energy is well-described by the Equation 4.2 :

$$LY_{late} = \frac{6.45}{1 + 0.07.e^{-E/0.13}} - 3.45 \times 10^{-5}.E \tag{4.2}$$

The LY_{late} and width of the gaussian peaks are used to build S1$_{late}$ spectra. An additional G4DS-tuned smearing was introduced to account for smearing induced by the charge

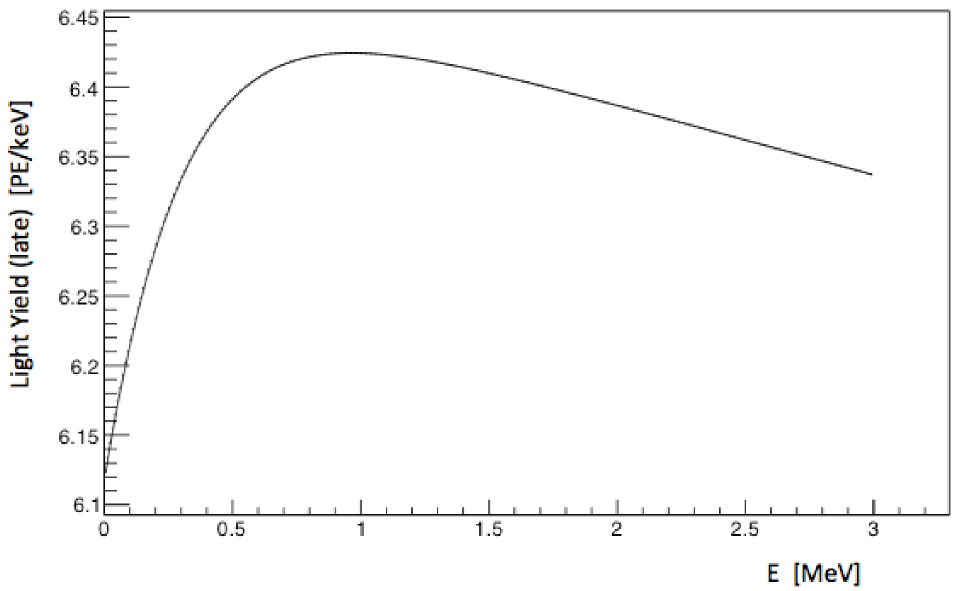

Figure 4.5: Null field light yield ($S1_{late}$)

integration in the PMTs.

The first approach implemented was to add all the spectral shapes of the background components in a weighted sum with weights (or activities) as free parameters. But the fitter shows degree of degeneracy between spectral shapes especially between components that have decays separately simulated at cryostat and PMTs. The "best-fit" gives 0 estimate for the activity of the "cryostat" or "PMT" component of certain isotopes.

The second approach is to fix the activities of of certain background components to the values obtained from the screening measurements and then estimate the activity of remaining components. But the measured activities also have uncertainties. Moreover, the original PMTs that were assayed for activity measurements were not deployed in DarkSide-50 detector. The activities of ^{85}Kr (activity was measured from analysis on 70 day data-set) and ^{60}Co may have changed during the preparation for 540 day data-taking.

For multi-dimensional fitting studies on UAr data, all major background components were included as reported in 3.1. The activities of the following components were fixed:

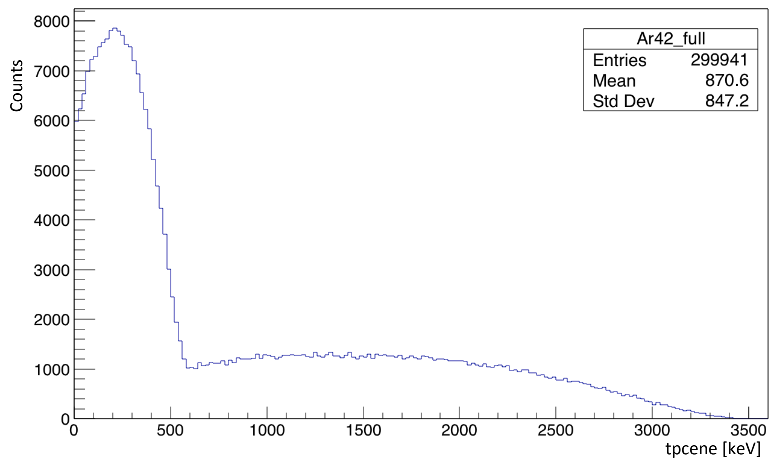

(a)

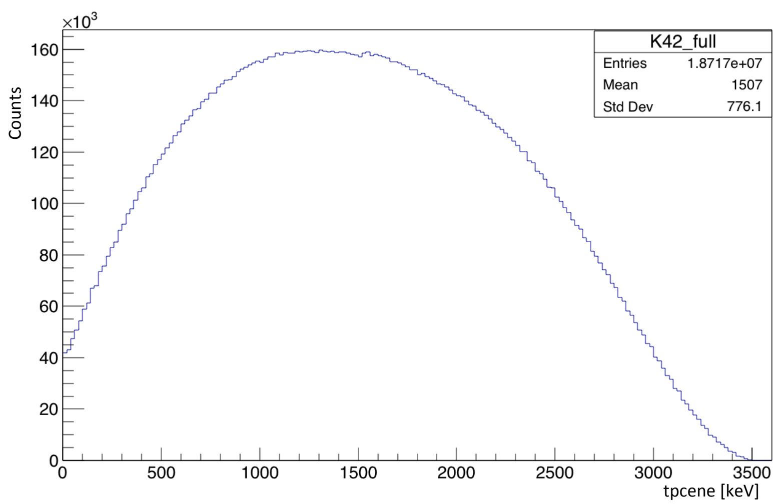

(b)

Figure 4.6: The simulated TPC energy distribution for decays from ^{42}Ar and ^{42}K full decay chains.

^{39}Ar, ^{85}Kr, ^{238}U cryostat, ^{40}K, ^{235}U cryostat at the values reported in Figure 3.1. As determined from the activities estimated by the fitter based on S1 and S1$_{late}$, the activities of those components were fixed to vary within a small interval. The small interval defined for each of those components approximately incorporates the activity values as obtained from the screening and fitting measurements reported in Figure 3.1. The "free" components that vanish were removed to constrain the fitter.

All fits for ^{42}Ar and ^{42}K in underground data set were undertaken in following fit configuration:

1) S1 range (400 PE, 5000 PE)

2) S1$_{late}$ range (400 PE, 20000 PE)

3) tdrift range (40 μs, 336 μs)

The field-on data for S1 vs tdrift fit has a livetime of 432 days after data quality cuts. While the null-field S1$_{late}$ data has livetime of $\sim$ 4 days. Due to small S1$_{late}$ data statistics above 18000 PE in data- set, the histogram bins beyond 18000 PE are combined.

The multi-dimensional fit of combined MC spectra of the background components for the field-off S1$_{late}$ and field-on S1 and tdrift data is shown in the Figure 4.7. Incorporating the spectra from full ^{42}Ar decay chain, the fitter gives an estimate for ^{42}Ar activity of 0.00186 ± 0.00035 Bq. The spectra for full decay chain of ^{42}Ar also includes ^{42}K decays. The activity estimate is based on assuming that secular equilibrium is established between ^{42}Ar β-decays and ^{42}K decays. Figure 4.7 shows the fit reproduces the activities of the "free" components reasonably well, and gives a correct order of estimate for ^{42}Ar activity. The χ^2-fits are reasonably good. With the liquid argon mass of 46.7 kg, the specific activity for ^{42}Ar is estimated to be 39.8 ± 7.5 μBq/kg in underground argon. The fitter gives the correct order of estimate for ^{42}Ar activity.

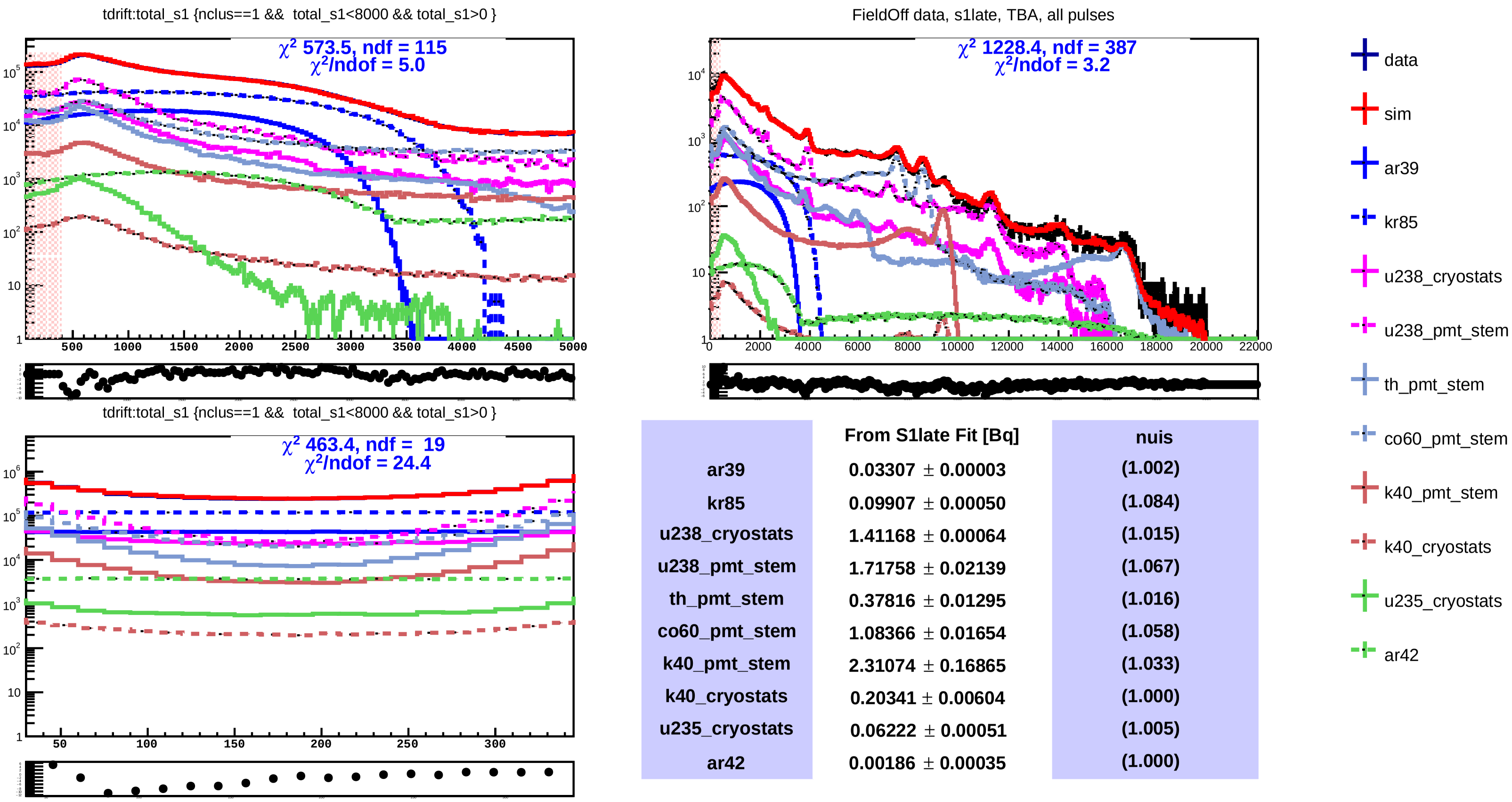

	From S1late Fit [Bq]	nuis
ar39	0.03307 ± 0.00003	(1.002)
kr85	0.09907 ± 0.00050	(1.084)
u238_cryostats	1.41168 ± 0.00064	(1.015)
u238_pmt_stem	1.71758 ± 0.02139	(1.067)
th_pmt_stem	0.37816 ± 0.01295	(1.016)
co60_pmt_stem	1.08366 ± 0.01654	(1.058)
k40_pmt_stem	2.31074 ± 0.16865	(1.033)
k40_cryostats	0.20341 ± 0.00604	(1.000)
u235_cryostats	0.06222 ± 0.00051	(1.005)
ar42	0.00186 ± 0.00035	(1.000)

Figure 4.7: The multidimensional fitting of MC S1, S1$_{late}$ and tdrift spectra on UAr data, with ^{42}Ar spectra included. The specific activity for ^{42}Ar is estimated to be ~ 40 μBq/kg.

With same fitting configuration (binning, fit ranges, and components), spectra from ^{42}K decay chain and ^{42}K β (Q = 3525 keV) were separately incorporated into the fitter. The activity estimate based on those fits is larger. When spectra from full decay chain of ^{42}K is included, the estimated specific activity is $\sim$ 100 μBq/kg. However, on incorporating ^{42}K β spectra into the fitter, the specific activity is estimated to be $\sim$ 75 μBq/kg. These values are consistent considering the natural branching ratio of 82 % for ^{42}K β (Q = 3525 keV) decay.

Statistical uncertainties owing to the different statistics of the MC data for the background components are already incorporated into the χ^2 calculation. The tuning of G4DS parameters for reconstructed S1 and S1$_{late}$ is nearly optimal with small deviation. Systematic tests were carried out by varying fit configuration. The activity estimates were checked against changes in the histogram binning, fitting range, and inclusion of other background components. The statistical uncertainties in the computed activities are small and the systematic uncertainties dominate. The activity estimate for ^{42}Ar was found most sensitive to the change in tdrift ranges without significant differences observed in the computed Chi-squares (χ^2's). Significantly smaller activity for ^{42}Ar was estimated when the fitting was carried out in tdrift range defining the region closer to the bottom of TPC.

Another fitting study was carried out to find out whether there is any preferential isotopic distribution for $^{42}Ar/^{42}K$. This can't be studied by incorporating the spectra from the entire ^{42}Ar decay chain in the fitter. S1, S1$_{late}$ and tdrift spectra for ^{42}Ar were generated assuming ^{42}Ar isotope is uniformly distributed. This assumption is probably true for the parent isotope ^{42}Ar but may not be true for its daughter ^{42}K.

One can make use of the tdrift distribution of the events to estimate the spatial distribution of a the isotope/component which undergoes decay in the TPC. The simulated ^{42}K decay chain at tdrift ranges $<$ 100 μs (component called ^{42}Ktop) and $>$ 250 μs (component

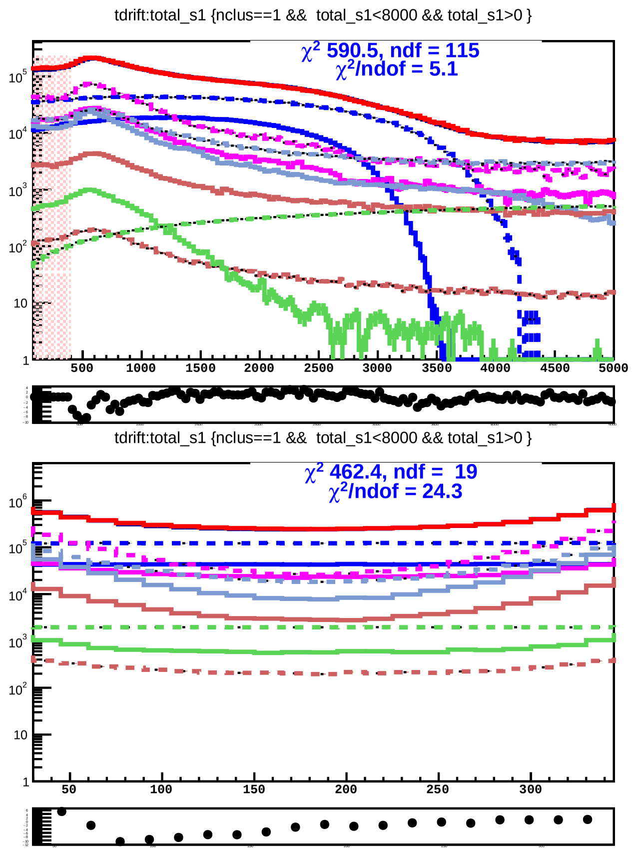

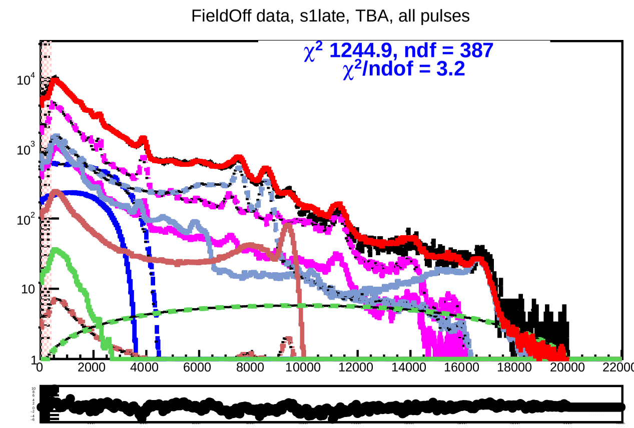

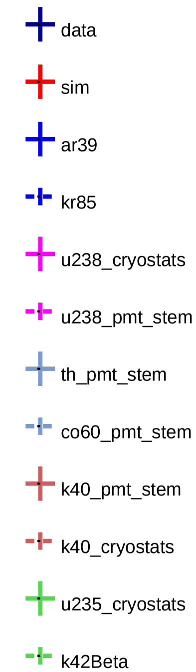

	From S1late Fit [Bq]	nuis
ar39	0.03306 ± 0.00009	(1.002)
kr85	0.10162 ± 0.00023	(1.083)
u238_cryostats	1.40404 ± 0.00066	(1.010)
u238_pmt_stem	1.72159 ± 0.02088	(1.048)
th_pmt_stem	0.40393 ± 0.01256	(1.015)
co60_pmt_stem	1.04953 ± 0.01968	(1.129)
k40_pmt_stem	2.15093 ± 0.16448	(1.046)
k40_cryostats	0.20344 ± 0.00605	(1.001)
u235_cryostats	0.06220 ± 0.00056	(1.005)
k42Beta	0.00352 ± 0.00032	(0.999)

Figure 4.8: The multidimensional fitting of MC S1, S1$_{late}$ and tdrift spectra on underground argon data, with ^{42}K β included. The specific activity for ^{42}K β activity for ^{42}K decay channel with BR=82% is estimated to be ~ 75 μBq/kg.

called ^{42}Kbot) and their respective S1, S1$_{late}$, tdrift spectra were generated and incorporated into the fitter. These would be approximate spectra if the ^{42}K isotopes were to drift in the electric field to the top (or bottom) of TPC and decay. The activity estimates and the χ^2s obtained for various ^{42}K and ^{42}Ar components are tabulated below. The results from the table show the activity estimate for ^{42}Ktop tends to 0 μBq/kg, while ^{42}Kbot tends to 10 μBq/kg. Our multidimensional fitter prefers a small excess of the ^{42}K gain positive charge ^{42}K and move to the bottom of the TPC under the influence of the electric field. The plot showing the multidimensional fit of ^{42}Kbot with other components is shown in Figure 4.9.

Table 4.1: Activity estimates and corresponding Chi-squares (χ's) for various combination of ^{42}K distribution in DarkSide-50 TPC

Components	Specific activity	χ^2/ndf (S1 fit)	χ^2/ndf (S1$_{late}$ fit)	χ^2/ndf (tdrift fit)
^{42}Ar	40 μBq/kg	5.0	3.2	24.4
^{42}Ktop	0 μBq/kg	5.3	3.1	23.5
^{42}Kbot	9 μBq/kg	5.2	3.1	22.8
^{42}Ktop,^{42}Kbot	(2,10) μBq/kg	5.2	3.1	22.9
^{42}Aruni,^{42}Kbot	(39,7) μBq/kg	5.0	3.2	23.9

4.5 $^{42}Ar/^{42}K$ fitting Studies in Atmospheric Argon (AAr) Data

The AAr and UAr data-sets have some differences. When the data-acquisition was carried out with AAr in TPC, the β-decays from ^{39}Ar dominated the trigger rate. Therefore, ^{39}Ar decays dominate the statistics in AAr data-set. On applying nominal data quality cuts and tdrift cut (> 20 μs), only six days worth of field-on data can be used for the fitting studies. tdrift cut is necessary to remove the events close to the top of the TPC that have unresolved S1 + S2 pulses that populate in the S1 time window. The multidimensional fitting in

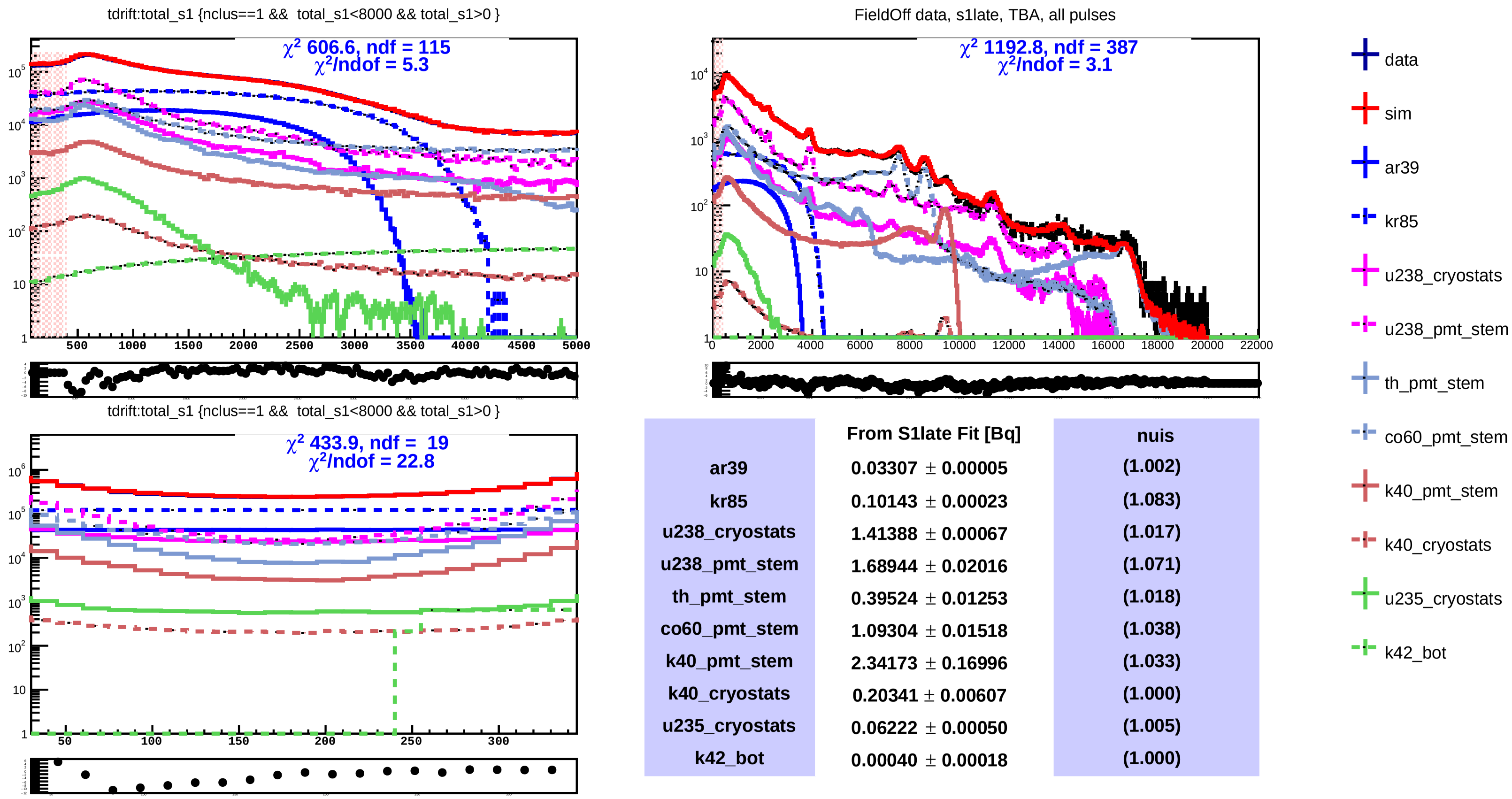

	From S1late Fit [Bq]	nuis
ar39	0.03307 ± 0.00005	(1.002)
kr85	0.10143 ± 0.00023	(1.083)
u238_cryostats	1.41388 ± 0.00067	(1.017)
u238_pmt_stem	1.68944 ± 0.02016	(1.071)
th_pmt_stem	0.39524 ± 0.01253	(1.018)
co60_pmt_stem	1.09304 ± 0.01518	(1.038)
k40_pmt_stem	2.34173 ± 0.16996	(1.033)
k40_cryostats	0.20341 ± 0.00607	(1.000)
u235_cryostats	0.06222 ± 0.00050	(1.005)
k42_bot	0.00040 ± 0.00018	(1.000)

Figure 4.9: A multidimensional spectral fit with ^{42}Kbot spectra included. The S1, S1$_{late}$ and tdrift spectra were obtained by simulating ^{42}K decays closer to the bottom of DarkSide-50 TPC.

AAr data shows insensitivity to certain background components. Moreover, there is a large "'nuisance" parameter (strong disagreement) between the activity estimates from S1 and S1$_{late}$ fits for some components. The fitter gives a reasonable estimate for the activities for some major background components when the activities of the background components are left as free parameters. However, the fitter is insensitive to some components (including ^{42}Ar) and gives a null estimate for their activities. Instead, the S1$_{late}$ spectral fitting gives a reasonable estimate for ^{42}K activity. In the best fit configuration (shown in Figure 4.10), the specific activity of ^{42}K is $\sim$ 50 μBq/kg. The fit gives a reasonable estimate for ^{42}K activity consistent with DEAP's measurements [150].

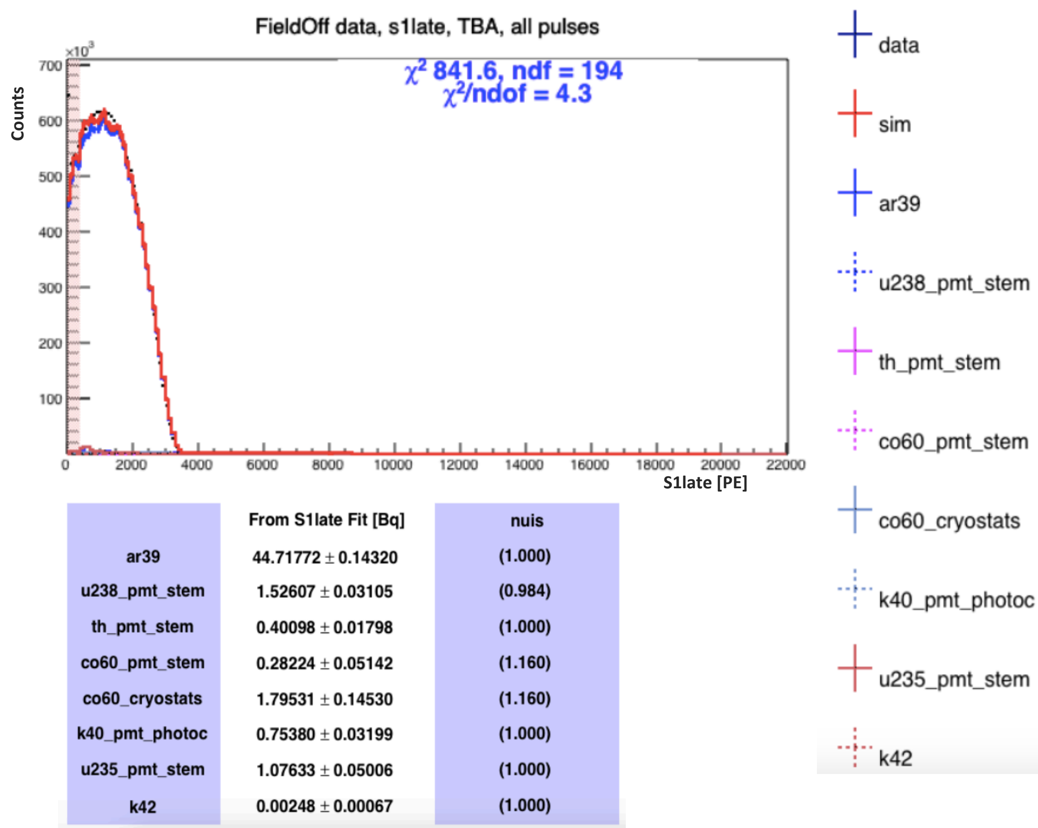

	From S1late Fit [Bq]	nuis
ar39	44.71772 ± 0.14320	(1.000)
u238_pmt_stem	1.52607 ± 0.03105	(0.984)
th_pmt_stem	0.40098 ± 0.01798	(1.000)
co60_pmt_stem	0.28224 ± 0.05142	(1.160)
co60_cryostats	1.79531 ± 0.14530	(1.160)
k40_pmt_photoc	0.75380 ± 0.03199	(1.000)
u235_pmt_stem	1.07633 ± 0.05006	(1.000)
k42	0.00248 ± 0.00067	(1.000)

Figure 4.10: The S1$_{late}$ spectral fit on AAr data with ^{42}K decay chain incorporated.

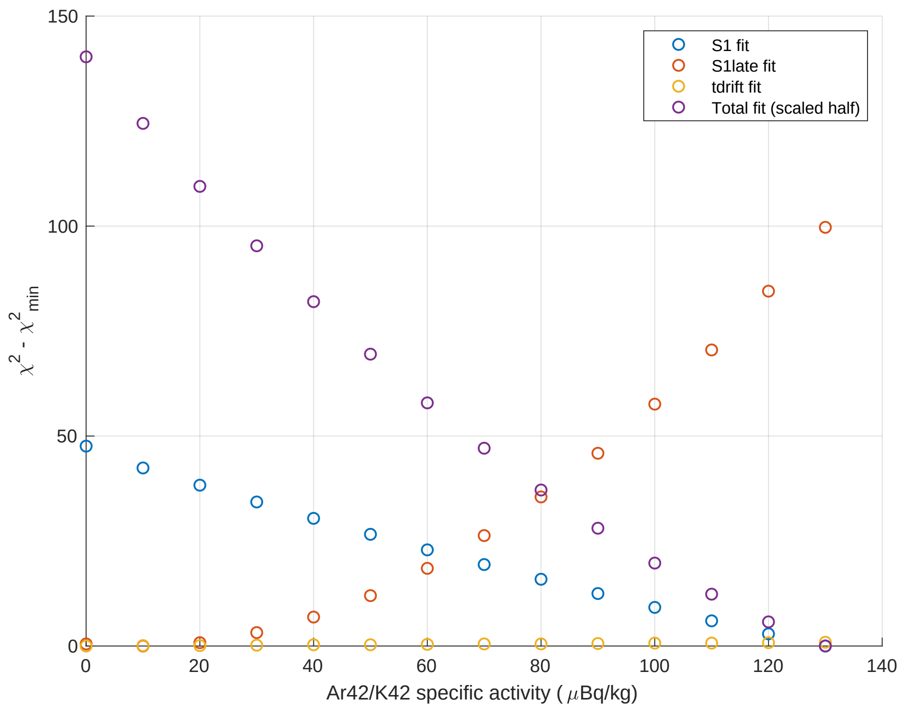

Figure 4.11: The change in χ^2's as a function of the increase in the specific activity of $^{42}Ar/^{42}K$. The spectra of ^{42}Ar β and that of ^{42}K is separately incorporated in the fitter. With increased activity, χ^2 in S1$_{late}$ rises quickly. The tdrift fit is insensitive to increased activity in the shown activity range. The fit was undertaken in AAr data.

A fitting strategy was adopted to incorporate spectra of ^{42}Ar Beta and ^{42}K full decay chain into the fitter. First, the spectra were generated assuming their isotropic distribution in TPC. Then, both components were incorporated into the fitter. The activities of ^{42}Ar β decay and ^{42}K full decay chain was fixed at the same value and incremented in successive steps. The corresponding Chi-squares (χ^2's) are recorded for each fit. The fits were performed in AAr data with the same binning, ranges, and components as used in ^{42}K S1$_{late}$ spectral fitting.

The plot of the change in χ^2's as a function of the increase in the specific activity (in steps of $\sim$ 10 μBq/kg) is shown in Figure 4.11. The change in S1$_{late}$ χ^2 is rapid above $\sim$ 60 μBq/kg. Also, above $>$ 80 μBq/kg, it is found that there is a strong systematic tension between S1$_{late}$ and S1 fits. The activities estimates from S1$_{late}$ and S1 fits differ significantly. Above 120 μBq/kg, the activity estimates for ^{42}Ar and ^{42}K differ significantly. And the activities (effectively the weighted shape of the spectra) of those components can't be simultaneously fixed. In conclusion, the fitter prefers $^{42}Ar/^{42}K$ activity on the order of few tens of μBq/kg.

4.6 Upper Limit on $^{42}Ar/^{42}K$ Activity from ^{42}K β-γ Analysis on AAr Data

The major ^{42}K decay channels are shown in Figure 4.1. ^{42}K β-decays to a ^{42}Ca (2^+) with a branching ratio (BR) of 17.7 %. ^{42}Ca (2^+) has a half-life of 0.82 picoseconds. It emits a 1524 keV γ and gets to the ground state. The ^{42}K β-γ decays were simulated in DarkSide-50 G4DS uniformly throughout the TPC. Each simulated event consists of a β and a γ produced with an exponentially distributed time delay with respect to the β. The energy of the β is drawn from the distribution (shown in Figure 4.2) with endpoint energy 2001 keV.

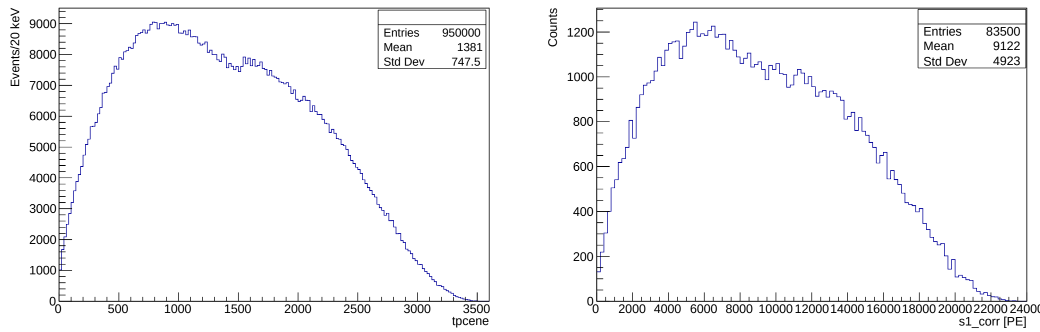

(a) (b)

Figure 4.12: a) The TPC energy distribution by simulated ^{42}K β-γ events in DarkSide-50). b) S1$_{corr}$ (z-corrected S1 distribution) of ^{42}K β-γ events simulated with S1 optics on.

The TPC energy distribution of the events is given in Figure 4.12 a). And simulated S1$_{corr}$ spectra (with smaller event statistics) is given in Figure 4.12 b) Since the β and γ emission is in almost a prompt coincidence, the event has single S1. The 1524 keV peak is not observed in the simulated spectra. The peak is smeared by the energy deposition from the β's. Further, most of the γ's do not deposit full energy in the TPC. Approximately 39 % of the events (primarily γ's) also penetrate the cryostat and deposit some energy in LSV. The LSV energy distribution shows a γ Compton peak at roughly 1400 keV.

Backgrounds

The search for signals from ^{42}K β-γ decays is not easy considering the overwhelming presence of the backgrounds. The specific activity of $^{42}Ar/^{42}K$ is expected to be on the order of few tens of μBq/kg. The ^{42}K β-γ decay channel has a BR = 17.7 %. The expected number of signal events from these decays in the 50 day AAr data-set is small. ^{42}K β-γ events induce electronic recoils (ER) in LAr. Overall, ER backgrounds (from β and γ decays) dominate the event statistics. This makes identifying the ^{42}K β-γ signals based on the available reconstructed data variables a difficult task.

Cuts implemented and effects

The basic search strategy is to identify signal events with little or no background. The parameter cuts implemented and the effects of those cuts are discussed below. The basic motivation for some cuts are to look at two pulse (S1 and S2) or three pulse (S1, and two S2's) events that deposit S1 in the range S1 (4000 to 24500) PE. In that S1 range, single-scatter (two pulses) β-events are few. Further, for single-scatter (two pulses) or double-scatter(three pulses) γ events are less likely to deposit such a large energy (scintillation). This removes majority of high energy γ backgrounds. To remove other γ backgrounds that would deposit energy in high S1 range, tdrift cuts and veto cuts are implemented. The cuts and efficiencies were tuned by looking simultaneously at simulated ^{42}K β-γ decays and at real data.

1) **Number of channels**

Cut: Select events for which information from all 38 PMTs are found. This cut is necessary because without information from all the 38 PMTs, the reconstructed variables are not reliable.

Effect: Loss of livetime

2) **Baseline**

Cut: Select events for which baseline is found. If the baseline is not present, the analysis parameters such as pulse integrals cannot be reliably reconstructed.

Effect: None

Any ^{42}K β-γ event in a live window efficiently triggers the Data Acquisition system.

3) **Veto cut**

Cut: Select events for which no energy is deposited in LSV. This removes most of the γ backgrounds from ^{60}Co, ^{40}K (from PMTs and cryostat) events, and neutron-scattering events in LSV.

Effect: Loss of signal efficiency

The cut causes large efficiency loss as some 1524 keV γ deposit energy in the LSV.

4) **Number of pulses**

Cut: Select a two pulse event or three pulse-event (Take four pulse event if S1 echo pulse or S2 echo pulse). This cut picks events with one S1 and one S2, or with one S1 and two S2's. The topology of two or three pulse events is expanded to include four pulse events as well if one of the pulse is S2 echo (echo pulse of electrons (produced by S2 photons ejecting the electrons from the cathode window) or S1 echo (echo pulse of electrons produced by S1).

Effect: Loss of signal efficiency

With affordable loss of efficiency, the cut removes multiple scattering γ's that would deposit S1 > 5000 PE. This cut combined with S1 and tdrift cuts remove most of the ^{60}Co and ^{40}K γ backgrounds.

5) **Drift time**

Cut: Select events with $40 < \text{tdrift} < 340$ μs

Effect: Loss of fiducial mass

This cut removes some γ backgrounds from the PMTs.

6) **Radial cut**

Cut: Select events with r < 17 cm

Effect: Loss of fiducial mass

This cut removes some γ backgrounds from cryostat surrounding the TPC.

Effect: Loss of fiducial mass

7) **F90**

Cut: Select events with f90 > 0.1

This cut removes few pile-up events and unresolved S1 + S2 events that pass the 40 < tdrift cut.

Effect: No effect

The ^{42}K β-γ events have f90 $\sim$ 0.3. But if the decay happened close to the top of the TPC, the f90 parameter could be < 0.1. This cut introduces the largest systematic uncertainty in the activity estimate.

Cut: Select events with f90 < 0.5

This cut removes a few α-like events that survived fiducial cuts (tdrift and radial cuts).

Effect: No effect

8) **S1 range**

Cut: Select events with $\text{S1}_{corr} > 4450$ PE

This cut removes most of the β backgrounds from ^{39}Ar and ^{39}Ar. The β events are mostly single-scatter events (with 2 pulses). Applying this cut and taking in two-pulse events removes most of the β-backgrounds at the expense of some loss of signal efficiency.

Effect: loss of signal efficiency

Cut: Select events with $\text{S1}_{corr} < 24500$ PE

Effect: Loss of signal efficiency

The signal efficiency loss from this high S1_{corr} threshold cut is $\sim < 0.1$ %. Very few β-γ signal events that contribute to the "tail-end" of the spectra (in Figure 4.12) are lost.

Activity estimate

The class of events that could pass the above cuts was studied. The possible backgrounds that could contribute are:

1) coincident ^{42}Co γ (1.17 MeV, 1.33 MeV) events

2) events from the tail of ^{85}Kr energy spectrum

3) events from ^{222}Rn (radon) daughters. These include β-decays from ^{214}Bi (with endpoint energies of 1.51 MeV, 1.54 MeV, 3.27 MeV), and β-decays (with endpoint energy 1.16 MeV) from ^{210}Bi. These radon daughters originating from the decay chains of Uranium isotopes

(present in PMTs and cryostat), are very less likely to deposit the bulk of their energies in sensitive volume. But if the radon diffuses into the liquid argon volume, the β's from the ^{222}Rn daughters can deposit energy within the TPC. These isotopes ^{214}Bi, ^{210}Bi have short half-lives on the order of few minutes.

For this analysis, AAr-50 data subsets AArp2, AArp3, AArp4, AArp5 were used. The other two data subsets approximately two days of lifetime (from early runs) were not used. Implementing above cuts, only 257 events survive. The resultant livetime is 43.28 days (after livetime losses from the implemented cuts are accounted). Including the signal efficiency loss due to some of the cuts as explained above, the MC predicts a global signal efficiency of 14.85 %. The effective mass (after the fiducial cut) is 35.4 kg.

Assuming all 257 events are from ^{42}K β-γ decays, the upper limit for the specific activity can be set. With a Global signal efficiency = 14.85 % and Effective mass = 35.4 kg, total specific activity for ^{42}K β-γ decays is found to be approximately $\sim$ 13 μ Bq/kg. Since the decay channel has a branching ratio of 17.7 %, one can estimate an upper limit for specific activity for ^{42}Ar (^{42}K). The upper limit for ^{42}Ar (^{42}K) specific activity from ^{42}K β-γ search is found to be 74 μBq/kg.

Some systematic uncertainties may arise from the MC estimate of the efficiency loss especially from the "number of pulses" cut, and the effect of the f90 > 0.1 cut. The following systematic test was carried out. Keeping all the other cuts unchanged and then varying S1 lower threshold in the range (4450 PE, 5150 PE), two values are recorded: 1) number of data events surviving the cuts, and 2) MC-predicted global detection efficiency. These can be used to predict the ^{42}Ar (^{42}K) activity in each case. Accounting for the differences, the upper limit for ^{42}Ar (^{42}K) activity is set to (70 $\pm$ 4) μBq/kg in AAr. It is important to note that the MC was generated simulating ^{42}K isotopes uniformly in the TPC.

Chapter 5

FLUKA studies for DarkSide detectors

5.1 Introduction

DarkSide-20k detector will run at the underground facilities at LNGS, like its predecessor DarkSide-50. At a depth equivalent to 3800 m of water, helped by the mountain overburden, the cosmic-ray muon flux at the LNGS cavern is reduced by a factor of 10^6 compared to that at earth's surface. Typically high energy muons penetrate to that depth, but low energy muons are removed from the spectrum attenuated by the mountain overburden. The mean energy of a cosmic ray muon at LNGS is around 280 GeV (compared to 1 GeV at the surface) [112]. The high energy muons do not directly present a serious background to dark matter (DM) searches. These muons deposit large amount of energy far above the energy range of interest for DM searches. However, these muons can interact locally (with the detector, cavern walls) and produce secondary particles. The Neutrons resulting from such muon interactions can be a serious background. These "cosmogenic" neutrons have typically higher energies than "radiogenic" neutrons and can penetrate the detector system and deposit energy in the TPC sensitive volume. So, it is important to study the muon-induced backgrounds, particularly the cosmogenic neutron backgrounds, in dark matter search experiments.

5.2 Cosmogenic Neutron Production

Negative muon (μ^-)capture: The μ^- capture occurs in nuclei via the electro-weak charged interaction (such as $\mu^- + p \rightarrow n + \nu$), and produces neutrons. This reaction can take place if muon kinetic energy is comparable or smaller than the muon binding energies. The capture rate is competitive to the muon decay ($\mu \rightarrow e^- + \nu + \nu$) rate in heavier nuclei [152]. This mode of neutron production is dominant at depths smaller than 100 meter water equivalent (m.w.e).

Muon spallation on nuclei: This process involves interaction of muon with a nuclei via exchange of a virtual photon. It causes the nucleus to disintegrate and emit secondary particles (including neutrons). This mode of neutron production exists at all depths. Shielding has little effect, as the muon can spallate on the shielding materials as well. Spallation of muons or/and its secondaries on the nuclei can also release neutrons.

Photo-nuclear interactions induced by muon : These interactions can produce neutrons via predominantly (γ, n) reactions. Typically, less than 10 MeV γ's are more likely to undergo Compton scattering with atomic electrons. γ's of (10-30)MeV mostly originate in electromagnetic showers induced by muon interactions. They can produce neutrons by a process called nuclear giant resonance (high-frequency collective dipole excitation of a nucleus) [153]. Neutrons produced by this mechanism have energies in the range 1 to 10 MeV. Above 30 MeV up to the pion threshold (140 MeV) [154], photo-nuclear interactions can produce neutrons by a quasi-deuteron effect. The photon interacts with the dipole moment of the proton-neutron pair instead of the nucleus as a whole. The energy of the neutrons produced by such interaction can have energies up to several hundred MeVs. Above 140 MeV (pion mass), photo-nuclear interactions can produce pions as well as neutrons. Neutrons can also be produced by pion capture in nuclei via $\pi^- + (Z, A) \rightarrow (Z-1, A-1) + n$. At even higher energies, large scale photo-hadron productions can occur. A large mix of pions, mesons, and kaons are produced. And highly energetic neutrons (with energy on the order of GeV) can be produced by the interaction of the photo-produced hadrons with the nuclei.

Hadronic showers induced by muon spallation: A high energy muon spallation on nuclei can result in hadronic showers. A hadronic shower consists of pions, kaons and nucleons, etc. Hadrons can interact with nuclei, or with themselves producing a sub-cascade of hadrons and nucleons. The hadrons lose energy and decay to other hadrons and/or leptons. Charged interactions or decay of particularly neutral mesons can also produce electromagnetic showers (of γ, e^+e^-, ν). Neutrons produced in hadronic showers can have energies from 10 GeV to 100 GeVs. These high energy neutrons contribute to the tail-end of the neutron energy spectrum shown in Figure 5.1.

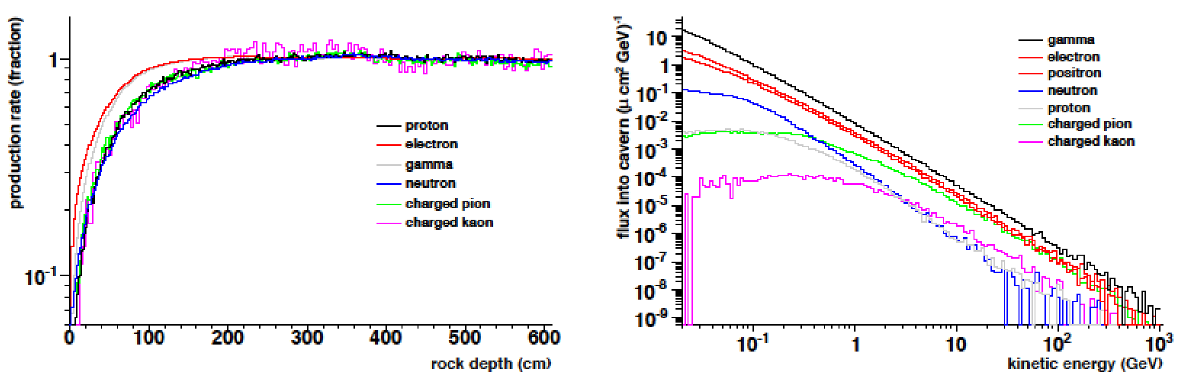

Figure 5.1: Particle production rates by 280 GeV muons traversing Gran Sasso rock as a function of distance (Left), the production rates are normalised for the particle species to the maximum production rate. The FLUKA- based prediction of integral particle flux per cosmogenic muon at Hall C of LNGS as a function of kinetic energy (Right). Figure taken directly from [16].

Cosmogenic neutron production, induced by fast muons on a material, can be expressed in terms of muon-induced neutron yield. It is defined as the number of neutrons produced per muon per gcm^{-2}. With the assumption muon energy losses are proportional to the muon energy, all nuclear reactions including those leading to neutron production is predicted to vary as $\overline{E}_{\mu}^{0.7}(x)$[155], where $\overline{E}_{\mu}(x)$ is the mean energy of muon at depth/thickness x. Precise measurement of neutron yield is a difficult endeavor. Underground experiments usually measure thermal neutrons that capture on the detectors. The Borexino's measurements and the FLUKA-based prediction of cosmogenic neutron production and yield are reported in [16].

5.3 FLUKA Simulation Toolkit

FLUKA is a particle interaction and transport Monte Carlo tool now independently managed by INFN and CERN [156] [157] [158]. FLUKA has been used in a wide range of applications: cosmic ray physics, neutrino physics, accelerator design and shielding, dosimetry, hadron therapy, neutronics, etc. FLUKA incorporates and implements sound and modern physical models. When applicable, microscopic physics models are implemented and ensured there is consistency among all the reaction steps and/or reaction types, conservation laws are fulfilled a priori, and results are validated with experimental data at each interaction level. Final predictions are obtained with minimal free parameters fixed for all energies, targets, and projectiles.

FLUKA has been known to simulate with high accuracy the interaction and propagation in matter of about 60 different particles, including photons, electrons, muons, hadrons, and neutrinos from eV to the PeV scale. It can also be used to track charged particles in the presence of electric and magnetic fields. Using an improved version of the Combinatorial Geometry (CG) package, FLUKA allows users to implement very complex geometries. The most important file for FLUKA is a text file with extension, .inp, that acts as an input file to incorporate material, geometry, and physics models by calling an appropriate card within the input file. This enables users to do little or no fortran coding and carry out simulation studies. If required, FLUKA allows the users to implement or change the Fortran user routines, and build suitable executable relevant to the problem of interest.

A user interface FLAIR [159], built on the python code, exists for FLUKA. It allows users to implement materials, geometry, design, and relevant physics models, build appropriate executables, process the FLUKA outputs, and obtain graphical plots when applicable. FLAIR is a powerful visualization and debugging tool that makes FLUKA studies relatively easier for users.

5.4 Cosmogenic Background Studies at LNGS

5.4.1 Muon-flux Measurements

The LNGS underground facility consists of three halls, 1) Hall A, 2) Hall B, and 3) Hall C. Various experiments have measured the total muon flux at LNGS. The muon flux reported by various experiments at LNGS is shown in Table 5.1. The variation in the measured values can be attributed to the relative location of halls within LNGS, differences in the time of data-taking, and systematic uncertainties.

Table 5.1: Total muon flux measured by various experiments at LNGS.

Experiment	Site	Total muon flux ($\times 10^{-4} s^{-1} m^{-2}$)	References
LVD	Hall A	3.33 ± 0.03	[160]
GERDA	Hall A	3.47 ± 0.07	[151]
MACRO	Hall B	3.22 ± 0.08	[161]
Borexino	Hall C	3.41 ± 0.01	[112]

5.4.2 Muon Energy Spectrum at LNGS

The cosmic muon kinetic energy spectrum can be represented by [162]:

$$\frac{dN}{dE_\mu} = const.(E_\mu + \epsilon(1 - e^{-\beta h})^{-\alpha} \tag{5.1}$$

where, E_μ is muon kinetic energy at slant depth, h, α is the surface muon spectral index, β and ϵ are associated with the muon energy loss mechanism in rock. The solution to Equation 5.1 [162] for average muon energy underground at slant depth h yields

$$< E_\mu >= \frac{\epsilon(1 - e^{-\beta h})}{\alpha - 2} \tag{5.2}$$

For large slant depth h, $\frac{dN}{dE}$ almost becomes flat for $E < E_\mu$, and then decreases with E.

MACRO Transition Radiation Detector at LNGS measured mean energy (in GeV) of $270 \pm 3(stat) \pm 18(syst)$ and $381 \pm 13(stat) \pm 21(sys)$ for single-muon events and double-muon events respectively.

The form of the Equation 5.1 can be integrated and inverted in analytical form, hence, permitting direct sampling. With a suitable choice of values for β and ϵ, the equation can reproduce the measured spectrum for both single-muon and double-muon events.

Angular distribution

The muon intensity and the energy profile of the muons is also a function of their incident direction on the detector. Slant depth h in (in the units of g/cm^2) of throughgoing muon in the overburden rock depends on both azimuthal (ϕ) and zenith angle (θ). Azimuthal angular distribution depends on the profile of the Gran Sasso mountain overburden. Angular distribution of the muons entering LNGS have been measured by MACRO [163] and Borexino [139]. The comparison of the data with the FLUKA predicted muon angular distribution is shown in Figure 5.2. The spectra are normalized with respect to the total muon flux measured by Borexino.

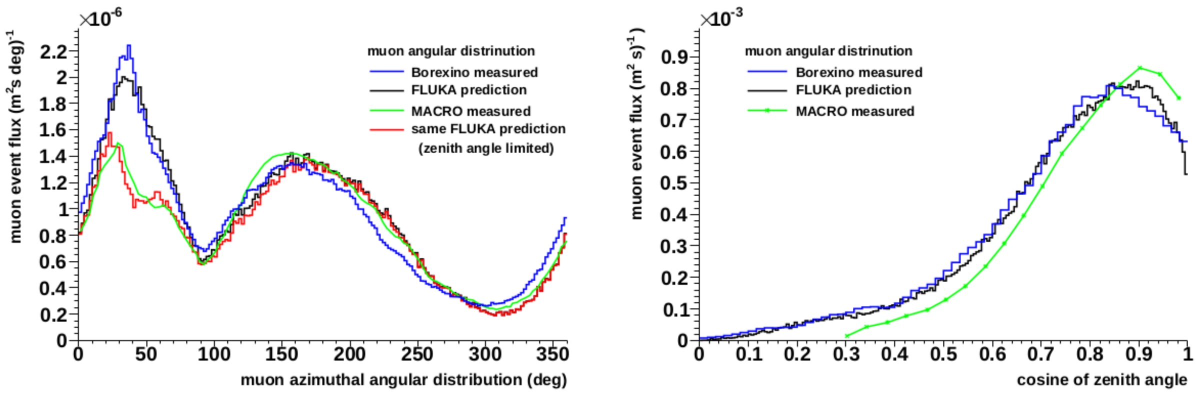

Figure 5.2: Muon azimuthal (left) and zenith (right) angular distribution at LNGS for polar coordinate system pointing up and North with clockwise increasing angle. The comparison between Borexino (blue), MACRO (green), and FLUKA predictions (black, red (zenith angle limited)). Figure taken directly from [16].

5.4.3 Muon-induced Full Radiation field at Hall C

To make reliable predictions of muon-induced background for underground detectors, the full spectra of muon and its secondaries need to be considered instead of muon spectra alone. A faithful simulation of the muon radiation field at the underground experiment also needs to implement the details of the depth, overburden geometry, and rock composition. Using FLUKA, a full simulated radiation field was prepared for Hall C (LNGS) [16]. The radiation field has been used in cosmogenic background studies for the Borexino and DarkSide detectors.

Event generation and propagation

To generate the muon flux within the hall, the combination of azimuthal and zenith angles were selected according to the measured muon angular distribution. The MACRO experiment mapped the Gran Sasso overburden [163], and based on it the muon direction can be translated into a respective slant depth h. The single muon or muon bundle event was sampled from the muon multiplicity spectrum measured by MACRO. The muon bundle with multiplicity greater than four was treated as having multiplicity four to simplify the sampling of the muon multiplicity spectrum. The distance between muons in a given bundle was drawn from the distribution measured by MACRO, and all muons within a bundle were given the same direction. The muon kinetic energy as a function of slant depth and muon event type, was selected by sampling from parameterized single or double muon event energy spectra. Unlike μ^+, μ^- can capture on nuclei. At the depth of LNGS, the fraction of stopped muon is less than 1 %. The constant charge ratio of $N_{\mu+/\mu-}$ of 1.38 was used to simplify the simulation. It is consistent with the weighted average of measurements reported by OPERA [164][$R_{single} = 1.395 \pm 0.025$ and $R_{multi} = 1.23 \pm 0.1$].

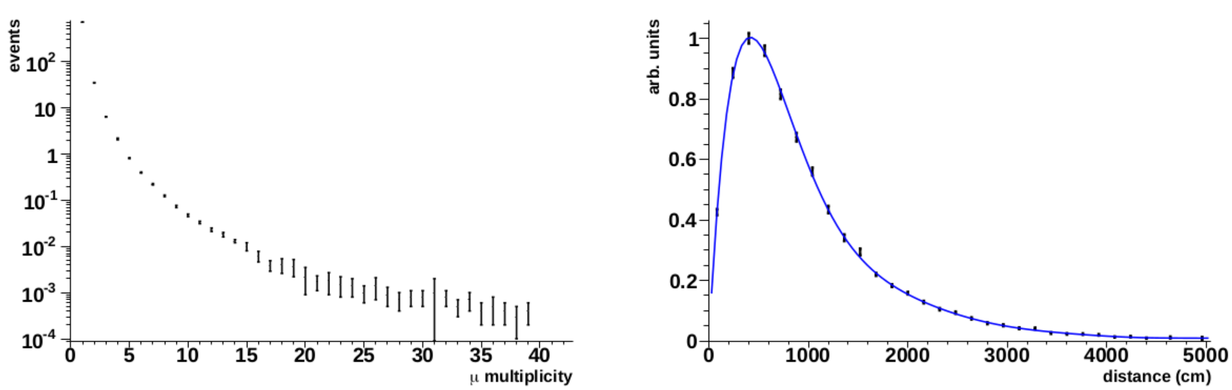

Figure 5.3: (Left) Muon multiplicity recorded by the MACRO detector. (Right) Muon separation for cosmogenic events in MACRO detector featuring two coincident muons (data points in black). The higher polynomial fit (blue) used for sampling of the distribution. Figure taken directly from [16].

Initially, a FLUKA description of the muon-induced radiation field at LNGS was prepared in the context of Borexino experiment [16][139]. The model incorporated 700 cm of rock surrounding the Hall C. The thickness was determined by the simulation to be enough to allow full shower development. The muon events were randomly chosen on a plane large enough to illuminate Hall C. The idea was to implement the initial distribution of muons at every point within the rock with appropriate direction and energy. Initially, the muon events were allowed to propagate without interactions and recorded only if they entered the hall. High energy muons propagating through the rock deviate little from their trajectories, so these muons were chosen as the sample for the simulation adjusting their kinetic energy by considering the average energy loss through the rock layer. Then the simulation was rerun with full physical processes enabling the muon to propagate through the rock layer and produce secondaries. The full description of the cosmogenic radiation field (that of muon and its secondaries) was recorded at the ceiling of the cavern. The full radiation field is necessary instead of simulating just the muon or cosmogenic neutron alone, as several processes can lead to neutron production when muons and the secondaries propagate through the rock and the detector materials. The recorded information of the full radiation field at the Hall-C was used in the context of Borexino as well as DarkSide detectors. Considering the small size of the cavern, the radiation field can be assumed constant at the average depth of the hall.

Validation with respect to Borexino

The full radiation field (stored as discussed above) emerging into Hall-C were propagated into the Borexino detector, and FLUKA-based predictions were validated against some Borexino's measurements [16][139]. Borexino's experimental data on cosmogenic neutrons have smaller systematic uncertainties. This is helped by the large size of the detector, simple spherical geometry, and efficient muon-tagging ability of the detector.

Muon-induced neutron yield is defined as the number of neutrons produced by a fast muon per gcm^{-2} and is predicted to increase with muon energy [165]. This is not directly accessible to the experiment. In liquid scintillators (such as in Borexino), neutron capture yield is measured based on gammas from neutron captures on isotopes like ^{1}H, ^{11}C. Fast neutron captures (order of 1 %) are not visible as they are overwhelmed by the high energy deposition of incident muon. However, Borexino has high detection efficiency for neutron captures that take place in a delayed time window (above 30 μs). The neutron capture yield predicted by FLUKA study is 2.7×10^{-4} muon gcm^{-2} [16] in agreement with the reported Borexino's experimental value. The cosmogenic isotope production by the muon interactions and the isotope yields from Borexino measurements, along with that predicted by FLUKA and Geant4 are tabulated in [139]. The FLUKA predictions are in good agreement with the experimental results.

Borexino carried out the spatial reconstruction of the (delayed) neutron capture locations and the parent muon track. This information was used to obtain the neutron lateral distance distribution. Neutron lateral distance is taken as the perpendicular distance between the neutron capture vertex/gamma emission vertex and the corresponding parent muon track. The measured neutron lateral distributions and the FLUKA predictions are shown in Figure 5.4. At large distances, there is a small deviation between the FLUKA-predicted and measured distributions. This difference can be attributed to muon bundle events in the data. In Borexino measurements, all neutrons were assigned to a single muon while some neutrons could have been produced by the coincident muons from bundles crossing the detector. This is more probable for higher neutron multiplicity as some neutrons may capture substantially away from the parent muon track.

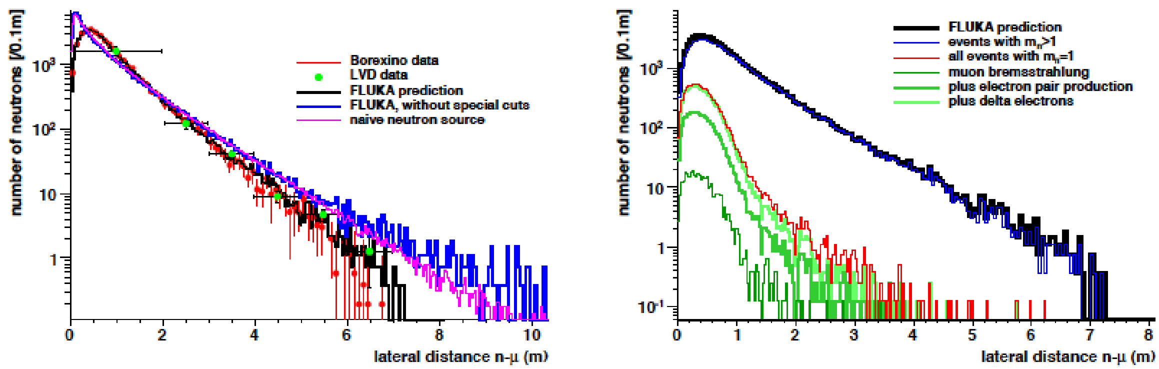

Figure 5.4: (Left) The neutron lateral distribution, FLUKA predictions compared with measurements from Borexino and LVD. blue histogram gives the predicted lateral distribution before applying reconstruction uncertainties and additional radial cuts. The predicted distribution for simple neutron simulation is in purple (left figure) and cumulative fractions of the events initiated by various class of muon interactions are shown on the right for the case. Figure taken from [16].

The FLUKA-predicted spectrum for multiplicity of thermal neutron capture per muon-induced event has been found to reproduce the Borexino's spectrum with reasonable accuracy. The "hard" losses by energetic muons are more likely initiated by muon bremsstrahlung and muon-nuclear interactions. The "soft" energy losses can be attributed to electron pair and delta electron production. A major fraction of single neutron capture is triggered by muons after delta electron pair production[16] . While high neutron multiplicity (> 5) is mostly caused by muon-nuclear interactions.

The cosmogenic muon event rate resulting in one or more thermal neutron capture in Borexino was 67 ± 1 per day. The corresponding FLUKA-predicted rate was 41 ± 3 per day [16]. The difference is limited to muon events with very low neutron capture multiplicities.

5.5 Previous FLUKA studies for DarkSide detectors

FLUKA based cosmogenic background studies have been carried out for DarkSide-50 detector in the past [7][9][14][166] as well as for different variants of the multi-ton DarkSide detectors [16][166][167] . This section particularly focuses on the FLUKA prediction and validation for DarkSide-50. The FLUKA simulation studies have been carried out to estimate the cosmogenic neutron veto efficiency and to estimate the cosmogenic neutron background for dark matter searches.

The simulated muon radiation field at Hall-C ceiling was used in cosmogenic background studies for DarkSide-50. The geometry and design of the DarkSide-50 detector was implemented in FLUKA. The radiation field was propagated onto the geometry. The simulation was run in two steps. First, the events were propagated and recorded as they entered the Water Cherenkov Detector(WCD). At this step, optics were set off. For the second step of the simulation, a certain event selection criterion was designed. Those events for which no particle entered the WCD were not pursued. The muon events leaving greater than 4 GeV in WCD and having a path length of greater than 2m were rejected. These events produce many signals in the veto detectors (WCD and the LSV) and are easily identifiable. Propagating those events with optics is computationally costly. In the second step, if the event had at least one particle entering LSV, the events were re-propagated from the WCD boundary with optics on.

For the generated simulation livetime of 48.7 years, 1388 events were found to have at least one particle entering the sensitive volume [9] and all of those could be vetoed based on energy deposition in veto detectors alone. In addition to veto information, the neutron interactions in TPC help identify a neutron signal from WIMP signal. Allowing in the muon events with long path lengths and energies in WCD, FLUKA-based studies predicted two single-scatter neutron events in WIMP search box. In 532.4-day data set, three such

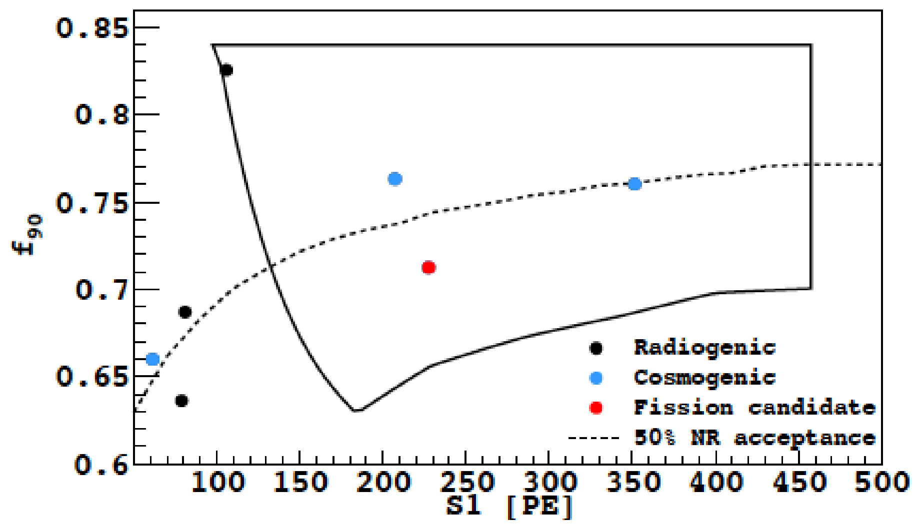

Figure 5.5: Neutron candidates in prompt Veto tag. Closed curve is the WIMP box and dashed curve is 50% Nuclear Recoil contour. Figure taken from [9].

cosmogenic neutron candidates were found (consistent with the FLUKA-predicted value). All the neutron candidates are shown in Figure 5.5. None of those candidates survive prompt veto cut. The DarkSide-50 could reject cosmogenic neutron backgrounds with very high efficiency.

5.6 FLUKA Study of Cosmogenic Backgrounds for DarkSide-20k

5.6.1 Design and Geometry

In this work, the design and geometry of DarkSide-20k was implemented in the FLUKA simulation code. The details of the design and geometry are discussed in an updated version of the technical design report [6]. The DarkSide-20k detector will have a protoDUNE-like cryostat. The details of the design of the protoDUNE cryostat are discussed in [114]. The outer cryostat geometry was implemented in the FLUKA in collaboration with the CERN group. Any updated changes in the cryostat design have been implemented.

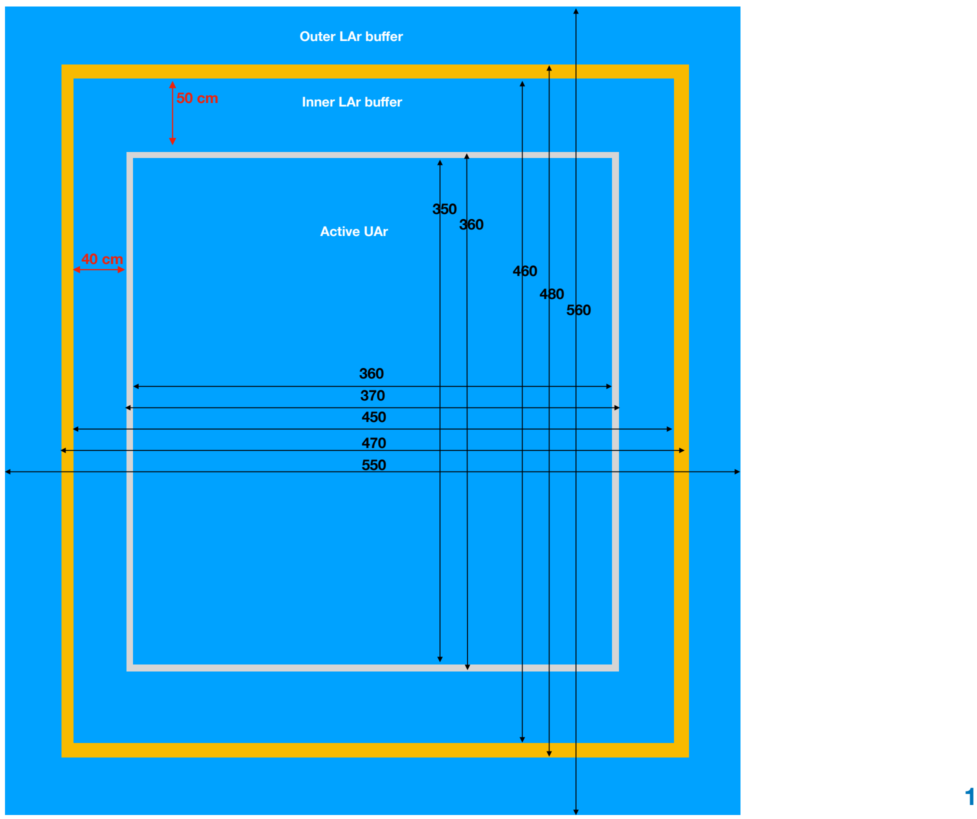

Figure 5.6: Dimensions of inner detector volumes as implemented in the FLUKA simulation. The inner vessel is approximated by nested cylindrical volumes with each volume holding approximately same amount of material as in real detector.

The inner vessel geometry implemented in FLUKA consists of five nested volumes, approximated by series of cylinders with their geometric center coinciding to that of TPC with the approximately right amount of materials. Five nested volumes (from the inside to the outside are: LAr (filling the TPC, 50 tons), acrylic TPC wall (5 cm thick in all directions surrounding the sensitive liquid argon volume), inner LAr veto (40 cm thick around the

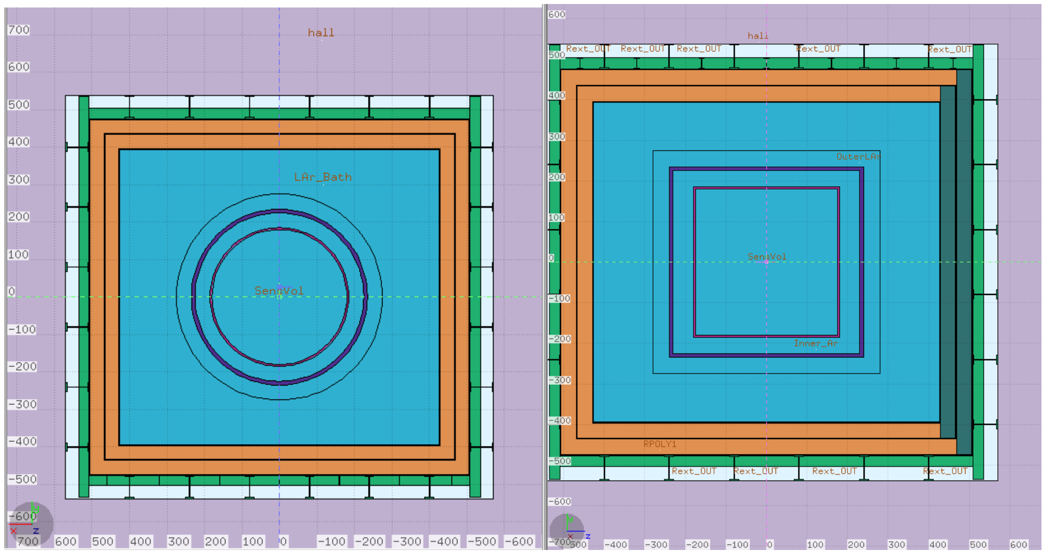

(a) (b)

Figure 5.7: The DarkSide-20k detector geometry and design implemented in the FLUKA simulation. (Left) is X-Y view. (Right) is Y-Z view.

vessel), Gd-doped acrylic (Gd at 1% mass fraction, 10 cm thick around the inner veto) and outer LAr veto (40cm around the Gd-plastic shell). The dimensions as implemented for inner volumes are given in the Figure 5.6, and the geometry of the design implemented in FLUKA is given in Figure 5.7. The polyure insulation layers on the cryostat roof have a smaller density ($\sim 40\ kg/m^3$) than in the layers surrounding from other sides.

Previously, the simulated muon radiation field prepared at the ceiling of Hall C was allowed to propagate through the air and stored on a virtual cylinder of 14m diameter and 14m. The description of the full radiation field (information of the events) on the surface of the cylinder is stored as fort.95 (Fortran binary) file. For this study, the events are pulled back by 78 cm to propagate them from just outside DarkSide-20k.

5.6.2 FLUKA: Physics Models and Related User Options

The present simulation work was carried out using the FLUKA code version 2011.2x.8 released on November 2019 by INFN. In FLUKA, photonuclear interactions are simulated over a large energy range through different mechanisms (Vector Meson Dominance, Delta Resonance, Quasi-Deuteron and Giant Dipole Resonance) depending of the projectile particle and energy [158][168]. Hadron-hadron interactions are based on the Dual Parton Model for energies (5 GeV to 20 TeV) while upto 5 GeV, the interactions are based on a Resonance production and decay model. All nuclear interaction models including nucleus-nucleus interactions share parts of the common PEANUT framework. The PEANUT nuclear interaction model in FLUKA can be described as sequence of following steps

- Glauber-Gribov multiple scattering followed by Generalized Intranuclear Cascade (GINC) at high energies (5 GeV and higher)
- Preequilibrium-cascade emission
- Evaporation/Fragmentation/Fission and De-excitation

Nuclear interactions generated by ions are treated through interfaces to external event generators. Nuclear interactions in FLUKA are treated with various nuclear models. Low energy neutrons (defined as neutrons having energies < 20 MeV) are treated separately using FLUKA neutron cross-section libraries and transported using the multi-group transport technique.

Physics models in FLUKA are integrated into the code and individual models are benchmarked against the available experimental data. The users have to call upon the relevant model/configuration that suits the problem of interest. For the simulation studies carried out in this work, the default setting was PRECISIO. It activates most of the physics processes relevant to cosmogenic muon interactions, while thresholds for the transport of the various particles can be set by the user. Low energy neutrons are transported to thermal energies. Photo-nuclear interactions were turned on in all materials using PHOTONUC, and nuclear de-excitations were called upon by using EVAPORAT and COALESCE . IONSPLIT activates the splitting of ions into nucleons. RADDECAY was enabled to simulate radioactive decays. Nucleus-nucleus interactions and transport can be activated using IONTRANS. To allow nucleus-nucleus interactions at higher energies (above 125 MeV/n), FLUKA requires linking the external event generators DPMJET and RQMD, and creating "ldpmqmd" executable [158].

5.6.3 Simulation Procedures

The FLUKA simulations were run at the Sabine cluster, University of Houston(UH). In the first step, the events were propagated in and raw energy deposition in each detector (LArBath, Outer LAr Veto, Inner LAr Veto, TPC) is collected. EVENTBIN enables a record of event-by-event energy depositions on the defined regions. In this step, full information (particle multiplicity, particle type, kinetic energy, age, position, and direction cosines) of the events were written into an external file for those events that have at least one particle entering the sensitive volume. Effectively, the radiation field is "frozen" at the surface of the TPC cylinder. In the second step, the events recorded at TPC were further propagated, demanding an event-by-event record of interaction types, number of scatterings, energy deposits, and information on the secondaries created. A conservative event selection criterion was designed to speed up the simulation and focus on important events for cosmogenic neutron background studies. After initial studies, the following events were rejected in second step:

- The events for which original muon is tracked entering the sensitive volume. None of these events pass the cut: outer veto energy deposition $<$ 100 MeV and inner veto energy deposition < 10 MeV.

- The events for which more than 50 particles are tracked entering the sensitive volume. These events leave enough coincident signals at multiple sites within the detector.

- The events for which summed kinetic energy (KE) of the particles are greater than 2 GeV at the boundary of TPC. Such events deposit significant energy in the sensitive volume, undergo a large number of scatterings, and are well-outside the most conservative WIMP search box.

5.6.4 Simulation Results

The simulation was carried out for a number of cosmogenic events corresponding to a lifetime of approximately 158 years (normalised with respect to Borexino's muon flux measurements) for DarkSide-20k. Approximately 10 million cosmogenic events at the cavern correspond to simulation lifetime of 169 days of a lifetime for our simulation geometry [16].

Table 5.2: Expected cosmogenic event rates at detector boundaries in DarkSide-20k

Expected cosmogenic event rates	
Just outside of	cosmogenic event rate
LAr Bath	2.50/min
Outer Argon Veto	0.92/min
Inner Argon Veto	0.65/min
LAr sensitive volume	0.40/min

The estimated cosmogenic event rates at boundary interface of LAr Bath, Outer LAr Veto, Inner LAr Veto and Liquid argon sensitive volume are shown in Table 5.2. These rates are upper limits as the entering particle was not required to deposit energy within the respective detectors. Each detector volume acts as a powerful passive shield. The cosmogenic event rates falls at each inner detector boundaries. Only 6.3% of original events have at least one particle entering the LAr sensitive volume. The cosmogenic rate for events that have at

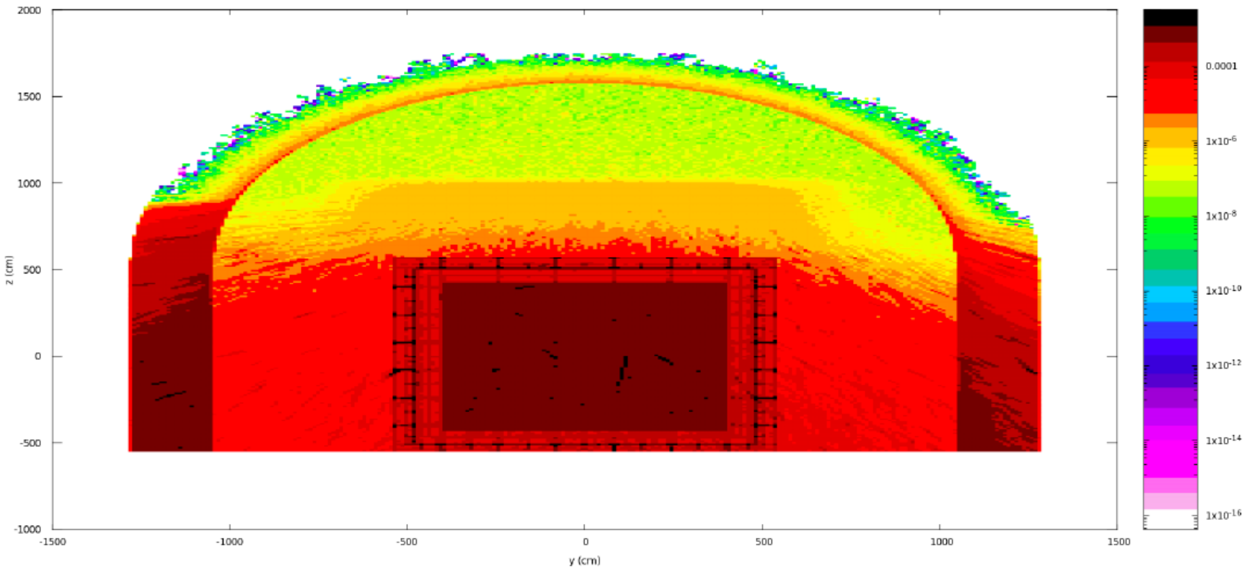

Figure 5.8: Energy deposition (per GeV per primary) by cosmogenic events [(Y-Z) view].

least one particle entering the sensitive volume is 0.40 per minute (580 per day). This event rate is high compared to the rate obtained for other version of DarkSide multiton detector, reported in [16]. The reason for it is the increased size of the sensitive volume relative to the size of veto detectors in DarkSide-20k, in comparison to the earlier version of the detector.

Tracking the events with muon entering the TPC boundary, the muon event rate is 0.31 per minute (450 per day). This event rate doesn't take into account the muon multiplicity or type, as the only requirement placed was the events have at least one muon entering the TPC.

For cosmogenic neutron background studies, only those events for which at least one particle is recorded as entering the sensitive volume were considered. The energy deposition by those events in the veto detectors is shown in the scatter plot (Figure 5.9). The energy deposition in the region of the scatter plot roughly defined by $0.2 < dE_{OAR} < 0.6$ and $0.2 < dE_{IAR} < 0.6$ (yellowish region in the scatter plot) are mostly populated by the energetic muon events. The muons that reach TPC will deposit a large energy (mostly through ionization and Bremsstrahlung) in outer detector volumes. No event is found (in simulation

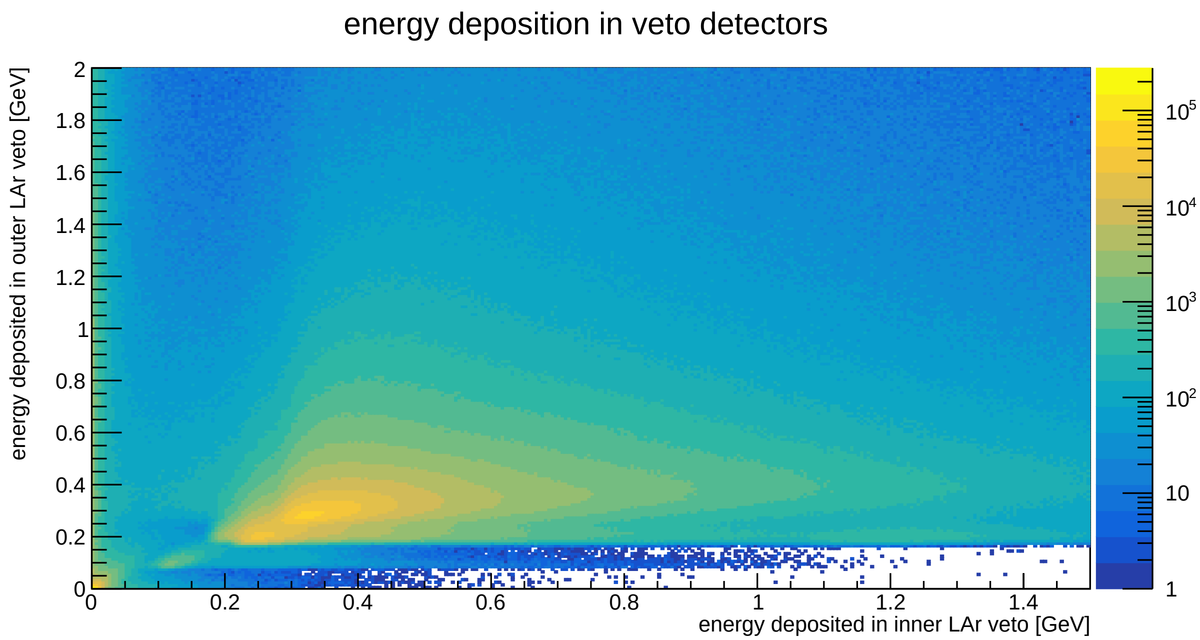

Figure 5.9: Energy deposited by cosmogenic events in veto detectors for which at least one particle is entering sensitive volume of the detector.

lifetime of 158.1 years) that has energy deposition: $dE_{OAR} < 10$ MeV and $dE_{IAR} < 100$ MeV , and has a muon entering the sensitive volume.

The events that populate close to the Y-axis and have $dE_{OAR} > 0.2\ GeV$ in the scatter plot deposit significant energy in outer LAr veto but deposit little or no energy in the inner liquid argon veto. The most difficult class of cosmogenic events to veto are those close to the origin of the graph. Such events deposit little energy in the veto detectors.

The rate of events with a neutron entering the TPC is 38 per day. Most of those events have neutrons accompanied by other particles, and most of those events deposit enough energy in veto-detectors, or/and have multiple scatterings from the coincident particles. In a simulation lifetime of 158 years, 112553 events are found with one neutron or/and one other particle entering TPC. The rate for such events is 712 per year (1.7 times larger than the earlier design discussed in [166]). And the estimated rate for a single neutron entering the TPC is 295 per year. The energy deposition spectrum of those neutron events is shown in figure 5.10. The rate of the single neutron entering the sensitive volume that passes the cut: with sum veto energy deposition < 10 MeV and energy deposition in TPC < 2 MeV (1 MeV) is 23.04 per year (19.48 per year).

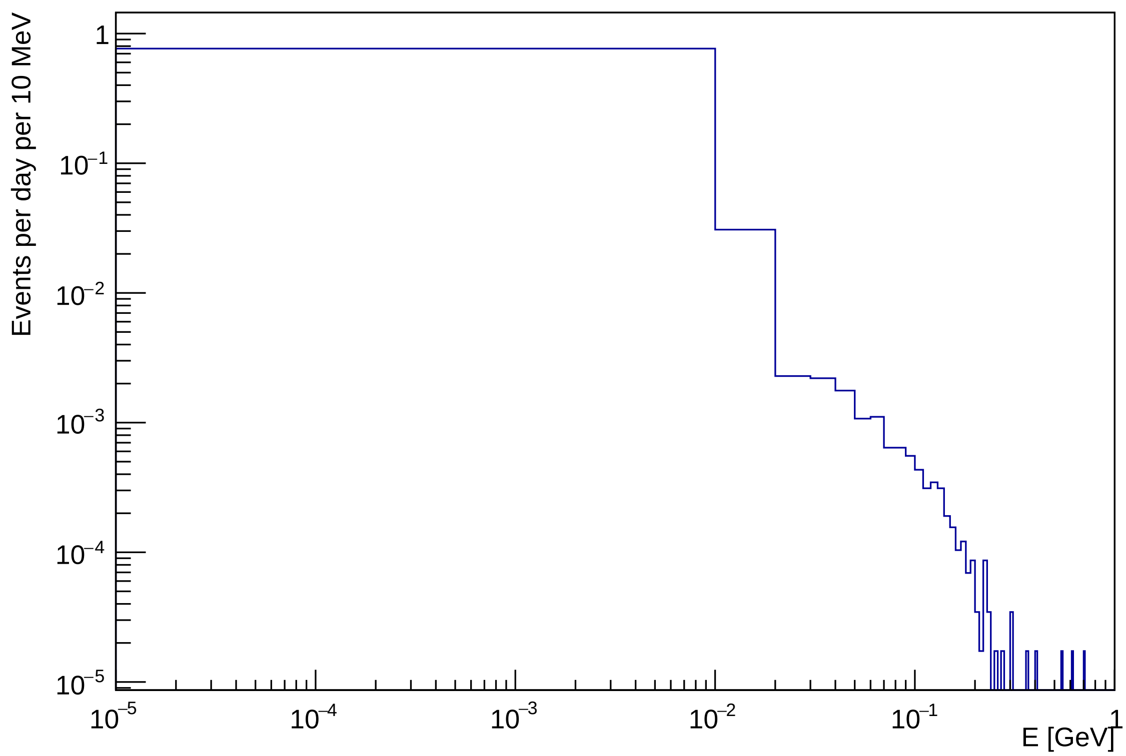

Figure 5.10: Energy deposited by event for which a single neutron is tracked entering the LAr sensitive volume. With no Veto or TPC cuts, 46745 events were found in 158.2 years (295 per year).

There are 199175 events in 158.1 years for which sum energy deposited in Outer Argon Veto and Inner Argon Veto is < 10 MeV and energy deposited in sensitive volume < 2 MeV. Practically, those events fall in one of these two classes 1) Non-muon event entering the LArBath 2) The muon-event that escaped the inner detectors. The energy deposition of those events are shown in Figure 5.11. If exploited, the energy deposition in LAr Bath can be used to veto these events that deposit little energy in inner detectors.

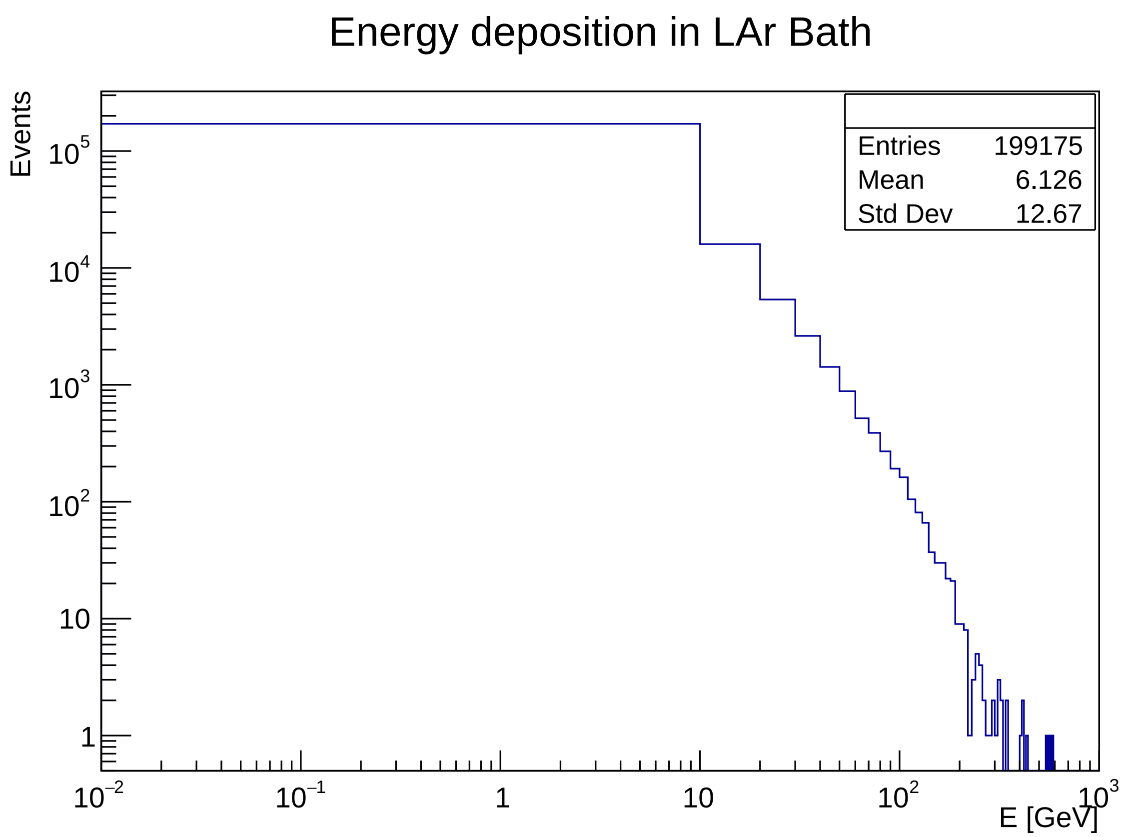

Figure 5.11: Energy deposited by cosmogenic events in LArBath for which energy deposited in veto detectors < 10 MeV and energy deposited in < 2 MeV for all 158.2 years of simulation lifetime.

Close to 97.4% of the 199175 events have only a gamma entering the TPC. Only one event (neutron produced by secondary produced by the decay of K^0) has a neutron interacting in the sensitive volume for which no neutron entered the sensitive volume. Out of all 199175 events that satisfy the veto cut (sum veto energy < 10 MeV and energy deposition in TPC < 2 MeV), only 9201 events (event rate: 58.16 per year) have at least one neutron entering sensitive volume. About 65% of those events have single-neutron entering the sensitive volume while remaining events have greater than one multiplicity per event. Essentially all events with a neutron plus other particles leave enough signatures in the TPC. The number of events that survive with each progressive veto cut and TPC cut is tabulated below.

Table 5.3: Cosmogenic neutron rates in TPC satisfying veto and TPC energy cuts

(Sum) veto energy deposited	Energy deposited in TPC (MeV)	Events	Rates
< 10 MeV	< 2	9201	58.16 per year
< 10 MeV	0 < E <= 1	6022	38.06 per year
< 2 MeV	0 < E <= 1	1125	7.11 per year

The result is 27 events have less than two scatterings in LAr sensitive volume satisfying sum veto energy deposition < 2 MeV and energy deposition 0 < E <= 1 MeV (expected WIMP search range). All these have single-neutron entering TPC. There are all but eight single-scatter neutron events in 158.2 years that satisfy above veto and TPC cuts. The events and their energy deposition at various detector volumes are shown in Figure 5.12. Only five of those events have original muon leaving over GeV energy in the LAr Bath but escaping the inner detectors. In principle, such muon signal would help to discriminate the single-scatter event as a "cosmogenic neutron-like". But the LAr Bath is optically shielded from rest of the veto and TPC system. So, those muons may not be identified by the detector system. Figure 5.12 shows some of the single-scatter neutron events have very low energy deposition (< 10 keV). The nuclear recoil signal from such neutrons may not be detectable.

Run	Event ID	Energy_LArBath[GeV]	Energy_OAR[keV]	Energy_IAR[keV]	Energy_TPC[keV]	nTPC	PID
27	902839	6.08393288	181.729	1241.68	8.01099	1	['8']
93	481188	7.27475595	43.0603	204.348	24.4722	1	['8']
96	292082	17.7274113	42.846	199.051	1.64954	1	['8']
145	1532025	1.83281481	0	576.581	4.42349	1	['8']
2029	1531611	5.71605004E-03	0	1073.56	114.214	1	['8']
2036	692281	2.58009823E-05	0	111.931	4.07504	1	['8']
2078	1513039	2.78797603	224.77	311.41	62.1769	1	['8']
2224	475840	2.78061366	628.488	1303.7	11.4201	1	['8']

Figure 5.12: 8 events that satisfy sum veto energy cut < 2 MeV and deposit energy in expected WIMP energy range (0 < E <= 1) MeV. All events involve single-scatter neutron that can potentially mimic WIMP like signal. PID '8' is FLUKA-assigned particle ID for neutrons.

DarkSide-20k will detect any electronic or neutron recoil events that deposit at least 800 keV energy in one of the inner AAr veto detectors. The detectable threshold may be much lower. For an 800 keV threshold, five single neutrons are found in 158.2 years that can mimic a WIMP signal. However, if there is a coincident signal in both veto detectors, energy threshold will be 100 keV for the veto detectors. So only two events are found that can induce WIMP like signal in 158.2 years of simulation lifetime. But these events have neutron-scatter close to the TPC surface, and are removed only by fiducial cut (Only events occuring in inner 20 ton-fiducial mass will be used for WIMP searches). The simulation results show no cosmogenic neutron background event in the simulation lifetime of 158.2 years. It shows DarkSide-20k has high efficiency of rejecting cosmogenic neutron background. However, considering the desired sensitivity for DarkSide-20k is 0.1 events in WIMP box over 20t x 10y exposure, more Monte Carlo (MC) statistics is possibly needed.

If veto information is abandoned, there are 610 events with a neutron single-scatter in TPC and deposits energy of $\leq$ 1 MeV. So, the expected rate for those events is 3.86 per year. If double-scattering neutrons are also included, the corresponding event rate is 9.92 per year. These are lower limits as there is no information on the TPC-interactions for those events rejected at the TPC boundary.

Chapter 6

Summary and Perspectives

There is strong evidence from astrophysical observations for the existence of a dark matter. But the nature of dark matter is still unknown. Many experiments, employing various detector technologies, are looking for signatures from dark matter interacting with ordinary matter. Weakly interacting particles (WIMP) are heavy and weakly interacting particles. These particles appear in various extensions of the Standard Particle Model. They remain the most compelling candidate dark matter.

Direct detection experiments try to detect signals from DM scattering off some target nuclei. A typical WIMP signal is a low energy recoil of the target nuclei. Such interactions are rare (on the order of a few per ton per year). One part of the WIMP search is to understand the WIMP interaction rates and characteristics in a detector. But another more important part is to understand the backgrounds, characteristics, and interaction rates.

In this thesis, I report the results from my studies of backgrounds from the $^{42}Ar/^{42}K$ decays and the muon-induced neutron interactions for dark matter searches. The summary and conclusions from the studies are presented separately below.

$^{42}Ar/^{42}K$ background studies

^{42}Ar is a possible source of background in liquid argon (LAr) based detectors. ^{42}Ar and its daughter isotope ^{42}K are radioactive. In Chapter 4, I report various MC based studies that I carried out to understand and estimate the backgrounds from $^{42}Ar/^{42}K$ decays using DarkSide-50 data. The specific radio-activity measured for $^{42}Ar/^{42}K$ is on the order of few tens of μBq/kg. These values agree well with the ones reported in [147][150]. Various approaches that can be used to estimate the ^{42}Ar backgrounds are discussed. In each of the activities estimated, the systematics dominate the statistical uncertainties. However, each of the techniques predicts the correct order of magnitude for the specific activity of $^{42}Ar/^{42}K$.

My findings show the spectral fitting of MC background spectra on the data shows insensitivity to the spectra of ^{42}Ar-β-decays. There is a degeneracy between S1, $S1_{late}$ and tdrift spectra of ^{42}Ar-β decays and that of ^{39}Ar. The MC spectra of full ^{42}Ar decay chain and various decays in ^{42}K decay chain was used in multidimensional spectral fitting to make estimate for $^{42}Ar/^{42}K$ activity. The upper limit for $^{42}Ar/^{42}K$ was also established from the ^{42}K β-γ search in atmospheric argon. The order of estimate is in agreement with the specific activity estimates from other liquid argon based experiments. The systematic effects are found to be a lot easier to handle with this signal-search approach compared to the spectral fitting approach.

The ^{42}K isotopes may drift in the uniform electric field of Time Projection Chamber (TPC). Some simplified MC scenarios for distribution of ^{42}K isotopes were investigated, and the spectra were incorporated in the multidimensional spectral fitting analysis. Our studies give a null estimate for ^{42}K activity at the top of TPC, and ~ 10 μ Bq/kg at the bottom. i.e. There is a small preference for ^{42}K isotopes to gain positive charge and move towards the bottom of the TPC.

The cosmogenically-shielded (underground) argon is expected to have a smaller concentration of ^{42}Ar. No obvious conclusions can be drawn based on my multidimensional spectral fitting studies. The MC fitting on both atmospheric argon and underground argon data-sets gave similar order of estimate.

TPC of the DS-20k detector will be filled will tonnes of argon extracted from the underground. The concentration of $^{42}Ar/^{42}K$ is expected to be smaller than in atmospheric argon. The DS-20k experiment can measure the specific activity of $^{42}Ar/^{42}K$ in underground argon. One possible avenue for search will be to look for single-scatter electronic recoil events (β-induced like) at higher energies (> 1 MeV). There are few radioactive isotopes (mostly the daughter isotopes in ^{222}Rn) that emit high energy β-particles with the active liquid argon sensitive volume like ^{42}K does. Looking for single-scatter β-like events, one can reject the backgrounds from the high energy multiple-scattering γ events.

In DarkSide-20k, the surrounding veto detectors will have tons of atmospheric argon. The $^{42}Ar/^{42}K$ decays may result in pile-up of events and accidental coincidences in atmospheric argon (AAr) vetoes. But the rate for this to occur is expected to be low and has little effect on the detector's performance. 1524 keV γ's from ^{42}K decay in veto detectors may penetrate the acrylic shell and reach TPC triggering the data acquisition system occasionally. Also, there will be little or no ^{60}Co and ^{40}K γ backgrounds in DarkSide-20k, so a ^{42}K 1524 keV γ peak may be observed above the backgrounds in the veto scintillation spectrum. Another mode of signal search can be carried out by identifying the ^{42}K γ scattering in the TPC in prompt coincidence with the β (Q = 2001 keV) scattering in AAr veto.

The precise measurement of ^{42}Ar based on ^{42}Ar β signal search in the data or through the spectral fitting technique is difficult. In both atmospheric and underground argon, the concentration of β-decaying isotope ^{39}Ar is several times higher than ^{42}Ar. Both ^{39}Ar and ^{42}Ar β-decays have similar end-point energies. Further, both of them are first forbidden unique decays and have similar β spectral shapes. So, the measurements based on ^{42}K channel has to be exploited to measure the $^{42}Ar/^{42}K$ radioactivity. But for dual-phase liquid-argon experiments, Monte Carlo-based estimation of the radioactivity through that channel is also not so easy. From GERDA's findings, ^{42}K isotopes may drift in the electric field within the detector. ^{42}K distribution could neither be entirely homogeneous nor discrete but could have complex dependence on the detector's electric field configuration. In larger liquid argon based detectors like DarkSide-20k and LEGEND, it may be possible to model the isotopic distribution of ^{42}K as a function of depth for a given electric field configuration.

Also, the measured radioactivities may vary across experiments depending on the initial concentration of ^{42}Ar getting into liquid argon. The concentration of ^{42}Ar in liquid argon may depend on several factors: location of Argon extraction site, purity of LAr, amount of exposure during shipping, etc. In DarkSide-20k, any attempt to reduce concentration of ^{39}Ar in liquid argon through cryogenic distillation may also remove some ^{42}Ar.

From a future perspective, a better understanding of reaction cross-sections and rates leading to ^{42}Ar production, and precise measurement of spectral shapes of the forbidden decays from the isotopes in ^{42}Ar chain are also necessary to better characterize and estimate ^{42}Ar background.

The $^{42}Ar/^{42}K$ decays would induce electronic recoils in liquid argon. These recoil events are efficiently discriminated by pulse shape discrimination on S1 (based on the f90 parameter). So, $^{42}Ar/^{42}K$-decays are not critical backgrounds for WIMP dark matter searches. However, high energy ^{42}K β events could be more serious backgrounds to solar neutrino event searches with argon-based future detectors like ARGO. Next-generation experiment LEGEND, the experiment pursuing Ge-based neutrino-less double beta decay ($0\nu\beta\beta$) searches will have liquid argon veto. The high energy ^{42}K β events may pose a serious backgrounds around the expected $0\nu\beta\beta$ signal (at 2039 keV). The next-generation liquid-argon based experiments strive for larger size (increased liquid argon mass) and greater sensitivity to rare event searches. So, it is important to carry out more studies to understand and measure precisely the backgrounds from $^{42}Ar/^{42}K$ in those searches.

Cosmogenic neutron background studies

Cosmogenic (muon-induced) neutrons are an important background to the direct detection of WIMPs (Weakly Interacting Massive Particles) in dark matter searches with underground detectors. In Chapter 5, I present the results from the FLUKA simulation studies of the cosmogenic neutron background I carried out for the DarkSide-20k detector.

In my studies, I find the outer cryostat system (and the liquid argon bath) act as an excellent passive shield for cosmogenic events. However, unlike in DarkSide-50, which has smaller TPC surrounded by large veto detectors, DarkSide-20k will have large TPC with comparatively smaller veto detectors. The simulation results suggest that the atmospheric argon veto detectors will not shield the inner TPC well. So, the DarkSide-20k TPC will be exposed to larger cosmogenic event rate (approximately 580 per day). However, the FLUKA studies show the veto detector system is able to identify and discriminate most of the cosmogenic neutrons. The cosmogenic neutron background rate with active tagging by the veto system is < 7.11 events per year. The veto efficiency of rejecting cosmogenic neutron background is smaller than that of DarkSide-50. It suggests we rely more on TPC event reconstruction, and the TPC cuts (multi-scatter and fiducial cut) to reject the remaining cosmogenic neutron backgrounds that can't be rejected based on the energy deposited in the veto detectors alone. But with the veto and TPC cuts, no WIMP-like neutron event is observed in simulation lifetime of approximately 158 years for DarkSide-20k. This suggests the DarkSide-20k is able to reject cosmogenic neutron backgrounds with very high efficiency. However, considering the high sensitivity desired for WIMP searches with DarkSide-20k, larger Monte Carlo (MC) statistics is necessary. This study shows the efficiency of veto detectors to reject the cosmogenic neutron backgrounds increases if the veto energy threshold is lowered or/and the energy deposition by the cosmogenic events in liquid argon bath is measured.

It is important to carry out GEANT4 studies to cross-validate the results obtained from the FLUKA simulation studies, especially the cosmogenic neutron background rate. GEANT4-based study allows one way to compute systematic uncertainties on FLUKA-predicted results. As low-energy-neutron treatment in FLUKA is different than in GEANT4, there is also a physics case to cross-validate the results with GEANT4-based studies.

This work was focused on studying the prompt cosmogenic neutron background for DarkSide-20k. The muons or muon-induced interactions within the detector can produce short-lived radioactive isotopes. These "cosmogenically" activated isotopes can emit neutrons in delayed data acquisition windows. It is important to study the delayed neutron backgrounds and estimate their rates. We can also investigate the possibility of vetoing the cosmogenic event based on the energy deposition in liquid argon bath, as it increases the detector's ability to reject "prompt" neutron backgrounds, and possibly the "delayed" cosmogenic neutron backgrounds.

Bibliography

[1] K. Freese. Review of observational evidence for dark matter in the universe and in upcoming searches for dark stars. *European Astronomical Society Publications Series*, 36:113–126, 2009.

[2] P. A. R. Ade, N. Aghanim, M. I. R. Alves, C. Armitage-Caplan, M. Arnaud, M. Ashdown, F. Atrio-Barandela, J. Aumont, et al. Planck 2013 results. I. Overview of products and scientific results. *Astronomy & Astrophysics*, 571:A1, 2014.

[3] S. Burles, K. M. Nollett, and M. S. Turner. Big bang nucleosynthesis predictions for precision cosmology. *The Astrophysical Journal Letters*, 552(1):L1–L5, 2001.

[4] D. Clowe, M. Bradač, A. H. Gonzalez, M. Markevitch, S. W. Randall, C. Jones, and D. Zaritsky. A direct empirical proof of the existence of dark matter. *The Astrophysical Journal Letters*, 648(2):L109–L113, 2006.

[5] M. Schumann. Direct detection of WIMP dark matter: concepts and status. *Journal of Physics G: Nuclear and Particle Physics*, 46(10):103003, 2019.

[6] C. E. Aalseth, F. Acerbi, P. Agnes, I. F. M. Albuquerque, T. Alexander, A. Alici, A. K. Alton, P. Antonioli, et al. DarkSide-20k: A 20 tonne two-phase LAr TPC for direct dark matter detection at LNGS. *The European Physical Journal Plus*, 133(3):131, 2018.

[7] P. Agnes, T. Alexander, A. K. Alton, K. Arisaka, H. O. Back, B. Baldin, K. Biery, G. Bonfini, et al. First results from the DarkSide-50 dark matter experiment at Laboratori Nazionali del Gran Sasso. *Physics Letters B*, 743:456–466, 2015.

[8] P. Agnes, I. F. M. Albuquerque, T. Alexander, A. K. Alton, D. M. Asner, H. O. Back, K. Biery, V. Bocci, et al. Simulation of argon response and light detection in the DarkSide-50 dual phase TPC. *Journal of Instrumentation*, 12(10):P10015, 2017.

[9] P. Agnes, I. F. M. Albuquerque, T. Alexander, A. K. Alton, G. R. Araujo, M. Ave, H. O. Back, B. Baldin, et al. DarkSide-50 532-day dark matter search with low-radioactivity argon. *Physical Review D*, 98(10):102006, 2018.

[10] P. Benetti, F. Calaprice, E. Calligarich, M. Cambiaghi, F. Carbonara, F. Cavanna, A. G. Cocco, F. di Pompeo, et al. Measurement of the specific activity of Ar-39 in natural argon. *Nuclear Instruments and Methods in Physics Research A Accelerators Spectrometers Detectors and Associated Equipment*, 574(1):83–88, 2006.

[11] L. Baudis, A. Brown, C. Capelli, M. Galloway, S. Kazama, A. Kish, S. Reichard, J. Wulf, et al. Dark matter search results from a one ton-year exposure of XENON1T. *Physical Review Letters*, 121(11):111302, 2018.

[12] X. Cui, A. Abdukerim, W. Chen, X. Chen, Y. Chen, B. Dong, D. Fang, C. Fu, K. Giboni, F. Giuliani, et al. Dark matter results from 54-ton-day exposure of PandaX-II experiment. *Physical Review Letters*, 119(18):181302–181309, 2017.

[13] D. S. Akerib, S. Alsum, H. M. Araújo, X. Bai, A. J. Bailey, J. Balajthy, P. Beltrame, E. P. Bernard, A. Bernstein, T. P. Biesiadzinski, et al. Results from a search for dark matter in the complete LUX exposure. *Physical Review Letters*, 118(2):021303–021312, 2017.

[14] P. Agnes, L. Agostino, I. F. M. Albuquerque, T. Alexander, A. K. Alton, K. Arisaka, H. O. Back, B. Baldin, et al. Results from the first use of low radioactivity argon in a dark matter search. *Physical Review D*, 93(8):081101, 2016.

[15] J. Chen and B. Singh. Nuclear data sheets for A= 42. *Nuclear Data Sheets*, 135:1–192, 2016.

[16] A. Empl, E. V. Hungerford, R. Jasim, and P. Mosteiro. A Fluka study of underground cosmogenic neutron production. *Journal of Cosmology and Astroparticle Physics*, 2014(08):064, 2014.

[17] F. Zwicky. On the masses of nebulae and of clusters of nebulae. *The Astrophysical Journal*, 86:217–246, 1937.

[18] V. C. Rubin. Dark matter in spiral galaxies. *Scientific American*, 248:96–109, 1983.

[19] R. P. Olling and M. R. Merrifield. Luminous and dark matter in the Milky Way. *Monthly Notices of the Royal Astronomical Society*, 326:164–180, 2001.

[20] C. S. Frenk, S. D. M. White, G. Efstathiou, and M. Davis. Cold dark matter, the structure of galactic haloes and the origin of the Hubble sequence. *Nature*, 317:595–597, 1987.

[21] P. Quini, J. Salmon, and W. Zurek. Primordial density fluctuations and the structure of galactic haloes. *Nature*, 322:329–335, 1986.

[22] J. Dubinski and R. G. Carlberg. The structure of cold dark matter halos. *The Astrophysical Journal*, 378:496–503, 1991.

[23] J. F. Navarro, C. S. Frenk, and S. D. M White. A universal density profile from hierarchical clustering. *The Astrophysical Journal*, 490(2):493–508, 1997.

[24] L. Hernquist. An analytical model for spherical galaxies and bulges. *The Astrophysical Journal*, 356:359–364, 1990.

[25] S. Kazantzidis, J. Magorrian, and B. Moore. Generating equilibrium dark matter halos: Inadequacies of the local Maxwellian approximation. *The Astrophysical Journal*, 601(1):37–46, 2004.

[26] J. C. Mather, E. S. Cheng, D. A. Cottingham, Jr. Eplee, R. E., D. J. Fixsen, T. Hewagama, R. B. Isaacman, K. A. Jensen, S. S. Meyer, et al. Measurement of the cosmic microwave background spectrum by the COBE FIRAS instrument. *The Astrophysical Journal*, 420:439–444, 1994.

[27] N. Jarosik, C. L. Bennett, J. Dunkley, B. Gold, M. R. Greason, M. Halpern, R. S. Hill, G. Hinshaw, et al. Seven-year wilkinson microwave anisotropy probe (WMAP*) observations: sky maps, systematic errors, and basic results. *The Astrophysical Journal Supplement Series*, 192(2):14–, 2011.

[28] A. A. Penzias and R. W. Wilson. A measurement of excess antenna temperature at 4080 Mc/s. *The Astrophysical Journal*, 142:419–421, 1965.

[29] P. de Bernardis, P. A. R. Ade, J. J. Bock, J. R. Bond, J. Borrill, A. Boscaleri, K. Coble, B. P. Crill, et al. A flat Universe from high-resolution maps of the cosmic microwave background radiation. *Nature*, 404:955–959, 2000.

[30] M. Bucher. Physics of the cosmic microwave background anisotropy. *International Journal of Modern Physics D*, 24(02):1530004, 2015.

[31] S. Burles and D. Tytler. The Deuterium abundance toward Q1937–1009. *The Astrophysical Journal*, 499(2):699–712, 1998.

[32] P. J. E. Peebles. Large-scale background temperature and mass fluctuations due to scale-invariant primeval perturbations. *The Astrophysical Journal*, 263:1:L1–L5, 1982.

[33] G. R. Blumenthal, H. Pagels, and J. R. Primack. Galaxy formation by dissipationless particles heavier than neutrinos. *Nature*, 299(5878):37–38, 1982.

[34] J. R. Bond, A. S. Szalay, and M. S. Turner. Formation of galaxies in a gravitino-dominated universe. *Physical Review Letters*, 48(23):1636–1640, 1982.

[35] G. R. Blumenthal, Primack J. R. Faber, S. M., and M. J. Rees. Formation of galaxies and large-scale structure with cold dark matter. *Nature*, 311:517–525, 1984.

[36] D. Kirkman, D. Tytler, N. Suzuki, J. M. O'Meara, and D. Lubin. The cosmological baryon density from the deuterium-to-hydrogen ratio in QSO absorption systems: D/H toward Q1243+ 3047. *The Astrophysical Journal Supplement Series*, 149:1–28, 2003.

[37] V. W. Robert, W. A. Fowler, and F. Hoyle. On the synthesis of elements at very high temperatures. *The Astrophysical Journal*, 148, 1967.

[38] Particle Data Group et al. Review of particle physics. *Chinese Physics C*, 40(10):100001, 2016.

[39] C. J. Copi, D. N. Schramm, and M. S. Turner. Big-bang nucleosynthesis and the baryon density of the universe. *Science*.

[40] A. Einstein. The foundation of the general theory of relativity. *Annalen der Physik*, 49(7):769–822, 1916.

[41] J. Wambsganss. Gravitational lensing in astronomy. *Living Reviews in Relativity*, 1(1):12, 1998.

[42] D. Maoz, J. N. Bahcall, D. P. Schneider, R. Doxsey, N. A. Bahcall, A. V. Filippenko, W. M. Goss, O. Lahav, and B. Yanny. A gravitational lens candidate discovered with the Hubble Space Telescope. *The Astrophysical Journal*, 386:L1–L3, 1992.

[43] J. Lehár, E. E. Falco, C. S. Kochanek, B. A. McLeod, J. A. Munoz, C. D. Impey, H. W. Rix, C. R. Keeton, and C. Y. Peng. Hubble Space Telescope observations of 10 two-image gravitational lenses. *The Astrophysical Journal*, 536(2):584–605, 2000.

[44] J. P. Kneib, R. S. Ellis, I. Smail, W. J. Couch, and R. M. Sharples. Hubble Space Telescope observations of the lensing cluster Abell 2218. *The Astrophysical Journal*, 471(2):643–656, 1996.

[45] S. A. Grossman and R. Narayan. Gravitationally lensed images in Abell 370. *The Astrophysical Journal*, 344:637–644, 1989.

[46] I. Ferreras, P. Saha, and L. L. R. Williams. Stellar and total mass in early-type lensing galaxies. *The Astrophysical Journal Letters*, 623(1):L5–L8, 2005.

[47] I. Ferreras, P. Saha, and S. Burles. Unveiling dark haloes in lensing galaxies. *Monthly Notices of the Royal Astronomical Society*, 383(3):857–863, 2008.

[48] E. Aubourg, P. Bareyre, S. Brehin, M. Gros, M. Lachieze-Rey, B. Laurent, E. Lesquoy, C. Magneville, et al. Evidence for gravitational microlensing by dark objects in the galactic halo. *Nature*, 365(6447):623–625, 1993.

[49] C. Alcock, R. A. Allsman, D. Alves, R. Ansari, E. Aubourg, T. S. Axelrod, P. Bareyre, , J. P. Beaulieu, et al. EROS and MACHO combined limits on planetary-mass dark matter in the galactic halo. *The Astrophysical Journal Letters*, 499(1):L9–L12, 1998.

[50] C. Alcock, R. A. Allsman, D. Alves, T. S. Axelrod, A. C. Becker, D. P. Bennett, K. H. Cook, K. C. Freeman, et al. The MACHO project: limits on planetary mass dark matter in the galactic halo from gravitational microlensing. *The Astrophysical Journal*, 471(2):774–782, 1996.

[51] P. Tisserand, L. Le Guillou, C. Afonso, J. N. Albert, J. Andersen, R. Ansari, É. Aubourg, P. Bareyre, et al. Limits on the Macho content of the galactic halo from the EROS-2 survey of the Magellanic Clouds. *Astronomy & Astrophysics*, 469(2):387–404, 2007.

[52] M. Bradač, D. Clowe, A. H. Gonzalez, P. Marshall, W. Forman, C. Jones, M. Markevitch, S. W. Randall, T. Schrabback, and D. Zaritsky. Strong and weak lensing united. III. Measuring the mass distribution of the merging galaxy cluster 1ES 0657–558. *The Astrophysical Journal*, 652(2):937–947, 2006.

[53] M. Bradač, S. W. Allen, T. Treu, H. Ebeling, R. Massey, R. G. Morris, A. Von Der Linden, and D. Applegate. Revealing the properties of dark matter in the merging cluster macs j0025. 4–1222. *The Astrophysical Journal*, 687(2):959–967, 2008.

[54] J. D. Bekenstein. Relativistic gravitation theory for the modified Newtonian dynamics paradigm. *Physical Review D*, 70(8):083509, 2004.

[55] C. Skordis, D. F. Mota, P. G. Ferreira, and C. Boehm. Large scale structure in Bekenstein's theory of relativistic modified Newtonian dynamics. *Physical Review Letters*, 96(1):011301, 2006.

[56] R. D. Peccei and H. R. Quinn. Constraints imposed by CP conservation in the presence of pseudoparticles. *Physical Review D*, 16(6):1791–1797, 1977.

[57] S. Weinberg. A new light boson? *Physical Review Letters*, 40(4):223–226, 1978.

[58] F. Wilczek. Problem of strong p and t invariance in the presence of instantons. *Physical Review Letters*, 40(5):279–282, 1978.

[59] R. D. Peccei. The strong CP problem and axions. *Lecture Notes in Physics (Axions)*, 741:3–17, 2009.

[60] R. Jackiw and C. Rebbi. Vacuum periodicity in a Yang-Mills quantum theory. *Physical Review Letters*, 37(3):172–175, 1976.

[61] L. D. Duffy and K. Van Bibber. Axions as dark matter particles. *New Journal of Physics*, 11(10):105008, 2009.

[62] C. A. Baker, D. D. Doyle, P. Geltenbort, K. Green, M. G. D. Van der Grinten, P. G. Harris, P. Iaydjiev, S. N. Ivanov, et al. Improved experimental limit on the electric dipole moment of the neutron. *Physical Review Letters*, 97(13):131801, 2006.

[63] P. Sikivie. Axion cosmology. *Lecture Notes in Physics (Axions)*, 741:19–50, 2008.

[64] G. G. Raffelt. Astrophysical methods to constrain axions and other novel particle phenomena. *Physics Reports*, 198(1-2):1–113, 1990.

[65] J. E. Kim. Light pseudoscalars, particle physics and cosmology. *Physics Reports*, 150(1):1–177, 1987.

[66] H. Primakoff. Photo-production of neutral mesons in nuclear electric fields and the mean life of the neutral meson. *Physical Review*, 81(5):899, 1951.

[67] N. Du, N. Force, R. Khatiwada, E. Lentz, R. Ottens, L. J. Rosenberg, G. Rybka, G. Carosi, et al. Search for invisible axion dark matter with the axion dark matter experiment. *Physical Review Letters*, 120(15):151301, 2018.

[68] T. Braine, R. Cervantes, N. Crisosto, N. Du, S. Kimes, L. J. Rosenberg, G. Rybka, J. Yang, et al. Extended search for the invisible axion with the axion dark matter experiment. *Physical Review Letters*, 124(10):101303, 2020.

[69] Y. Fukuda, T. Hayakawa, E. Ichihara, K. Inoue, K. Ishihara, H. Ishino, Y. Itow, T. Kajita, et al. Evidence for oscillation of atmospheric neutrinos. *Physical Review Letters*, 81(8):1562–1567, 1998.

[70] Q. R. Ahmad, R. C. Allen, T. C. Andersen, J. D. Anglin, J. C. Barton, E. W. Beier, M. Bercovitch, J. Bigu, et al. Direct evidence for neutrino flavor transformation from neutral-current interactions in the Sudbury Neutrino Observatory. *Physical Review Letters*, 89(1):011301, 2002.

[71] J. Lesgourgues and S. Pastor. Neutrino cosmology and Planck. *New Journal of Physics*, 16(6):065002, 2014.

[72] D. H. Perkins. *Particle Astrophysics (Second Edition)*. Oxford University Press, 2009.

[73] K. N. Abazajian, K. Arnold, J. Austermann, B. A. Benson, C. Bischoff, J. Bock, J. R. Bond, Borrill, et al. Neutrino physics from the cosmic microwave background and large scale structure. *Astroparticle Physics*, 63:66–80, 2015.

[74] M. Jeżabek and Y. Sumino. Neutrino mixing and see-saw mechanism. *Physics Letters B*, 440(3-4):327–331, 1998.

[75] E. K. Akhmedov, G. C. Branco, and M. N. Rebelo. Seesaw mechanism and structure of neutrino mass matrix. *Physics Letters B*, 478(1-3):215–223, 2000.

[76] L. Roszkowski, E. M. Sessolo, and S. Trojanowski. WIMP dark matter candidates and searches- current status and future prospects. *Reports on Progress in Physics*, 81(6):066201, 2018.

[77] A. Boyarsky, M. Drewes, T. Lasserre, S. Mertens, and O. Ruchayskiy. Sterile neutrino dark matter. *Progress in Particle and Nuclear Physics*, 104:1–45, 2019.

[78] A. Merle. *Sterile Neutrino Dark Matter*. Morgan & Claypool Publishers, 2017.

[79] E. Figueroa-Feliciano. Direct detection searches for WIMP dark matter. *Progress in Particle and Nuclear Physics*, 66(3):661–673, 2011.

[80] J. Ellis, J. S. Hagelin, D. V. Nanopoulos, K. Olive, and M. Srednicki. Supersymmetric relics from the big bang. *Nuclear Physics B*, 238(2):453–476, 1984.

[81] G. Bertone. The moment of truth for WIMP dark matter. *Nature*, 468(7322):389–393, 2010.

[82] G. Jungman, M. Kamionkowski, and K. Griest. Supersymmetric dark matter. *Physics Reports*, 267(5-6):195–373, 1996.

[83] S. Chatrchyan, V. Khachatryan, A. M. Sirunyan, A. Tumasyan, W. Adam, E. Aguilo, T. Bergauer, M. Dragicevic, et al. Observation of a new boson at a mass of 125 GeV with the CMS experiment at the LHC. *Physics Letters B*, 716(1):30–61, 2012.

[84] J. Ellis and D. Ross. A light Higgs boson would invite supersymmetry. *Physics Letters B*, 506(3-4):331–336, 2001.

[85] J. E. Gunn, B. W. Lee, D. N. Schramm, and G. Steigman. Some astrophysical consequences of the existence of a heavy stable neutral lepton. *The Astrophysical Journal*, 223:1015–1031, 1978.

[86] L. Bergström. Non-baryonic dark matter: observational evidence and detection methods. *Reports on Progress in Physics*, 63(5):793–841, 2000.

[87] T. Bringmann and C. Weniger. Gamma ray signals from dark matter: Concepts, status and prospects. *Physics of the Dark Universe*, 1(1-2):194–217, 2012.

[88] O. Buchmueller, C. Doglioni, and L. T. Wang. Search for dark matter at colliders. *Nature Physics*, 13(3):217–223, 2017.

[89] M. W. Goodman and E. Witten. Detectability of certain dark-matter candidates. *Physical Review D*, 31:3059–3063, 1985.

[90] G. Bertone. *Particle dark matter: observations, models and searches*. Cambridge University Press, 2010.

[91] R. Agnese, A. J. Anderson, M. Asai, D. Balakishiyeva, R. B. Thakur, D. A. Bauer, J. Beaty, J. Billard, et al. Search for low-mass weakly interacting massive particles with SuperCDMS. *Physical Review Letters*, 112(24):241302–241308, 2014.

[92] P. A. Amaudruz, M. Baldwin, M. Batygov, B. Beltran, C. E. Bina, D. Bishop, J. Bonatt, G. Boorman, et al. First results from the DEAP-3600 dark matter search with argon at SNOLAB. *Physical Review Letters*, 121(7):071801–071811, 2018.

[93] E. Armengaud, C. Augier, A. Benoit, L. Bergé, T. Bergmann, J. Blümer, A. Broniatowski, V. Brudanin, et al. Search for low-mass WIMPs with EDELWEISS-II heat-and-ionization detectors. *Physical Review D*, 86(5):051701–051707, 2012.

[94] E. Aprile, J. Aalbers, F. Agostini, M. Alfonsi, F. D. Amaro, M. Anthony, F. Arneodo, P. Barrow, et al. First dark matter search results from the XENON1T experiment. *Physical Review Letters*, 119(18):181301–181307, 2017.

[95] J. Xia, A. Abdukerim, W. Chen, X. Chen, Y. Chen, X. Cui, D. Fang, C. Fu, et al. PandaX-II constraints on spin-dependent WIMP-nucleon effective interactions. *Physics Letters B*, 792:193–198, 2019.

[96] E. Aprile, J. Aalbers, F. Agostini, M. Alfonsi, L. Althueser, F. D. Amaro, M. Anthony, Antochi, et al. Constraining the spin-dependent WIMP-nucleon cross sections with XENON1T. *Physical Review Letters*, 122(14):141301, 2019.

[97] C. Amole, M. Ardid, I. J. Arnquist, D. M. Asner, D. Baxter, E. Behnke, M. Bressler, B. Broerman, et al. Dark matter search results from the complete exposure of the PICO-60 C_3F_8 bubble chamber. *Physical Review D*, 100(2):022001, 2019.

[98] J. D. Lewin and P. F. Smith. Review of mathematics, numerical factors, and corrections for dark matter experiments based on elastic nuclear recoil. *Astroparticle Physics*, 6(1):87–112, 1996.

[99] K. Abe, K. Hiraide, K. Ichimura, Y. Kishimoto, K. Kobayashi, M. Kobayashi, S. Moriyama, M. Nakahata, et al. A direct dark matter search in XMASS-I. *Physics Letters B*, 789:45–53, 2019.

[100] E. Armengaud, C. Augier, A. Benoît, L. Bergé, J. Billard, A. Broniatowski, P. Camus, A. Cazes, et al. Searches for electron interactions induced by new physics in the EDELWEISS-III germanium bolometers. *Physical Review D*, 98(8):082004, 2018.

[101] R. Agnese, T. Aramaki, I. J. Arnquist, W. Baker, D. Balakishiyeva, S. Banik, D. Barker, R. B. Thakur, et al. Results from the super cryogenic dark matter search experiment at soudan. *Physical Review Letters*, 120(6):061802, 2018.

[102] F. Petricca, G. Angloher, P. Bauer, A. Bento, C. Bucci, L. Canonica, X. Defay, A. Erb, et al. First results on low-mass dark matter from the CRESST-III experiment. *Journal of Physics: Conference Series*, 1342(1):012076, 2020.

[103] D. S. Akerib, H. M. Araújo, X. Bai, A. J. Bailey, J. Balajthy, S. Bedikian, E. Bernard, A. Bernstein, et al. First results from the LUX dark matter experiment at the Sanford Underground Research Facility. *Physical Review Letters*, 112(9):091303, 2014.

[104] P. Agnes, I. F. M. Albuquerque, T. Alexander, A. K. Alton, G. R. Araujo, D. M. Asner, M. Ave, H. O. Back, et al. Low-mass dark matter search with the DarkSide-50 experiment. *Physical Review Letters*, 121(8):081307, 2018.

[105] D. S. Akerib, S. Alsum, H. M. Araújo, X. Bai, A. J. Bailey, J. Balajthy, P. Beltrame, E. P. Bernard, et al. Limits on spin-dependent WIMP-nucleon cross section obtained from the complete LUX exposure. *Physical Review Letters*, 118(25):251302, 2017.

[106] A. J. Anderson, J. M. Conrad, E. Figueroa-Feliciano, K. Scholberg, and J. Spitz. Coherent neutrino scattering in dark matter detectors. *Physical Review D*, 84(1):013008, 2011.

[107] P. Agnes, I. F. M. Albuquerque, T. Alexander, A. K. Alton, G. R. Araujo, D. M. Asner, M. Ave, H. O. Back, et al. Constraints on sub-GeV dark-matter–electron scattering from the darkSide-50 experiment. *Physical Review Letters*, 121(11):111303, 2018.

[108] P. Agnes, L. Agostino, I. F. M. Albuquerque, T. Alexander, A. K. Alton, K. Arisaka, H. O. Back, B. Baldin, et al. The veto system of the DarkSide-50 experiment. *Journal of Instrumentation*, 11(03):P03016, 2016.

[109] A. Wright, P. Mosteiro, B. Loer, and F. Calaprice. A highly efficient neutron veto for dark matter experiments. *Nuclear Instruments and Methods in Physics Research Section A Accelerators Spectrometers Detectors and Associated Equipment*, 644(1):18–26, 2011.

[110] G. Alimonti, C. Arpesella, G. Bacchiocchi, M. Balata, G. Bellini, J. Benziger, S. Bonetti, A. Brigatti, et al. A large-scale low-background liquid scintillation detector: the counting test facility at Gran Sasso. *Nuclear Instruments and Methods in Physics Research Section A Accelerators Spectrometers Detectors and Associated Equipment*, 406(3):411–426, 1998.

[111] M. Janecek. Reflectivity spectra for commonly used reflectors. *IEEE Transactions on Nuclear Science*, 59(3):490–497, 2012.

[112] G. Bellini, J. Benziger, D. Bick, G. Bonfini, D. Bravo, M. B. Avanzini, B. Caccianiga, L. Cadonati, et al. Cosmic-muon flux and annual modulation in Borexino at 3800 m water-equivalent depth. *Journal of Cosmology and Astroparticle Physics*, 2012(05):015, 2012.

[113] P. A. Amaudruz, M. Baldwin, M. Batygov, B. Beltran, C. E. Bina, D. Bishop, J. Bonatt, G. Boorman, et al. Design and construction of the DEAP-3600 dark matter detector. *Astroparticle Physics*, 108:1–23, 2019.

[114] B. Abi, R. Acciarri, M. A. Acero, M. Adamowski, C. Adams, D. L. Adams, P. Adamson, M. Adinolfi, Z. Ahmad, C. H. Albright, et al. The single-phase ProtoDUNE technical design report. *arXiv:1706.07081*, 2017.

[115] T. Doke, H. J. Crawford, A. Hitachi, J. Kikuchi, P. J. Lindstrom, K. Masuda, E. Shibamura, and T. Takahashi. Let dependence of scintillation yields in liquid argon. *Nuclear Instruments and Methods in Physics Research Section A Accelerators Spectrometers Detectors and Associated Equipment*, 269(1):291–296, 1988.

[116] T. Doke, A. Hitachi, J. Kikuchi, K. Masuda, H. Okada, and E. Shibamura. Absolute scintillation yields in liquid argon and xenon for various particles. *Japanese Journal of Applied Physics*, 41(3R):1538, 2002.

[117] L. Baudis. WIMP dark matter direct-detection searches in noble gases. *Physics of the Dark Universe*, 4:50–59, 2014.

[118] A. Hitachi, T. Takahashi, N. Funayama, K. Masuda, J. Kikuchi, and T. Doke. Effect of ionization density on the time dependence of luminescence from liquid argon and xenon. *Physical Review B*, 27(9):5279–5285, 1983.

[119] M. Miyajima, T. Takahashi, S. Konno, T. Hamada, S. Kubota, H. Shibamura, and T. Doke. Average energy expended per ion pair in liquid argon. *Physical Review A*, 9(3):1438–1443, 1974.

[120] D. M. Mei, Z. B. Yin, L. C. Stonehill, and A. Hime. A model of nuclear recoil scintillation efficiency in noble liquids. *Astroparticle Physics*, 30(1):12–17, 2008.

[121] D. Gastler, E. Kearns, A. Hime, L. C. Stonehill, S. Seibert, J. Klein, W. H. Lippincott, D. N. Mckinsey, and J. A. Nikkel. Measurement of scintillation efficiency for nuclear recoils in liquid argon. *Physical Review C*, 85:065811.

[122] P. Agnes, I. F. M. Albuquerque, T. Alexander, A. K. Alton, D. M. Asner, M. P. Ave, H. O. Back, B. Baldin, et al. Electroluminescence pulse shape and electron diffusion in liquid argon measured in a dual-phase TPC. *Nuclear Instruments and Methods in Physics Research Section A Accelerators Spectrometers Detectors and Associated Equipment*, 904:23–34, 2018.

[123] P. Cennini, S. Cittolin, D. D. Giudice, J. P. Revol, C. Rubbia, W. H. Tian, X. Li, P. Picchi, et al. On atmospheric 39Ar and 42Ar abundance. *Nuclear Instruments and Methods in Physics Research Section A: Accelerators, Spectrometers, Detectors and Associated Equipment*, 356(2-3):526–529, 1995.

[124] D. Acosta-Kane, R. Acciarri, O. Amaize, M. Antonello, B. Baibussinov, M. B. Ceolin, C. J. Ballentine, R. Bansal, et al. Discovery of underground argon with low level of radioactive 39Ar and possible applications to WIMP dark matter detectors. *Nuclear Instruments and Methods in Physics Research Section A Accelerators Spectrometers Detectors and Associated Equipment*, 587(1):46–51, 2008.

[125] H. O. Back, F. Calaprice, C. Condon, E. de Haas, R. Ford, C. Galbiati, A. Goretti, T. Hohman, A. Inanni, B. Loer, and D. Montanari. First large scale production of low radioactivity argon from underground sources. *arXiv:1204.6024*, 2012.

[126] H. O. Back, T Alexander, A. Alton, C. Condon, E. de Haas, C. Galbiati, A. Goretti, T. Hohmann, A. Ianni, C. Kendziora, and B. Loer. First commissioning of a cryogenic distillation column for low radioactivity underground argon. *arXiv:1204.6061*, 2012.

[127] T. Alexander, D. Alton, K. Arisaka, H. O. Back, P. Beltrame, J. Benziger, G. Bonfini, A. Brigatti, et al. Light yield in DarkSide-10: A prototype two-phase argon TPC for dark matter searches. *Astroparticle Physics*, 49:44–51, 2013.

[128] P. Agnes. Direct Search for dark Matter with the DarkSide experiment. PhD thesis, APC, Paris, 2016.

[129] C. Bœhm and P. Fayet. Scalar dark matter candidates. *Nuclear Physics B*, 683(1):219–263, 2004.

[130] J. L. Feng and J. Kumar. Dark-matter particles without weak-scale masses or weak interactions. *Physical Review Letters*, 101(23):231301, 2008.

[131] D. Hooper and K. M. Zurek. Natural supersymmetric model with MeV dark matter. *Physical Review D*, 77(8):087302, 2008.

[132] K. Winger, J. Feichter, M. B. Kalinowski, H. Sartorius, and C. Schlosser. A new compilation of the atmospheric 85krypton inventories from 1945 to 2000 and its evaluation in a global transport model. *Journal of Environmental Radioactivity*, 80(2):183–215, 2005.

[133] J. Ahlswede, S. J. Hebel, R. M. Ross, J. O. Schoetter, and B. Kalinowski. Update and improvement of the global krypton-85 emission inventory. *Journal of Environmental Radioactivity*, 115:34–42, 2013.

[134] N. E. Holden, T. B. Coplen, J. K. Böhlke, L. V. Tarbox, J. Benefield, J. R. de Laeter, P. G. Mahaffy, G. O'Connor, et al. IUPAC Periodic table of the elements and isotopes (IPTEI) for the education community (IUPAC Technical Report). *Pure and Applied Chemistry*, 90(12):1833–2092, 2018.

[135] E. Browne. Nuclear data Sheets for A= 232. *Nuclear Data Sheets*, 107(10):2579–2648, 2006.

[136] E. Browne and J. K. Tuli. Nuclear data sheets for A= 235. *Nuclear Data Sheets*, 122:205–292, 2014.

[137] E. Browne and J. K. Tuli. Nuclear data Sheets for A= 238. *Nuclear Data Sheets*, 127(C):191–332, 2015.

[138] C. Stanford, S. Westerdale, J. Xu, and F. Calaprice. Surface background suppression in liquid argon dark matter detectors using a newly discovered time component of tetraphenyl-butadiene scintillation. *Physical Review D*, 98:062002, 2018.

[139] G. Bellini, J. Benziger, D. Bick, G. Bonfini, D. Bravo, M. B. Avanzin, B. Caccianiga, L. Cadonati, et al. Cosmogenic Backgrounds in Borexino at 3800 m water-equivalent depth. *Journal of Cosmology and Astroparticle Physics*, 2013(08):049, 2013.

[140] G. Koh. A dark matter search with DarkSide-50. PhD thesis, Princeton University, 2018.

[141] L. Pagani. Direct dark matter detection with DarkSide-50 experiment. PhD thesis, University of Genoa, 2017.

[142] A. J. Peurrung, T. W. Bowyer, R. A. Craig, and P. L. Reeder. Expected atmospheric concentration of ^{42}Ar. *Nuclear Instruments and Methods in Physics Research Section A: Accelerators, Spectrometers, Detectors and Associated Equipment*, 396(3):425–426, 1997.

[143] A. S. Barabash, V. N. Kornoukhov, and V. E. Jants. Estimate of the 42Ar content in the Earth's atmosphere. *Nuclear Instruments and Methods in Physics Research Section A: Accelerators Spectrometers, Detectors and Associated Equipment*, 385(3):530–534, 1997.

[144] I. Kaplan. *Nuclear Physics*. Addison-Wesley, 1963.

[145] X. Mougeot. Reliability of usual assumptions in the calculation of β and ν spectra. *Physical Review C*, 91(5):055504, 2015.

[146] P. Venkataramaiah, K. Gopala, A. Basavaraju, S. S. Suryanarayana, and H. Sanjeeviah. A simple relation for the Fermi function. *Journal of Physics G, Nuclear Physics*, 11(3):359–364, 1985.

[147] A. Lubashevskiy, M. Agostini, D. Budjáš, A. Gangapshev, K. Gusev, M. Heisel, A. Klimenko, A. Lazzaro, et al. Mitigation of $^{42}Ar/^{42}K$ background for the GERDA Phase II experiment. *The European Physical Journal C*, 78(1):1–10, 2018.

[148] V. D. Ashitkov, A. S. Barabash, S. G. Belogurov, G. Carugno, S. I. Konovalov, F. Massera, G. Puglierin, R. R. Saakyan, V. N. Stekhanov, and V. I. Umatov. A liquid-argon ionization detector for the study of double β decay. *Instruments and Experimental Techniques*, 46(2):153–160, 2003.

[149] A. S. Barabash, R. R. Saakyan, and V. I. Umatov. On concentration of 42Ar in liquid argon. *Journal of Physics: Conference Series*, 718(6):062004, 2016.

[150] R. Ajaj, G. R. Araujo, M. Batygov, B. Beltran, C. E. Bina, M. G. Boulay, B. Broerman, J. F. Bueno, et al. Electromagnetic backgrounds and potassium-42 activity in the DEAP-3600 dark matter detector. *Physical Review D*, 100(7):072009, 2019.

[151] M. Agostini, M. Allardt, A. M. Bakalyarov, M. Balata, I. Barabanov, N. Barros, L. Baudis, C. Bauer, et al. Flux modulations seen by the muon veto of the GERDA experiment. *Astroparticle Physics*, 84:29–35, 2016.

[152] B. Macdonald, J. A. Diaz, S. N. Kaplan, and R. V. Pyle. Neutrons from negative-muon capture. *Physical Review*, 139(5B):B1253–B1263, 1965.

[153] M. Danos and E. G. Fuller. Photonuclear reactions. *Annual Review of Nuclear Science*, 15(1):29–66, 1965.

[154] G. Ricco. *Photonuclear reactions I,Lecture Notes in Physics,vol61*. Springer, Berlin, Heidelberg, 1977.

[155] L. B. Bezrukov, V. I. Beresnev, O. G. Ryajskaya, L. N. Stepanets, and G. T. Zatsepin. Investigation of depth-intensity curve of nuclear events induced by muons. *Proceedings of the 13th International Conference on Cosmic Rays*, 3:1947, 1973.

[156] A. Ferrari, P. Sala, A. Fasso, and J. Ranft. FLUKA: a multi-particle transport code. *CERN Yellow report*, 2005-10, 2005.

[157] G. Battistoni, T. Boehlen, F. Cerutti, P. W. Chin, L. S. Esposito, A. Fassò, A. Ferrari, A. Lechner, A. Empl, et al. Overview of the FLUKA code. *Annals of Nuclear Energy*, 82:10–18, 2015.

[158] T. T. Böhlen, F. Cerutti, M. P. W. Chin, A. Fassò, A. Ferrari, P. G. Ortega, A. Mairani, P. R. Sala, G. Smirnov, and V. Vlachoudis. The FLUKA code: developments and challenges for high energy and medical applications. *Nuclear Data Sheets*, 120:211–214, 2014.

[159] V. Vlachoudis. FLAIR: a powerful but user friendly graphical interface for FLUKA. *Proc. Int. Conf. on Mathematics, Computational Methods & Reactor Physics (M&C 2009)*, 1:3, 2009.

[160] C. F. Vigorito and on behalf of the LVD Collaboration. The underground muon flux with 24 years of data of the LVD detector. *Journal of Physics: Conference Series*, 1181(1):012057, 2019.

[161] M. Ambrosio, R. Antolini, A. Baldini, G. C. Barbarino, B. C. Barish, G. Battistoni, Y. Becherini, R. Bellotti, et al. Search for the sidereal and solar diurnal modulations in the total MACRO muon data set. *Physical Review D*, 67(4):042002, 2003.

[162] M. Ambrosio, R. Antolini, A. Baldini, G. C. Barbarino, B. C. Barish, G. Battistoni, Y. Becherini, R. Bellotti, et al. Measurement of the residual energy of muons in the Gran Sasso underground laboratories. *Astroparticle Physics*, 19(3):313–328, 2003.

[163] M. Ambrosio, R. Antolini, G. Auriemma, R. Baker, A. Baldini, G. C. Barbarino, B. C. Barish, G. Battistoni, et al. Vertical muon intensity measured with MACRO at the Gran Sasso laboratory. *Physical Review D*, 52(7):3793, 1995.

[164] N. Agafonova, A. Anokhina, S. Aoki, A. Ariga, T. Ariga, D. Autiero, A. Badertscher, A. Bagulya, et al. Measurement of the atmospheric muon charge ratio with the OPERA detector. *The European Physical Journal C*, 67(1-2):25–37, 2010.

[165] Y. F. Wang, V. Balic, G. Gratta, A. Fasso, S. Roesler, and A Ferrari. Predicting neutron production from cosmic-ray muons. *Physical Review D*, 64(1):013012, 2001.

[166] P. Singh. Rare event searches with DarkSide-50 detector. PhD thesis, University of Houston, 2018.

[167] A. Empl and E. V. Hungerford. A FLUKA study of β-delayed neutron emission for the ton-size DarkSide dark matter detector. *arXiv:1407.6628*, 2014.

[168] A. Fasso, A. Ferrari, J. Ranft, and P. R. Sala. FLUKA: a multi-particle transport code. *CERN Yellow report*, 2005-10, 2005.